



HAL
open science

Variations atmosphériques du CO₂ à l'échelle millénaire durant le stade isotopique MIS 6

Jinhwa Shin

► **To cite this version:**

Jinhwa Shin. Variations atmosphériques du CO₂ à l'échelle millénaire durant le stade isotopique MIS 6. Sciences de la Terre. Université Grenoble Alpes, 2019. Français. NNT : 2019GREAU006 . tel-02171720

HAL Id: tel-02171720

<https://theses.hal.science/tel-02171720>

Submitted on 3 Jul 2019

HAL is a multi-disciplinary open access archive for the deposit and dissemination of scientific research documents, whether they are published or not. The documents may come from teaching and research institutions in France or abroad, or from public or private research centers.

L'archive ouverte pluridisciplinaire **HAL**, est destinée au dépôt et à la diffusion de documents scientifiques de niveau recherche, publiés ou non, émanant des établissements d'enseignement et de recherche français ou étrangers, des laboratoires publics ou privés.

THÈSE

Pour obtenir le grade de

DOCTEUR DE LA COMMUNAUTE UNIVERSITE GRENOBLE ALPES

Spécialité : **Sciences de la Terre, de l'Univers et de
l'environnement**

Arrêté ministériel : 25 mai 2016

Présentée par

Jinhwa SHIN

Thèse dirigée par **Jérôme CHAPPELLAZ**
codirigée par **Roberto GRILLI** et **Frédéric PARRENIN**

préparée au sein du **L'Institut des Géosciences de
l'Environnement** dans **l'École Doctorale Terre Univers
Environnement**

Millennial-scale atmospheric CO₂ variations during the Marine Isotope Stage 6

Thèse soutenue publiquement le **18 mars 2019**,
devant le jury composé de :

M. Didier SWINGEDOUW

Charge de Recherches, CNRS, EPOC (Rapporteur)

M. Eric WOLFF

Professor, University of Cambridge (Rapporteur)

Mme. Pascale BRACONNOT

Directeur de Recherche, CNRS, LSCE (Examineur)

M. Fabien ARNAUD

Directeur de recherche, CNRS, EDYTEM (Président du jury)

M. Frédéric PARRENIN

Directeur de recherche, CNRS, IGE (co-Directeur de thèse)

M. Roberto GRILLI

Charge de Recherches, CNRS, IGE (co-Directeur de thèse)

M. Jérôme CHAPPELLAZ

Directeur de recherche, CNRS, IGE (Directeur de thèse)



Résumé

Le dioxyde de carbone est le second gaz à effet de serre le plus abondant dans l'atmosphère après la vapeur d'eau. A cause de l'augmentation continue des concentrations de dioxyde de carbone atmosphérique due aux activités humaines depuis la révolution industrielle, prédire les changements futurs du climat et des écosystèmes est de première importance. Cependant, les prédictions exactes du climat futur sont limitées du fait des incertitudes dans les estimations d'émissions de carbone et du fait d'une connaissance imparfaite des rétroactions climat / cycle du carbone (Friedlingstein et al., 2006). En général, le CO₂ atmosphérique est contrôlé par les échanges gazeux avec les réservoirs océaniques et les stocks de carbone terrestre (Ahn and Brook, 2014; Bereiter, 2012; Landais et al., 2013). Cependant, du fait de caractéristiques différentes des réservoirs, les échelles de temps des échanges gazeux entre l'atmosphère et les stocks océaniques et terrestres sont différentes. Notre compréhension des mécanismes exacts du cycle du carbone est encore limitée, spécialement sur les échelles de temps longues.

L'objectif principal de cette thèse était de comprendre la variabilité millénaire du CO₂ atmosphérique durant le stade isotopique marin 6 (Marine Isotope Stage 6, MIS 6), l'avant dernière période glaciaire (185-135 ka BP). Durant la première partie de la période MIS 6 (185-160 ka BP), 6 oscillations climatiques millénaires peuvent être observées dans des indicateurs de la température antarctique, du phénomène de bascule bipolaire dans la région Atlantique Nord et de l'intensité des moussons des basses latitudes. Un cycle hydrologique intensifié et des vêlages d'iceberg dans l'Atlantique Nord pourraient avoir impacté la circulation atlantique méridionale de retournement (Atlantic Meridional Overturning Circulation, AMOC) durant MIS 6 (Margari et al., 2010). La reconstruction de CO₂ atmosphérique à partir des carottes antarctiques peut fournir des informations clés sur le lien entre CO₂ atmosphérique et variabilité climatique millénaire. Cependant, les enregistrements existants du CO₂ à partir de la carotte de glace de Vostok ne montrent pas de variabilité millénaire du fait de trop mauvaises résolution et précision.

Pour comprendre la variabilité du CO₂ atmosphérique pendant MIS 6, une précision meilleure que 2 ppm est nécessaire, parce qu'il y a la possibilité d'observer des variations de CO₂ de moins de 5 ppm pendant les plus petits événements isotopiques maximums en Antarctique (Antarctic Isotope Maxima, AIM) comme observés durant la dernière période glaciaire (Ahn and Brook, 2014; Bereiter et al., 2012). Pendant la première année de cette thèse, nous avons amélioré la précision de la méthode d'extraction existante, menant à une reproductibilité des mesures d'environ 1 ppm (1 σ) lorsqu'elle est couplée avec l'analyse chromatographique des gaz (gas chromatography, GC). Cependant, en utilisant le broyeur à billes, quelques morceaux de glace relativement gros (visibles à l'oeil nu) subsistent, ce qui montre que l'efficacité de l'extraction n'est pas optimale. C'est pourquoi nous avons développé un

nouvel instrument appelé « système de broyage par anneaux » pour améliorer l'efficacité de l'extraction de l'air en utilisant des anneaux métalliques. Cependant, la précision du système de broyage par anneaux est 2 ppm, ce qui est moins bon que le système de broyage par billes. Nous avons donc choisi le système de broyage par billes pour reconstruire les données de CO₂ atmosphérique.

Pour examiner comment le CO₂ atmosphérique est lié avec le changement climatique sur les échelles de temps millénaires pendant le MIS 6, nous avons analysé 150 échantillons de CO₂ atmosphérique obtenus à partir de la carotte EPICA Dome C (EDC) sur la période 189.4-135.4 ka BP. Une oscillation mineure et 5 oscillations majeures du CO₂ atmosphérique pendant la première partie de la période du MIS 6 (189-160 ka BP) ont été découvertes. Cette variabilité est très liée avec la température antarctique. Pendant les périodes stadiales courtes dans l'Atlantique Nord, les variations de CO₂ atmosphérique sont négligeables et découplées avec la variabilité de la température antarctique. Durant ces périodes, la force de l'upwelling dans l'océan austral pourrait ne pas être suffisante pour impacter le CO₂ atmosphérique. De plus, 2 modes de variations du CO₂ sont présentes pendant la période du MIS 6. Le maximum de dioxyde de carbone 6 (carbon dioxide maxima 6, CDM 6) suit le réchauffement rapide de l'hémisphère Nord de seulement 100 ± 360 ans, alors que les retards pour les CDM 3 et 4 sont bien plus longs, 100 ± 280 ans en moyenne. Ces deux modes de variation du CO₂ pourraient être liés à un changement de mode de l'AMOC de la première partie du MIS 6 au MIS 6e. Ces deux phénomènes sont aussi observés pendant la dernière période glaciaire. Cependant, les données disponibles permettent seulement une discussion exploratoire des mécanismes responsables de la variabilité du CO₂ pendant MIS 6. Comme les conditions aux limites de la dernière période glaciaire ne peuvent pas être appliquées au MIS 6, des données supplémentaires et des études par modélisation du MIS 6 sont nécessaires.

Abstract

Carbon dioxide is the second most abundant greenhouse gas in the atmosphere after water vapour. Due to the continual increase of atmospheric carbon dioxide concentration caused by human activities since the industrial revolution, predicting future climate and ecosystem changes is of increasing importance. However, exact predictions for future climate are limited because of uncertainties in estimated carbon emissions and poor knowledge about climate-carbon cycle feedbacks (Friedlingstein et al., 2006). In general, atmospheric CO₂ is controlled by gas exchanges with oceanic reservoirs and terrestrial carbon stocks (Ahn and Brook, 2014; Bereiter, 2012; Landais et al., 2013). However, due to the different characteristics of the reservoirs, the time scales of gas exchanges are different. Our understanding of the exact mechanisms of the carbon cycle is still limited, especially on longer time scales.

The main objective of this thesis is to understand the millennial variability of atmospheric CO₂ during the Marine Isotope Stage 6 (MIS 6), the penultimate glacial, period (185–135 kyr BP). During the early MIS 6 period (185-160 kyr BP), 6 millennial-scale climate oscillations can be observed in proxy records of Antarctic temperature, the bipolar see-saw phenomenon in the North Atlantic region, and Monsoon intensity in low latitudes. An intensified hydrological cycle and iceberg calving in the North Atlantic may have impacted on the Atlantic Meridional Overturning Circulation during MIS 6 (Margari et al., 2010). Atmospheric CO₂ reconstructions from Antarctic ice cores can provide key information on how atmospheric CO₂ concentrations are linked to millennial-scale climate changes. However, existing CO₂ records from the Vostok ice core do not show the millennial variability due to the lack of suitable temporal resolution and precision. To understand atmospheric CO₂ variability during MIS 6, a precision of less than 2 ppm is mandatory, because there is a possibility that we could observe small CO₂ variability of less than 5 ppm during the smaller Antarctic isotope maxima events as observed during the last glacial period (Ahn and Brook, 2014; Bereiter et al., 2012).

During the first year of this PhD, we improved the precision of the existing extraction method showing a measurement reproducibility of about 1 ppm (1 σ) when coupled with the GC analysis. However, using the ball mill, a few large pieces of ice (visible by eye) were still left after crushing, which shows that the air extraction efficiency was still low. Thus, we developed a new instrument called the ring mill system to improve the extraction efficiency, using metallic rings. The precision of the ring mill system, however, is ~2 ppm, which is not better than the ball mill system. Therefore, we chose the ball mill system to reconstruct atmospheric CO₂ data.

To investigate how atmospheric CO₂ is related with climate change on millennial time scales during MIS 6, we reconstructed 150 samples of atmospheric CO₂ data from the EPICA Dome C (EDC) ice core during the MIS 6 period (189.4–135.4 kyr BP). One minor and five major variabilities of

atmospheric CO₂ during the early MIS 6 period (189–160 kyr BP) were found. These variabilities are highly matched with Antarctic temperature. During the short stadials in the North Atlantic, atmospheric CO₂ variations are negligible and decoupled with temperature variations in Dome C. During this period, the strength of upwelling in the southern ocean might not be sufficient to impact on atmospheric CO₂. In addition, 2 modes of CO₂ variations are present in the MIS 6 period. One, corresponding to the earliest part of MIS 6 at around 181.5±0.2 kyr BP, where carbon dioxide maxima (CDM) 6 lags abrupt warming in the Northern Hemisphere by only 100±360 yrs, and the other one, for CDM 3 (169.7±0.2 kyr BP) and CDM 4 (174.5±0.2 kyr BP) where the lag is much longer, 1,100±280 yrs on average. These 2 modes of CO₂ variations might be related with a mode change of AMOC from the earliest MIS 6 to MIS 6e. These two phenomena also are observed during the last glacial period. However, the limited available proxy data permit only an exploratory discussion of the mechanisms responsible for CO₂ variability during MIS 6. Because the boundary conditions of the last glacial period cannot be applied to MIS 6, additional proxy data and multiple modelling studies conducted during MIS 6 period are needed.

List of Abbreviations

AABW	Antarctic Bottom Water
AIM	Antarctic Isotope Maxima
AMOC	Atlantic Meridional Overturning Circulation
BCTZ	Bubble-Clathrate Transformation Zone
BIC	Byrd ice core
CDM	Carbon dioxide maxima
CIM	Centrifugal Ice Microtome
COD	Close-off Depth
DIC	Dissolved Inorganic Carbon
EDC	EPICA Dome C
EDML	EPICA Dronning Maud Land
EV	Electronic Valve
FID	Flame Ionization Detector
GC	Gas chromatography
LID	Lock-In Depth
MIS	Marine Isotope Stage
NADW	North Atlantic Deep Water
NH	Northern Hemisphere
NIPR	Japanese National Institute of Polar Research
NOAA	National Oceanic and Atmospheric Administration
NPDW	North Pacific Deep Water
OSU	Oregon State University
P	pressure gauges
SH	Southern Hemisphere

SNU	Seoul National University
SWW	Southern Westerly Winds
TCD	Thermal Conductivity Detector
THC	Thermohaline circulation
UBern	University of Bern
V	manual Valve

Table of Contents

Résumé	I
Abstract	III
List of Abbreviations	V
Chapter 1. Introduction	1
1.1. Climate and carbon cycle.....	2
1.2. Major Carbon reservoirs	3
1.2.1. Atmosphere.....	4
1.2.2. Terrestrial Biosphere.....	4
1.2.3. Oceans.....	5
1.2.3.1. Physical-chemical processes.....	5
1.2.3.2. The marine carbon pumps.....	6
1.2.3.3. Thermohaline circulation and CO ₂ cycle	7
1.3. Atmospheric CO ₂ from the ice core in the past.....	8
1.4. Carbon cycle mechanisms in the past on millennial time scales.....	10
1.5. Thesis overview	11
Chapter 2. The ice core archive	14
2.1. Sample selection for this study	15
2.2. Gas trapping in the ice	16
2.3. Physical and chemical processes affecting atmospheric CO ₂ signal.....	18
2.3.1. Physical processes in the firn column affecting CO ₂ value	18
2.3.1.1. Gravitational fractionation effect.....	18
2.3.1.2. Signal attenuation effect	19
2.3.1.3. Thermal diffusion effect	20
2.3.1.4. Heterogeneous gas trapping.....	21

2.3.2. Chemical processes affecting gas composition in ice	21
2.3.2.1. Oxidation of organic molecules	21
2.3.2.2. The reaction of carbonate dust with acid in the ice.....	22
2.3.2.3. The snow melting-refreezing process	22
2.3.2.4. Antarctic ice cores for CO ₂ studies	22
2.4. Gas age calculation challenge	23
Chapter 3. Introduction to gas extraction methods	24
3.1. Wet extraction	24
3.2. Sublimation system	26
3.3. Dry extraction	27
3.3.1. Ball mill	27
3.3.2. Needle cracker	28
3.3.3. Centrifugal Ice Microtome (CIM)	29
3.3.4. Drawbacks of dry gas extraction	30
3.4. Application of extraction methods on different ice types	30
Chapter 4. Improvement in the precision of the existing extraction method: the ball mill system	34
4.1. Ball mill system and Gas chromatography analysis	34
4.1.1. The dry extraction	36
4.1.2. The analytical line system	36
4.2. Experimental procedure	40
4.2.1. Cell Preparation	40
4.2.2. Sample preparation	41
4.2.3. Gas extraction	42
4.2.4. Blank tests	43
4.2.5. Analysis of atmospheric CO ₂ concentration	44

4.2.5.1. Calibration	44
4.2.5.2. CO ₂ calculation	45
4.2.5.3. Water vapour percentage calculation	45
4.2.5.4. Data correction	46
4.3. Improvements with respect to the existing setup	47
4.3.1. Reduction of water vapour inputs	48
4.3.2. Improvement of sample throughput	50
4.4. Conclusion	50
Chapter 5. A new high efficiency dry extraction technique for the measurement of atmospheric CO₂ in Antarctic ice cores	51
5.1. The Ring mill system	52
5.2. Distribution of grain size of the ice powder.....	53
5.3. Results and discussion	56
5.3.1. Results from blank tests	56
5.3.2. Results from Antarctic ice cores	59
5.4. Conclusion	60
Chapter 6. Millennial-scale atmospheric CO₂ variations during MIS 6 period.....	62
Abstract.....	63
6.1. Introduction.....	64
6.2. Methods.....	67
6.2.1. CO ₂ measurements	67
6.2.2. CH ₄ measurements.....	67
6.2.3. Nitrogen isotopes	68
6.2.4. The gravitational correction	68

6.2.5. Ice age revision by estimating Δ depth from $\delta^{15}\text{N}$ in air of ice.....	69
6.2.6. Age scale revision of MD01–2444 marine sediment record.....	71
6.3. Results.....	72
6.3.1. The new high-resolution and high precision CO_2 record during MIS6	72
6.3.2. Relationship between temperature in Dome C and atmospheric CO_2	73
6.3.3. Millennial variabilities during early MIS 6 period	73
6.3.4. Leads and lags between CO_2 and the abrupt warming in Northern Hemisphere	75
6.4. Discussion.....	77
6.4.1. Atmospheric CO_2 on millennial time scale	77
6.4.2. Why did CO_2 lag the abrupt warming in NH during MIS 6e?.....	80
6.5. Conclusion	82
Annex I	84
Annex II	85
Annex III.....	87
Annex IV	90
Annex V.....	93
References.....	94
Chapter 7. Conclusions and future plans.....	98
References.....	100
Acknowledgements	109

Chapter 1

Introduction

Future climate and ecosystem changes due to the continual increase of atmospheric carbon dioxide concentration caused by human activities since the industrial revolution are inevitable but could be reduced through emission control. Projections for future climate are limited because of uncertainty with respect to estimated carbon emissions and a lack of exact knowledge about climate-carbon cycle feedbacks (Friedlingstein et al., 2006). Aside from anthropogenic emissions, atmospheric CO₂ is mainly controlled by gas exchange with oceanic reservoirs and terrestrial carbon stocks (Ahn and Brook, 2014; Bereiter et al., 2012; Landais et al., 2013). Due to the different characteristics of the reservoirs, the time scales of gas exchange between the atmosphere and the oceanic and terrestrial carbon stocks are different. Due to the limited duration of direct measurements of atmospheric CO₂ which only started in 1957 (Keeling, 1960), our understanding of the carbon cycle dynamics is limited on longer time scales.

Ice core studies allows to considerably extend the historical perspective by reconstructing atmospheric CO₂ directly from gas preserved in polar ice sheets. This led so far to a record spanning over 800,000 yrs (Lüthi et al., 2008; Petit et al., 1999). This record is essential to understand carbon cycle mechanisms on longer time scales. It notably shows that atmospheric CO₂ closely parallels variabilities in the ice core isotopic temperature record during the last 800,000 yrs (Fischer et al., 2010; Lorius et al., 1990; Petit et al., 1999). In this thesis, I reconstructed atmospheric CO₂ concentrations from the European Project for Ice Coring in Antarctica (EPICA) Dome C during the Marine Isotope Stage (MIS) 6 period (185 kyr BP–135 kyr BP), the penultimate glacial period, to understand the atmospheric CO₂ variability on millennial time scales and to compare it with other records.

The general context about atmospheric CO₂ is introduced in Chapter 1.1; the characteristics of the three main carbon reservoirs involved on Quaternary time scales: atmosphere, ocean and terrestrial biosphere, are discussed in Chapter 1.2. Previous ice core studies about atmospheric CO₂ over the last 800,000 yrs are introduced in Chapter 1.3. Carbon cycle mechanisms on millennial time scales are reviewed in Chapter 1.4, followed by the outline of this thesis.

1.1. Climate and carbon cycle

Carbon dioxide is the second most abundant greenhouse gas in the atmosphere after water vapour. The atmosphere receives short-wave energy from the sun, and this energy is partially absorbed by the surface of the Earth and re-emitted to the atmosphere as long-wave energy. This long-wave energy is partially absorbed and re-emitted by greenhouse gases in the atmosphere. This phenomenon is called the greenhouse effect. CO₂ does not condense or precipitate in the atmosphere, and considerably affects the radiative forcing of greenhouse gases by feedback mechanisms (Lacis et al., 2010).

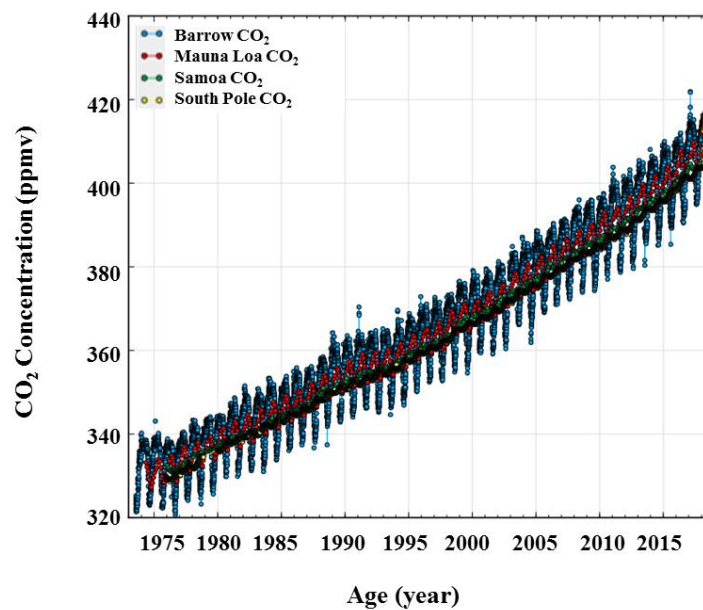


Figure 1.1. Atmospheric CO₂ concentrations observed directly at the Barrow, Mauna Loa and American Samoa and South Pole Observatory. Data were obtained from Tans and Keeling. (2017) and NOAA website.

Charles David Keeling began to measure atmospheric CO₂ in Hawaii at the Mauna Loa Observatory in 1958. The instrumental record of atmospheric CO₂, measured continuously since Keeling's first measurements, is called the 'Keeling curve'. Mean annual atmospheric CO₂ concentrations measured at Mauna Loa Observatory have increased continuously from about 315 ppmv in 1958 to 406.99 ppmv when this chapter was written, as of August 2018. Atmospheric CO₂ concentrations reached the 400 ppmv threshold on May 9, 2013, which was recorded at Mauna Loa Observatory (Tans and Keeling, 2017). This concentration is about 40 % higher than the preindustrial level, approximately 280 ppmv (Etheridge et al., 1996) and is unusually high, at least during the last 800 kyr (Lüthi et al., 2008). Atmospheric CO₂ increases by ~1.5 ppmv on average every year. This unprecedented increase of atmospheric CO₂ is directly caused by human activities such as fossil fuel

burning, cement production, reduced soil carbon stock by land use change, the increase of agricultural production.

Nowadays, atmospheric CO₂ is measured by various observatories that form a global network, allowing to depict regional differences and to better constrain the sources and sinks. These observatories include the well-known United States National Oceanic and Atmospheric Administration (NOAA) stations at Barrow and Mauna Loa in Northern Hemisphere (NH), and American Samoa and South Pole in Southern Hemisphere (SH) (Figure 1.1). With these data sets, we are able to observe atmospheric CO₂ variations globally on various time scales from hourly to multi decadal scales over a period of 60 years. Global observations show a distinct seasonal periodicity of CO₂, which is related with photosynthesis of vegetation on land and soil respiration, themselves impacted by temperature and humidity on inter-annual time scales. The seasonal cycle of atmospheric CO₂ is dominated by the northern Hemisphere: due to higher global photosynthesis during the summer in the NH, atmospheric CO₂ concentrations reach their annual minimum in November, and due to low photosynthesis in NH winter, the concentration of atmospheric CO₂ is highest in May. In addition, these observations show that atmospheric CO₂ emissions by fossil fuel occur mostly in the NH. The amplitude of the seasonal change in the NH has been increasing for 40 years. On the other hand, the variation of the seasonal cycle in the SH is relatively smaller, because of a smaller land mass and less agriculture in SH.

1.2. Major Carbon reservoirs

Carbon can be stored in the atmosphere, the ocean, the terrestrial biosphere and in lithospheric sediments, the four main carbon reservoirs (Figure 1.2). The size of the carbon stock of each reservoir is different, varying from 600 Gt in the atmosphere to 63,000,000 Gt in the lithosphere (Holmen, 1992). On geological time scales, atmospheric CO₂ is mainly controlled by the balance between volcanic outgassing and carbon sequestration through continental weathering related with plate tectonics. On shorter time scales such as along the Quaternary era, the concentration of CO₂ in the atmosphere is controlled by gas exchange with the ocean and terrestrial carbon reservoirs, which is called the biogeochemical carbon cycle (Hain et al., 2014; Holmen, 1992; Sigman and Boyle, 2000). Atmospheric CO₂ can be captured from the atmosphere via biological fixation in the land and oceans via photosynthesis. On the other hand, on land, due to soil respiration, carbon can be released from the land into the atmosphere (Davidson et al., 2000; Mielenick and Dugas, 2000). Understanding possible evolution of gas exchange between the ocean and atmosphere, as well as changes of terrestrial carbon stocks become an important issue for understanding the future behaviour and role of atmospheric CO₂.

In this section, only three reservoirs--ocean, atmosphere and terrestrial biosphere--are discussed. The time scale of carbon exchanges between lithospheric sediments and the atmosphere is over 200 Myr (Figure 1.2), making them negligible on millennial timescales.

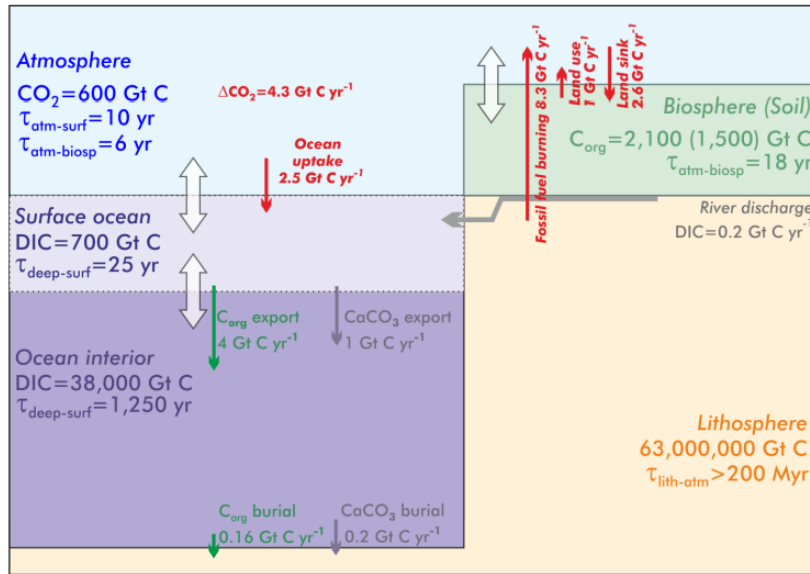


Figure 1.2. Global carbon cycle during the pre-industrial global carbon cycle (Holmen, 1992). Arrows indicates the direction of flux while numbers and arrows in red correspond to anthropogenic perturbations of the carbon cycle during 2002-2011 (Le Quéré et al., 2012; Sigman and Boyle, 2000).

1.2.1. Atmosphere

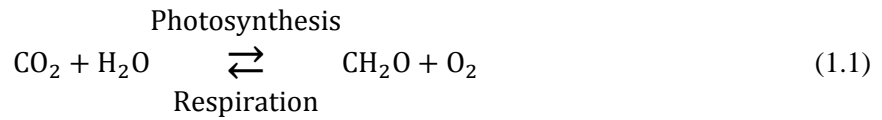
Among the three Earth surface reservoirs, atmosphere, land and ocean, the amount of CO_2 is smallest in the atmosphere, and the majority of carbon in the atmosphere exists as carbon dioxide. Thus, atmospheric CO_2 responds sensitively to the variations of the global carbon cycle. About 380 – 600 PgC is stored in the atmospheric reservoir during glacial and interglacial periods, respectively, corresponding to concentrations of atmospheric CO_2 during glacial and interglacial periods which varied between 180 and 280 ppmv as measured in the ice core record (Lüthi et al., 2010). To understand how atmospheric CO_2 is related with climate change, we should understand the timescales of carbon exchange between atmospheric CO_2 and the terrestrial, oceanic, and sedimentary reservoirs. The residence time of a given species (i.e. CO_2) in a reservoir (i.e. the atmosphere) is referred to as its lifetime. The lifetimes of CO_2 differ depending on the type of reservoirs from days to multi-millennia and longer (Figure 1.2).

1.2.2. Terrestrial Biosphere

The terrestrial biosphere is divided into carbon in living vegetation, unfrozen soils, permafrost and peatlands. About 2,100 PgC is stored in the terrestrial biosphere.

Terrestrial carbon is involved with photosynthesis and respiration in plants, and with soil respiration (microbial and root respiration). Photosynthesis is affected by light and specific enzymes. Soil respiration is also called biodegradation, and atmospheric CO_2 is produced by decomposition of organic matter. These are mostly controlled by temperature and precipitation (Chae, 2011; Davidson et

al., 2000; Kim et al., 2010; Mielnick and Dugas, 2000). These processes are the biochemical photosynthesis-respiration reaction, which can be explained by a simple equation:



The photosynthesis-respiration equation above shows that atmospheric CO₂ is reduced by photosynthesis, and via respiration, atmospheric CO₂ is produced. The time scale of the carbon exchange between vegetation and soils and atmosphere varies from years to decades (Holmen, 1992).

1.2.3. Oceans

3/4 of the Earth surface is occupied by oceans. Around 38,000Gt of carbon is stored in the world's oceans, the surface ocean reservoir consists of about 700 – 900 PgC, and about 37,000 PgC is located in the deep ocean (IPCC, 2007). Carbon is exchanged between the atmosphere and the surface ocean on timescales of years to decades. Atmospheric CO₂ is exchanged with carbon in the deep ocean on millennial time scales (about 1,250 years) because carbon exchange with the deep ocean is governed by ocean circulation. Carbon is also exchanged between the surface ocean and deep ocean reservoirs, and the time scale for this exchange is about 25 years (Sigman and Boyle, 2000). Carbon is exchanged between atmosphere and ocean via physical-chemical, dynamical or biological processes. These three processes are discussed here.

1.2.3.1. Physical-chemical processes

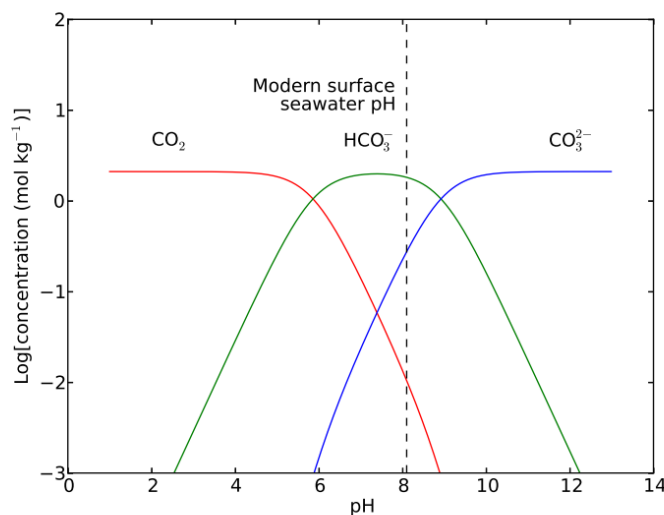
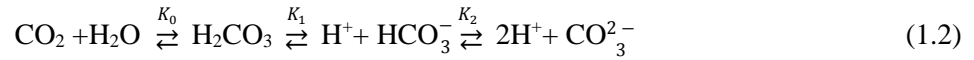


Figure 1.3. CO₂, HCO₃⁻ and CO₃²⁻ in the surface ocean when temperature is 25°C, salinity is 35 ‰ and [DIC] is 2.1 mmol kg⁻¹. Dotted line indicates pH of Modern surface seawater. This graph is from (Eggleston, 2015).

Atmospheric CO₂ is soluble, thus atmospheric CO₂ reacts with water to form dissolved CO₂ and dissociate into three different inorganic forms: carbonic acid ion (H₂CO₃), bicarbonate ion (HCO₃⁻), and carbonate ion (CO₃²⁻). These three inorganic forms make together the so-called Dissolved Inorganic Carbon (DIC).



K₀, K₁ and K₂ are the dissociation constants, which depend on sea water temperature, sea water salinity and pressure. The concentration of dissolved inorganic carbon (DIC) in the ocean is the total of the concentrations of carbonic acid, bicarbonate and carbonate (eq. 1.3, eq. 1.4). Dissolved CO₂ is also present in the oceans, negligible compared to DIC. Thus, the total DIC concentration of sea water can be simplified to eq.1.5:

$$\text{DIC} = [\text{CO}_2] + [\text{HCO}_3^-] + [\text{CO}_3^{2-}] \quad (1.3)$$

$$[\text{CO}_2] = [\text{CO}_{2(\text{aq})}] + [\text{H}_2\text{CO}_3] \quad (1.4)$$

$$\text{DIC} \approx [\text{HCO}_3^-] + [\text{CO}_3^{2-}] \quad (1.5)$$

Thus, the three DIC components are splitted depending on the pH or the alkalinity of water as seen in figure 1.3. Figure 1.3 shows speciation of DIC in the surface ocean when sea temperature in the ocean is 25°C, salinity is 35‰ and the amount of DIC is 2.1 mmol/kg. The majority of DIC is bicarbonate, which makes up ~ 90%, and the second is carbonate (around 10%). Dissolved CO₂ constitutes less than 1%. Via this reaction, on short timescales, atmospheric CO₂ is taken up by the ocean to form DIC. The alkalinity in the deep ocean is affected on long timescales by this reaction, which changes the depth of the lysocline and impacts on the dissolution of calcium carbonate.

1.2.3.2. The marine carbon pumps

CO₂ exchange between the atmosphere, the surface ocean and the deep ocean is described by two major “pumping” mechanisms: the solubility pump and the biological pump (also referred to as the carbonate pump and the organic carbon pump, respectively) (Toggweiler et al., 2003a; Toggweiler et al., 2003b; Volk and Hoffert, 1985) (Figure 1.4)

The solubility pump is related with temperature and salinity due to the dissociation constants of the DIC. Solubility of CO₂ is greater in cooler and fresh surface waters. Thus, the oceanic uptake of atmospheric CO₂ through this pumping mechanism is stronger in Polar Regions. The formation deep water occurs in regions with high water density, precisely where surface waters are cold, thus these regions are synonymous with areas of high CO₂ solubility.

The biological pump consists of the soft-tissue pump and the carbonate pump. The soft-tissue pump (or organic pump) is the cycling of carbon fixation by phytoplankton in the euphotic (sunlight) region during photosynthesis. The carbonate pump is the cycling of calcium carbonate (CaCO_3) produced by certain organisms as shells made of carbonate (CaCO_3). Thus, for the biological pump, light, CO_2 , nutrients (such as, nitrogen and phosphorous) and oligo-elements (Fe) are required. Nutrients are a limiting factor in most oceanic regions. For example, in the Southern Ocean, biological productivity is limited due to a relatively low nutrient content, notably of iron (Marinov et al., 2008).

Regarding the organic carbon pump, phytoplankton is consumed by zooplankton (planktonic animals). The photosynthesized carbon is transformed in short-living particulates, such as skeletons or faecal particles. This organic carbon then sinks into the ocean interior if it is not demineralised by respiration. If organic carbon is demineralized, at the surface, the resulting CO_2 is exchanged with the atmosphere directly. Thus, DIC in the surface ocean is reduced by biological carbon fixation and the export of organic carbon into the deep ocean. These two mechanisms result in a decrease of pCO_2 in the surface ocean.

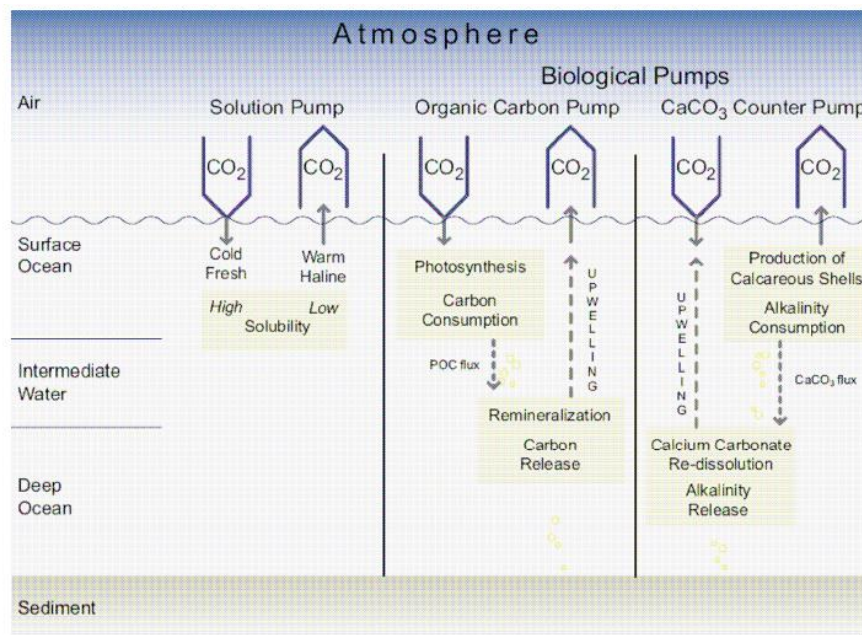


Figure 1.4. Two major pumping mechanisms of CO_2 from the atmosphere into the ocean (IPCC, 2007).

1.2.3.3. Thermohaline circulation and CO_2 cycle

Ocean circulation is driven by density gradients, which are affected by temperature and salinity. It is referred to as thermohaline circulation (THC). Deep cold and salty waters are formed at high latitudes of both hemispheres especially in the North Atlantic region and the Southern Ocean (Figure 1.5). Deep water originating in the North Atlantic region is referred to as North Atlantic Deep Water

(NADW) and the deep water current from the Southern Ocean is referred to as the Antarctic bottom water (AABW). The Atlantic Meridional Overturning Circulation (AMOC) is composed of the Antarctic Bottom Water (AABW), making up the upper overturning cell, and North Atlantic Deep Water (NADW), which forms the lower overturning cell. The strength of AMOC is thought to play a major role in the so-called “bipolar seesaw mechanism” (Broecker, 1998; Stocker and Johnsen, 2003), corresponding to the reverse trends in the temperature records from Greenland and Antarctica during rapid climatic events of past glaciations. When temperature increases in the Northern Hemisphere, it generates ice sheet melting. The resulting meltwater partly runs toward the surface of the North Atlantic Ocean, which salinity is reduced. The density of surface water in the North Atlantic thus decreases, leading to a reduction of NADW intensity. This leads to subsequent cooling of the Northern hemisphere and warming of Antarctica. This change of ocean dynamics can impact on the carbon cycle, through mechanisms which will be discussed in detail in section 1.4.

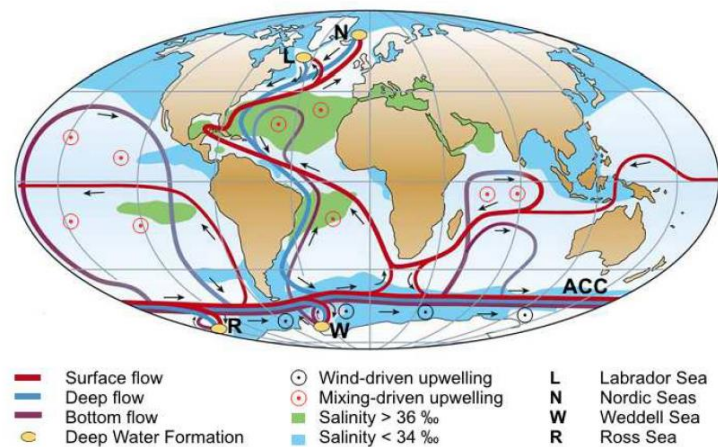


Figure 1.5. Thermohaline circulation (Kuhlbrodt et al., 2007; Rahmstorf, 2002).

1.3. Atmospheric CO₂ from the ice core in the past

Beyond the instrumental record providing direct measurements into the atmosphere, atmospheric CO₂ concentration can be reconstructed in principle via various paleoclimate records: ice cores, the carbon isotopic composition of phytoplankton, boron isotope signatures of foraminifer shells and leaf stomata density patterns (Royer et al., 2001). However, out of these records, only polar ice cores permit us to reconstruct a precise and reliable record of atmospheric CO₂ concentration in the past (Bereiter et al., 2012; Marcott et al., 2014; Petit et al., 1999). The mechanisms leading to the formation of this paleo-record of atmospheric CO₂ will be explained in section Chapter 2. The other CO₂ proxies allow a reconstruction of CO₂ concentrations over much longer geological periods than ice cores, however, the precision of the data is low.

Atmospheric CO₂ variations and temperature derived from δD of water over the last 800,000 years are shown in Figure 1.6 (Jouzel et al., 2007; Lüthi et al., 2010; Petit et al., 1999), covering 8 glacial and interglacial cycles. During the interglacial periods, CO₂ concentration varied between 250–300 ppmv. In addition, Figure 1.6 shows that atmospheric CO₂ closely parallels temperature variability as reconstructed from EDC during that period (Fischer et al., 2010; Lorius et al., 1990; Petit et al., 1999). During glacial periods, CO₂ concentrations decrease slowly to about 180 ppmv. CO₂ concentrations during the minima of glacial periods vary between 170–190 ppmv. During the glacial terminations atmospheric CO₂ increases rapidly from the glacial period level to the interglacial level.

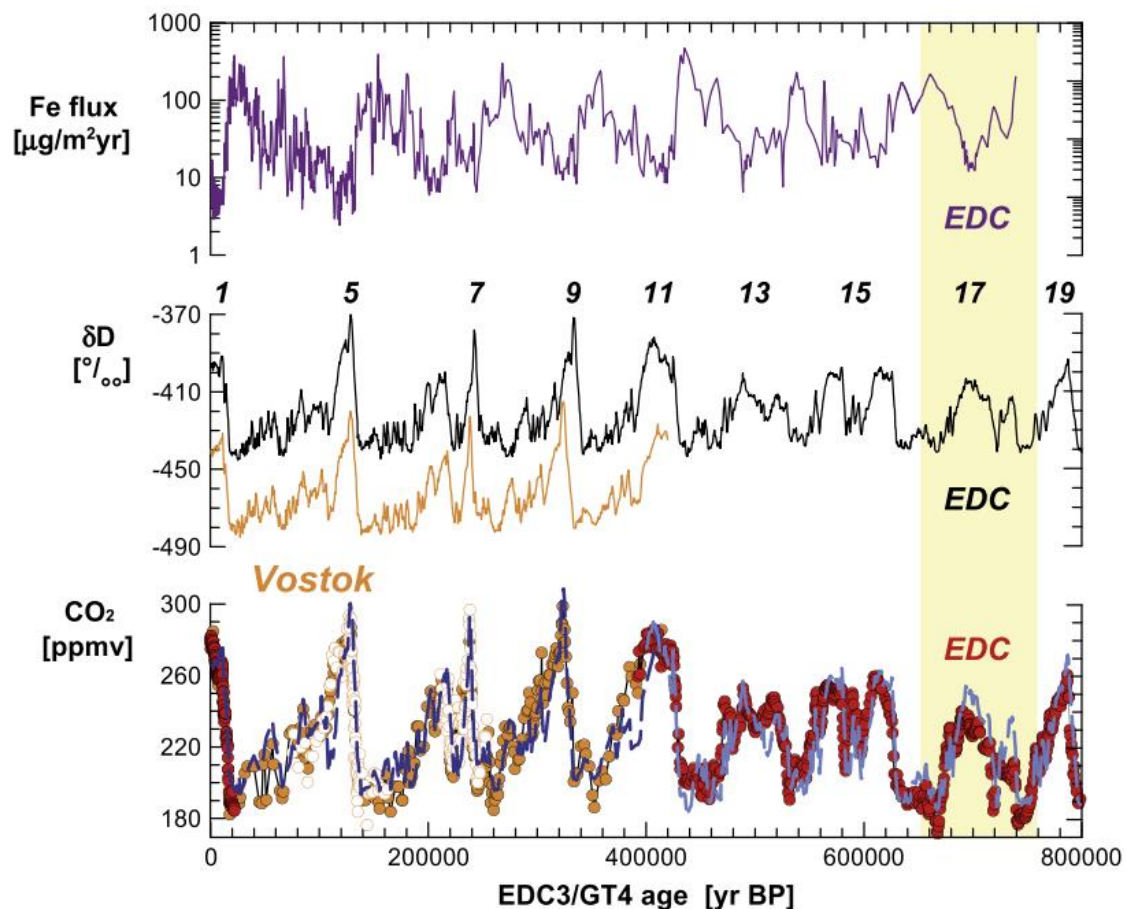


Figure 1.6. Top: Iron fluxes from EDC (Martínez-García et al., 2009). Middle: Temperature proxy data which are derived from continuous stable water isotope records. These two data were obtained from EDC and Vostok ice core (Jouzel et al., 2007; Petit et al., 1999). Bottom: Atmospheric CO₂ concentrations from EDC and Vostok ice cores (Fischer et al., 1999; Lüthi et al., 2010; Monnin et al., 2001; Petit et al., 1999; Siegenthaler et al., 2005). Bold dashed lines in blue indicate a CO₂ estimate derived from the linear interpolation. Age scale of these data for the EDC and the Vostok ice cores set are on the EDC3 and GT4 age scale, respectively.

Millennial-scale variability of atmospheric CO₂ has been carefully investigated over the last glacial period. It appears to be closely linked to major Antarctic Isotope Maxima (AIM) (Ahn and Brook, 2014; Bereiter et al., 2012), varying on the order of 10–20 ppmv during the major AIM events (Bereiter et al., 2012). Atmospheric CO₂ reaches its maximum values with a delay with respect to Antarctic temperature. It then decreases slowly. However, this apparent offset may be related with the difficulty to accurately estimate the age offset between the ice and the trapped gases in the ice (Louergue et al., 2008). During the smallest Antarctic isotope maxima events, smaller CO₂ variabilities are observed of less than 5 ppmv (Ahn and Brook, 2014; Bereiter et al., 2012).

1.4. Carbon cycle mechanisms in the past on millennial time scales

In general, atmospheric CO₂ on millennial-timescale can be controlled by CO₂ exchange between Ocean and Atmosphere, as well as changes of terrestrial carbon stocks. Coupled climate carbon cycle models reported that the variations of atmospheric CO₂ concentration on millennial-timescale are mainly dominated by deep ocean inventory requiring a few millennia to react to climate change (Schmittner and Galbraith, 2008). These variations of CO₂ concentration might be compensated by fast changes in the terrestrial biosphere (Bouttes et al., 2011; Menviel et al., 2014; Schmittner and Galbraith, 2008).

In the deep ocean reservoir, the Southern Ocean is important in regulating global atmospheric CO₂ variations on millennial time scales (Ahn and Brook, 2014; Bereiter et al., 2012). This is identified by a close relationship between atmospheric CO₂ and Antarctic temperature in EDC during the last 800,000 years (Lüthi et al., 2008). Because the Antarctic Circumpolar current in the Southern Ocean is highly enriched in dissolved CO₂, CO₂ can be released from the ocean to the atmosphere via Southern Ocean ventilation, possibly driven by changes in stratification, buoyancy forcing and the strength and position of circumpolar westerly winds (Toggweiler et al., 2006) and the variations of sea ice extent in the Southern Ocean (Stephens and Keeling, 2000). Changes in the AMOC (Schmittner and Galbraith, 2008), are also thought to be important mechanisms of CO₂ release into the atmosphere on millennial time scales.

Exchange between deep and shallow waters in the Southern Ocean is partly conditioned by Southern Westerly Winds (SWW) which is a zonal circulation system located in the mid latitudes of the Southern Hemisphere. SWW moves surface waters northward by Ekman transport in the Southern Ocean. Surface waters are then replaced by the upwelling of deep water, containing high amounts of dissolved CO₂. Upwelling of deep water driven by wind in the Southern Ocean can thus release CO₂ to the atmosphere (Toggweiler et al., 2006). Therefore the SWW position and strength in the Southern Ocean can substantially impact on the upwelling and ventilation of deep water, and is a key factor for modulation of atmospheric CO₂.

In the Southern Ocean, biological productivity is limited, reflected in a relatively low chlorophyll content. This indicates that the phytoplankton in the Southern Ocean have limited access to essential micronutrients such as iron. Aeolian dust input into the Southern Ocean can modulate iron deposition. If the amount of aeolian dust input in the Southern Ocean increases, the productivity of phytoplankton in the Southern Ocean increases and carbon fixation in the Southern Ocean biosphere is thus enhanced. Organic detritus sinks into the deep ocean reservoir (Marinov et al., 2008), and atmospheric CO₂ can thus be drawn down by what is known as the biological carbon pump (Martin, 1990). Atmospheric CO₂ might also be affected by sea ice dynamics, because sea ice may block the carbon exchange between the atmosphere and the Southern Ocean (Stephens and Keeling, 2000). Sea ice can also suppress the extent of surface water where biological fixation occurs actively (Hillenbrand and Cortese, 2006). This may have an impact on the efficiency of deep-ocean internal mixing, and therefore the mean residence time of carbon in the ocean (Ferrari et al., 2014). A reduced biological pump can also increase atmospheric CO₂ when upwelling of deep water with abundant nutrients is reduced (Schmittner, 2005). Thus, the impact of upwelling in the Southern Ocean on atmospheric CO₂ concentrations may have multiple, counteracting components.

The AMOC is able to control atmospheric CO₂ concentrations as well (Bouttes et al., 2011; Menviel et al., 2014; Schmittner and Galbraith, 2008). When large amounts of low-density fresh water are released into the North Atlantic, the AMOC is shut down. Thus, heat piles up in the South, and moisture movement from the Atlantic to the Pacific is reduced. Therefore, sea ice retreats in the Southern Ocean. On the other hand, the North Atlantic is cooled, and the Intertropical Convergence Zone is shifted to the south. Salinity at the surface of the Pacific Ocean is increased. Thus, AABW and North Pacific Deep Water (NPDW) transport are enhanced (Menviel et al., 2014). Enhanced NPDW transport ventilates deep Pacific carbon via the Southern Ocean. Thus, atmospheric CO₂ increases.

Terrestrial carbon is affected by variation of vegetation and soil respiration (microbial and root respiration) in the terrestrial biosphere. Temperature and precipitation are the most important control factors for these two processes (Chae, 2011; Davidson et al., 2000; Kim et al., 2010; Mielnick and Dugas, 2000). Thus, thawing of permafrost (Köhler et al., 2014), biomass decomposition caused by drought which cause decomposition of biomass (Marcott et al., 2014), changes in precipitation connected to shifts of the Intertropical Convergence Zone (mainly in northern Africa and northern South America) may cause variations in terrestrial carbon stocks (Menviel et al., 2008).

1.5. Thesis overview

The main goal of this thesis is to understand atmospheric CO₂ variability on millennial time scales during the penultimate glacial period (approximately 185 to 135 kyr BP) and also to explore similarities/differences in atmospheric CO₂ variations on millennial time scales during the past two

glacial periods. These two glacial periods are also identified by numbered Marine Isotope Stages (MIS). Marine Isotope Stages are numbered stages that were originally designed to designate the major climatic swings. The penultimate glacial corresponds to MIS 6 and the part of the last glacial period investigated in this study corresponds to the MIS 3 period (60–27 kyr BP) (Figure 1.7). To this end, I reconstructed for the first time at high temporal resolution and with a suitable analytical precision atmospheric CO₂ concentrations from the EDC ice core during the MIS 6 period.

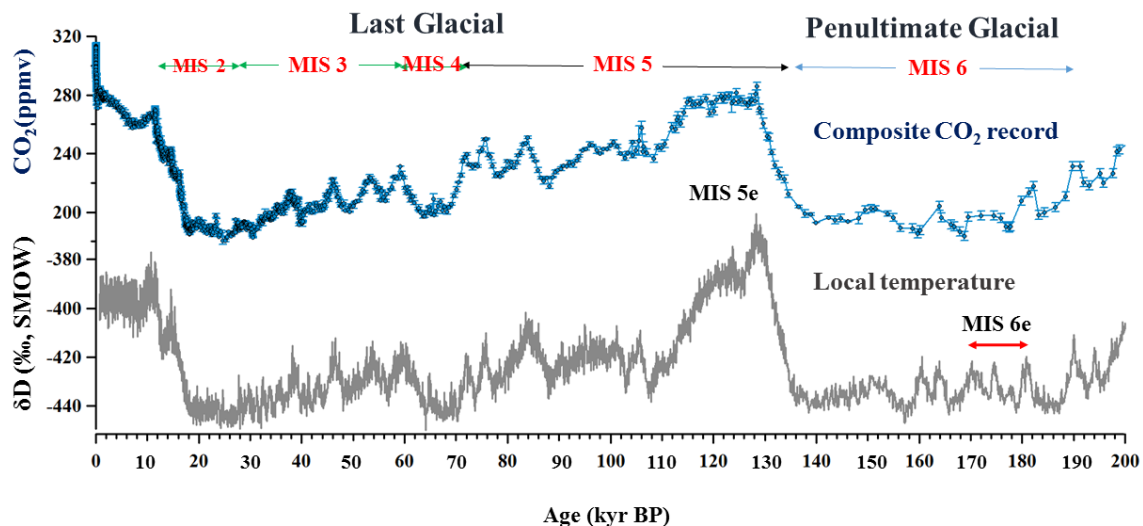


Figure 1.7. Atmospheric CO₂ concentrations from Antarctica (Bereiter et al., 2015) and local temperature from Dome C (Jouzel et al., 2007) during the past two glacial periods.

Polar ice cores permit us to directly reconstruct a record of atmospheric CO₂ concentration in the past (Bereiter et al., 2012; Marcott et al., 2014; Petit et al., 1999). However, this does not mean that all ice cores have equal potential to reconstruct CO₂ concentrations. The potential of CO₂ reconstruction from Greenland and High Mountain ice cores is limited due to contamination. In addition, we cannot reconstruct CO₂ concentrations over the entire 800 kyr period covered by ice cores with a sub-centennial time resolution due to the physical processes of gas trapping in the firn layer of the ice sheet, which smooth atmospheric gas concentrations. These processes are discussed in Chapter 2.

To reconstruct atmospheric CO₂ concentrations from ice cores, wet extraction (Kawamura et al., 2003), crushing extraction (Ahn et al., 2009; Bereiter et al., 2013) or sublimation extraction (Schmitt et al., 2011) are used. In Chapter 3, different extraction techniques are described. High precision measurements are needed to observe small CO₂ variability of less than 5 ppmv during the smallest Antarctic isotope maxima events (Ahn and Brook, 2014; Bereiter et al., 2012). To understand atmospheric CO₂ variability during MIS 6, a precision of less than 2 ppmv is mandatory. We improved the precision of the existing extraction method – based on a ball mill - showing a measurement

reproducibility of about 1 ppmv (1σ) when coupled with the Gas chromatography analysis. The improved procedure and how the measurement are improved are introduced in Chapter 4. However, using the ball mill, a few large pieces of ice (visible by eye) were still left after crushing, which shows that the air extraction efficiency is not optimal. Thus, we tested a new extraction method to improve the extraction efficiency, as described in Chapter 5.

In Chapter 6, new atmospheric CO₂ data on millennial time scales during the penultimate glacial period are presented. Similarities and differences between atmospheric CO₂ during the past two glacial periods are discussed. Some possible mechanisms which may be involved in atmospheric CO₂ variations on millennial time scales are suggested, followed by the main conclusions of this thesis and future plans.

Chapter 2

The ice core archive

Polar ice cores are vertical cores obtained from the Greenland and Antarctic ice sheets, usually drilled at locations where snow accumulates annually and does not melt, in order to obtain continuous records. Deep ice cores are usually drilled at ice domes or ice divides where the ice is stratigraphically well-layered and ice sheet flow is at a minimum. When snow accumulates on a polar ice sheet, the air that circulates via the overlying layers is occluded in the ice layers directly. Thus, air initially in the form of bubbles deeper as clathrates in the ice captures the atmospheric composition when the ice formed. With ice and occluded air from ice cores from Greenland and Antarctica, we can obtain continuous information on the climate of the past that long predates direct instrumental measurement. For example, the isotopic composition (such as $\delta^{18}\text{O}$, δD) of the ice allows us to quantify temperature variations in the past. Tephra produced from volcanic eruptions which occurred close to ice core sites are also deposited in ice cores. In addition, dust and chemical aerosol species (Na^+ , NO_3^- , NH_4^+) are also recorded in the ice, which allow us to understand the changes of atmospheric circulation pattern. From the occluded air in the ice, we can reconstruct the atmospheric composition directly including the trace greenhouse gases CO_2 , CH_4 and N_2O .

The atmospheric CO_2 record in ice cores reflects atmospheric CO_2 in the past, but physical and chemical properties may affect atmospheric CO_2 signals. First, air is moved into the firn via diffusion and air is trapped gradually. Gas moves into the firn column at different rates, and the heavier molecular species are enriched at the bottom of the firn, which can bias measured atmospheric CO_2 concentrations. Second, CO_2 records can be contaminated by the in-situ production of CO_2 caused by carbonate-acid reactions and oxidation of organic molecules. In addition, due to the snow melting-refreezing process, CO_2 data can be scattered due to higher solubility in water compared to other gases (Neftel et al., 1983). These three processes can lead to differences between measured CO_2 values and the real values of atmospheric CO_2 .

In this chapter, I discuss about gas trapping in the ice and how physical and chemical properties affect atmospheric CO_2 signals. In this chapter, in Chapter 2.1, we introduce ice core sites in Antarctica that are used in this study. In Chapter 2.2, gas trapping in the ice is introduced in detail. Then, the impact of the gas trapping process on atmospheric CO_2 signals in ice cores is discussed in Chapter 2.2. In Chapter 2.3, contamination of the atmospheric CO_2 signal in the firn due to physical and chemical processes in the firn will be discussed. Finally at a given depth, ages of the air and ice are different. This will be discussed in Chapter 2.4.

2.1. Sample selection for this study

In this thesis, EPICA Dome C (EDC) is chosen to reconstruct atmospheric CO₂ during MIS 6. Samples from the Talos Dome ice core (TALDICE) are used to test the accuracy of a new crushing system. The locations of these ice cores are plotted in Figure 2.1 and detailed information about the drilling sites is introduced in Table 2.1. The Vostok ice core, which was previously used for CO₂ reconstruction during MIS 6, is also introduced (Petit et al., 1999).

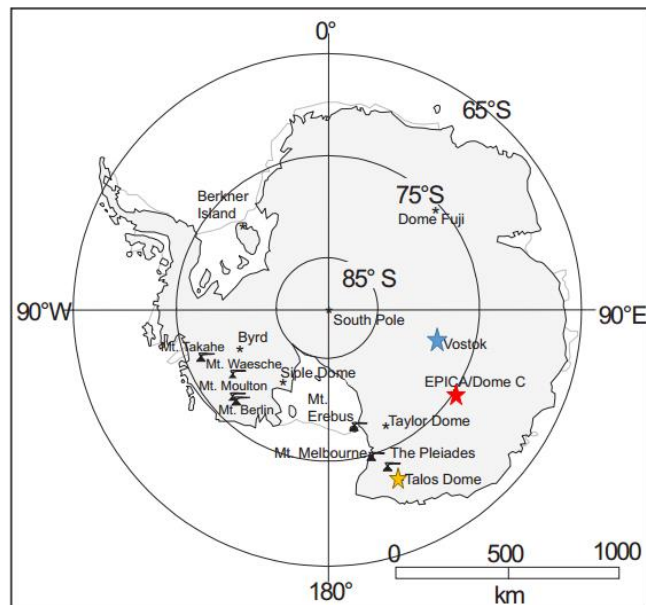


Figure 2.1. Location map of EDC (in red), Vostok (in blue) and TALDICE (in yellow), the three ice cores used and mentioned in this study (Dunbar and Kurbatov, 2011).

Table 2.1 Glaciological characteristic of Antarctic ice cores.

	EDC	Vostok	TALDICE
Latitude	75°06'S,	78°28'S,	72° 47'S,
Longitude	123°21'E	106°48'E	159° 04'E
Annual mean Temperature (°C)	-54.5	-57.3	-41
Accumulation rate (mm water equiv. yr ⁻¹)	28.5	22	80
Brittle zone depth (m)	600 – 1200	300–720	667–1002
Brittle zone ice age range (kyr BP)	29 – 84	13–50	12–35
Length of core (m)	3270.2	3667	1620
Age at bottom (kyr B.P.)	800 kyr	420 ky (for 3300m)	150 kyr
References	(Parrenin et al., 2012; Schwander et al., 2001)	(Petit et al., 1999)	(Frezzotti et al., 2004; Schilt et al., 2010)

2.2. Gas trapping in the ice

Fresh dry snow is deposited continuously on the surface in the dry snow zone of the ice sheet ice sheets i.e where no surface melting occurs. The compositional and isotopic characteristics of freshly deposited snow show annual cycles, and it is often possible to distinguish annual layers, particularly in high-accumulation areas and in the uppermost layers of snow and firn. Annual layers, however, are quickly lost due to wind-driven mixing in the low-accumulation areas of the Antarctic plateau. As snow accumulates at the sites during centuries to millennia, this accumulated powdery snow is pressed continuously under its own weight. Snow starts to compact into firn by the increase of hydrostatic pressure with depth. The snow particles become rounded and jointed together, and are thus transformed into firn (Figure 2.2). This topmost layer of the ice sheet, composed of fresh snow and low-density firn, is highly porous.

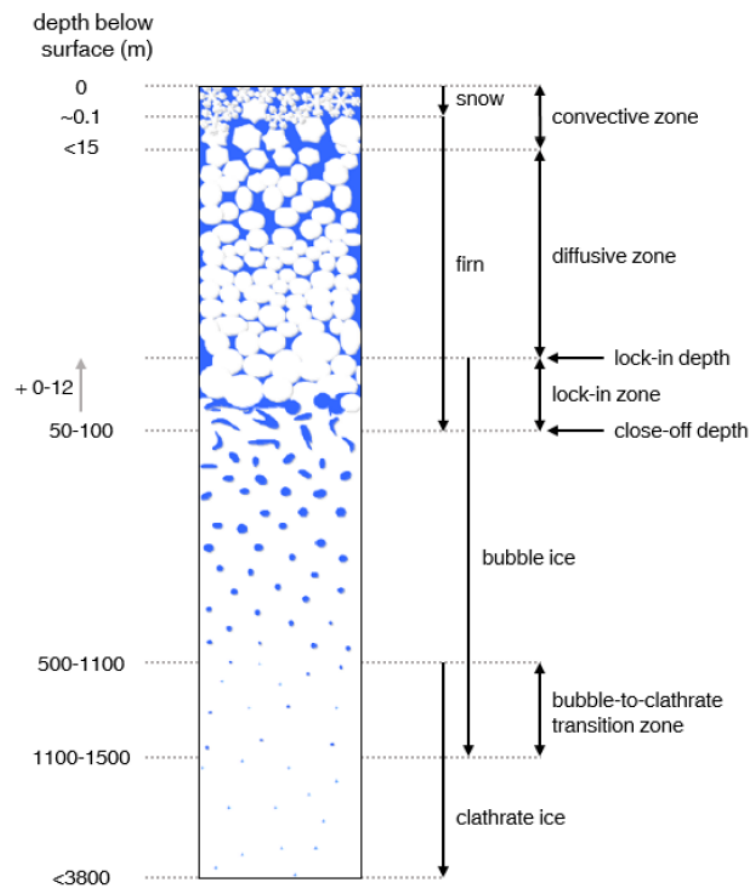


Figure 2.2. This figure shows the firm densification process and gas trapping process in the Antarctic ice sheet (Bereiter, 2012; Nehrbass-Ahles, 2017; Schwander, 1996).

The layers of firn become denser due to dry sintering and plastic deformation. As these layers become sufficiently dense, firn becomes ice (Schwander, 1989). Figure 2.2 shows the firm densification process in a polar ice sheet. The transformation of surface snow into ice layers requires between ~100 and ~6,000 yrs (Blunier et al., 2007).

Due to the absence of melt in cold polar ice sheets, air can move freely into the open pore space in the topmost part of the firn column via convection, and the air is moved into the deeper firn via diffusion and finally trapped in the ice sheet. This process can be divided into three zones (Sowers et al., 1992). The first zone is the convective zone, the highest position where air is well-mixed by the pressure gradient with respect to the surface (Clarke and Waddington, 1991). This zone usually reaches depths in the first 15 m (Landais et al., 2006; Severinghaus et al., 2010). The density of surface snow is 0.3–0.35g/cm³ (Bender et al., 1997), and the porosity of this zone is 62–67 %. Convection in the uppermost firn is affected by wind forcing. The depth of this zone can be determined in part by the wind speed and accumulation rate (Kawamura et al., 2006).

In the diffusive zone, the stagnant/static air column below the convective zone, air is moved into open pores by molecular diffusion. The movement of molecules is thus affected by temperature. In this zone, gases are still in contact with the atmosphere. When the density of the firn reaches ~0.815–~0.845 g/cm³ in the bottom of the diffusive zone, the diffusion effect decreases (Buizert et al., 2012). The air is trapped at this depth, which is called the lock-in depth (LID) (Schwander and Stauffer, 1984). The depth of the LID varies from 50 to more than 100m, which depends on the accumulation rate and the mean annual temperature. For example, the LID in Vostok varies on the order of 100 meters.

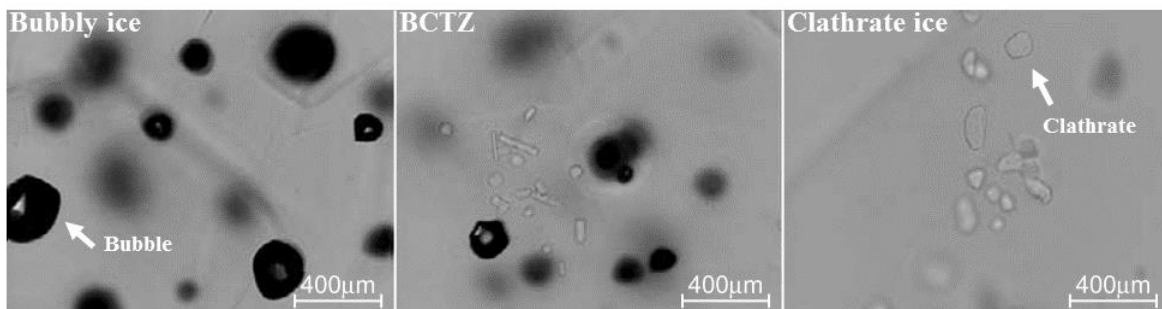


Figure 2.3. Images of air inclusions in the Dome Fuji observed under an optical microscope (Ohno et al., 2004). Left: Air bubbles above the transition zone. Middle: Bubbles and clathrates in the transition zone Right: Clathrates below the transition zone. This figure is from Ohno et al. (2004).

Below the diffusive zone is a non-diffusive zone or bubble formation zone. The height of this zone is 2~12 m, which is dependent on the seasonal snow and firn layer anisotropy. The pores between snow particles are totally isolated from each other and from the atmosphere, and form bubbles. However, additional air is occluded in pores between the lock-in depth and the close-off depth. Gas can move horizontally along permeable layers, because the firn permeability is different vertically. This interval is called the lock-in zone or pore closing zone, both of which refer to the non-diffusive transitional zone between firn and ice which is located a few meters (roughly 5-10 m) below the LID. The ice density of this zone is between 0.815~0.845 g/cm³ (Arnaud, 1997), the volume of the air is 10-15 percent. Finally, bubbles become completely trapped in the ice at the Close-off Depth (COD) which

is determined by the mean surface temperature, pressure and accumulation rates, and wind speed (Kaspers et al., 2004). Bubbly ice covers only 15 % of cores in Antarctica.

Because of the hydrostatic pressure increase at depth, bubbles are compressed in the first several hundred meters in the ice sheet. They are caged in the clathrates (Figure 2.3). If hydrostatic pressure exceeds the dissociation pressure, the air bubble is pressed into the ice lattice. The air molecules are occluded in the crystalline structure of the ice, caged in an H-bonded structure. These structures are referred to as clathrates (Ohno et al., 2010; Uchida et al., 2014). Clathrates start to be formed at around 500–1100 m. At these depths between where clathrates start to form and where bubbles disappear, bubbles and clathrates exist together (Lipenkov, 2000) (Figure 2.3). This area is called the bubble-to-clathrate transition zone (BCTZ) (Lüthi et al., 2010), or gas-clathrate transition zone (Kobashi et al., 2008). The thickness of the BCTZ is 180–700 m (Uchida et al., 2014). In the deeper part of the BCTZ, the size of the clathrates is smaller than that of the bubbles.

2.3. Physical and chemical processes affecting atmospheric CO₂ signal

2.3.1. Physical processes in the firn column affecting CO₂ value

2.3.1.1. Gravitational fractionation effect

In the topmost layer in the polar ice sheet, gas is well-mixed by wind-pumping (Clarke and Waddington, 1991). The heavier molecular species are enriched in the firn bottom due to earth's gravitational field. A gravitational fractionation effect develops with depth and mass difference between gas species (Craig et al., 1988). The gravitational fractionation effect is not related with the absolute molar mass, but rather with the difference in the masses (Δm) between two molecular species. If the height of the diffusion zone is larger, the heavier isotopes are preferentially accumulated. Thus, gravitational fractionation is highly associated with the height of the diffusion zone. The gravitational fractionation effect is therefore dependent on the temperature and accumulation rates at the site because these climate factors can impact on the firn column height. The isotopic enrichment in the LID is estimated using the barometric equation as below:

$$\delta = \left[\frac{R}{R_0} - 1 \right] \times 10^3 = \left(e^{\frac{\Delta m g}{RT}} - 1 \right) \times 1000 \cong \frac{\Delta m g Z}{RT} (\text{‰}) \quad (2.1)$$

Where R is the ideal gas constant, Δm is the absolute mass difference between the isotopes of the same species (kg/mol), g is the gravitational acceleration (9.82 m/s²), Z is the height of the diffusive column (in m), and T is the mean annual temperature in the firn (in K).

Due to the gravitational fractionation, the heavier molecules are enriched in the firn bottom. CO₂ measurement data is thus higher than real atmospheric concentrations, and the data should be corrected. The isotopic ratio of ¹⁵N/¹⁴N of N₂ and ⁴⁰Ar/³⁶Ar of in the ice can be used to estimate the amount of gravitational fractionation effect. The δ¹⁵N isotope ratio of N₂ is constant in the atmosphere on orbital time scales (Mariotti, 1983) but δ¹⁵N isotope ratio started to be biased from the upper part of the diffusion zone to the LID due to the gravity. In addition, the gravitational fractionation effect depends on the weight of the difference of two isotopic mass, and to estimate the enrichment of CO₂ we should calculate the difference between the molar mass of atmospheric CO₂ and the molar mass of air. Considering the mean molar mass of air is ~29g/mol, which is similar to the molar mass of N₂, the isotopic enrichment is estimated using the isotopic ratio of ¹⁵N/¹⁴N of N₂ in the ice, using the equations below:

$$CO_{2, \text{corr}} = CO_{2, \text{obs}} - (M_{CO_2} - M_{air}) \times \delta^{15}N \times CO_{2, \text{obs}} = CO_{2, \text{obs}} \times \left(1 - \frac{\delta^{15}N \times 15.2}{1000}\right) \quad (2.2)$$

Where M is the mass of the molecular weight of species.

However, δ¹⁵N isotope ratio data is not always available for the data correction. In this case, the δ¹⁵N isotope ratio can be estimated using an empirical relationship between deuterium data and δ¹⁵N (Dreyfus et al., 2010; Schneider, 2011). However, this is not ideal because the relationship between temperature and δ¹⁵N does not hold for some time periods (for example, MIS6 period in EDC). The equation commonly used to estimate δ¹⁵N from deuterium is as below:

$$\delta^{15}N = 0.0020032 \times \delta D + 1.2969 \quad (2.3)$$

2.3.1.2. Signal attenuation effect

The surface atmosphere is mixed with older air in the firn. Thus, air over decades to millennia, depending on the temperature and accumulation rate at the drilling site, is mixed in the firn layers (Schwander and Stauffer, 1984). In addition, the bubbles at a certain depth do not necessarily close at the same time. Thus, a signal of atmospheric CO₂ is integrated over decades to millennia, which is referred to as the smoothing effect, signal attenuation effect or damping effect. If the duration of the signal is shorter than the width of the gas age distribution, the CO₂ signal can be smoothed out. This

smoothing effect is mainly governed by the speed of porosity closure, which is highly related to accumulation and temperature. The smoothing effect is stronger for lower accumulation and/or lower temperature. This effect removes high-frequency signals and reduces the amplitude of the signal if the width of the gas age distribution in the site is broader. Figure 2.4 shows an example of smoothing effect. The atmospheric CH₄ series from Greenland (GRIP) shows a rapid change of CH₄ during the abrupt cooling event at 8.2 kyr BP. However, the atmospheric CH₄ series from EDC, which has much lower accumulation rates with respect to the GRIP site, shows a much smaller variation. CH₄ data from EPICA Dome C (EDC) is attenuated by 34 to 59 % compared to the data from GRIP.

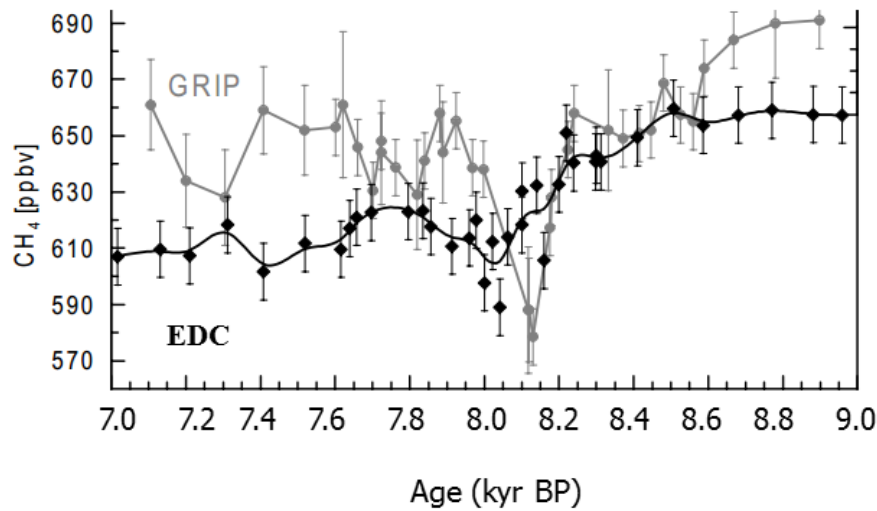


Figure 2.4. Atmospheric CO₂ from EDC and GRIP at ~ 8.2 kyr BP (Spahni et al., 2003).

2.3.1.3. Thermal diffusion effect

Gas movement is also subjected to thermal gradients within the diffusive zone. Heavier isotopes preferentially accumulate at the cooler part of the thermal gradient (Grachev and Severinghaus, 2003). If the temperature gradient is large, this phenomenon can be significant (Severinghaus et al., 2001). This mechanism, known as the thermal fractionation effect, is superimposed on the gravitational fractionation effect, and can be estimated using $\delta^{15}\text{N}$ in the occluded air. The thermal fractionation effect is described by the following equation:

$$\delta_{\tau} = \left[\left(\frac{T}{T_0} \right)^C - 1 \right] \times 1000 \quad (2.4)$$

where T is the temperature at the bottom of the diffusive column, T₀ is the temperature at the surface of the diffusive column and C is the thermal diffusion coefficient. This mechanism can be important on the CO₂ mole fraction for large temperature differences in the firn column. However this effect is not

significant on the CO₂ mole fraction (Eggleston, 2015; Schneider, 2011) because temperature gradients in interior Antarctica tend to be gradual (Jouzel et al., 2007).

2.3.1.4. Heterogeneous gas trapping

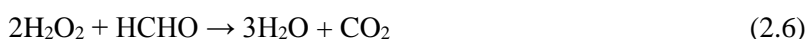
The physical characteristics of the firn column at the drilling site determine the properties of gas close off as well. Fluctuations in the density of the firn, for example, can influence close off depth. At relatively dense layers in the firn, air can be closed off earlier (Kawamura et al., 2006). Thus, some bubbles at a given layer could be enclosed earlier and at a shallower depth than the surrounding layers. In this case, the occluded air in the early close-off bubble is relatively older than those of the surrounding layers. In lower-density firn layers, bubbles can be closed off later and deeper than the bubbles in the surrounding layers, and the trapped air is thus relatively younger than air in the surrounding layers. Air is therefore not necessarily trapped in exact chronological order. This effect is thought to be larger at low accumulation sites than at higher accumulation sites (Fourteau et al., 2017). Variations in the gas trapping process can be more clearly observed when gas composition changes rapidly. This phenomenon is observed in CH₄ concentrations from Vostok 4G-2 with low accumulation on cm-scale variations at around 60 kyr BP when climate changes rapidly (Fourteau et al., 2017).

At the time of writing, no study directly addresses whether CO₂ concentrations are also affected by this mechanism. Methane concentrations vary rapidly when compared to carbon dioxide, and this effect might have a greater impact on atmospheric CH₄. On the other hand, the possibility of an impact on atmospheric CO₂ concentrations cannot be ruled out. (Nehrbass-Ahles, 2017). Since the gas trapping process can impact gas age distributions, the CO₂ signal should also be affected.

2.3.2. Chemical processes affecting gas composition in ice

2.3.2.1. Oxidation of organic molecules

CO₂ can be produced in the via oxidation of organic compounds (HCHO, CH₃COO⁻ and HCOO⁻) by an oxidizing agent such as hydroxide peroxide (H₂O₂) either biologically (Campen et al., 2003) or abiologically (Tschumi and Stauffer, 2000). The oxidation of organic molecules is described as follows:



2.3.2.2. The reaction of carbonate dust with acid in the ice

CO₂ concentrations can be contaminated by the in situ production of CO₂ caused by carbonate-acid reactions (Delmas et al., 1980). CaCO₃ and H⁺ are mainly involved in this reaction. This reaction can occur when the ice is acidic and decarbonate CaCO₃ which is present in the ice as dust particles (Smith et al., 1997a) and form CO₃²⁻. The carbonate and acid reaction is the reaction between CO₃²⁻ and protons to form CO₂. The reaction consists of two steps, which are described as below:



These reactions are reversible, and the direction of the reactions is determined by the equilibrium state of the components. For example, if the concentration of calcium ions (Ca²⁺) is higher than 70 ppb in the ice, the corresponding carbonate formed during decarbonation reacts to neutralize the existing H⁺, and the overall reaction occurs as below:



Due to this chemical reaction, atmospheric CO₂ can be depleted in principle, however, any clear evidence for the depletion in the ice where air is occluded in bubbles could not be found yet. However this depletion of atmospheric CO₂ is observed in the BTCZ (Tschumi and Stauffer, 2000).

On the other hand, if the concentration of calcium (Ca²⁺) is lower than 5 ppb at the site before ice is formed, CaCO₃ can react with H⁺, and the atmospheric CO₂ concentration cannot be contaminated in this case.

2.3.2.3. The snow melting-refreezing process

CO₂ concentration can be considerably contaminated because CO₂ is highly soluble in water compared to other gases (Neftel et al., 1983). When ice is melted, atmospheric CO₂ can be dissolved. If the melted ice freezes again at the ice coring sites, this dissolved gas in the water might be trapped in the bubbles of the ice. Thus, CO₂ concentrations are artificially increased. In addition, carbonate-acid reactions can occur in the melt water (Anklin et al., 1995).

2.3.2.4. Antarctic ice cores for CO₂ studies

Atmospheric CO₂ is usually reconstructed from the Antarctic ice cores because of higher impurities such as Ca²⁺, hydrogen peroxide H₂O₂ and formaldehyde HCHO in Greenland ice core. As

mentioned above, these impurities can cause carbonate-acid reaction and the oxidation of organic carbon. This can cause large scattering of atmospheric CO₂ data. Some examples on CO₂ production in Greenland are as below:

CO₂ records from Antarctic ice core agree with those from Greenland within age uncertainties and analytical uncertainties during the last 300 yrs. However at the beginning of the second millennium, atmospheric CO₂ concentrations reconstructed from Greenland ice cores (Eurocore and GRIP) is higher than those from Antarctic ice core by up to 20 ppmv during the millennium. Considering the inter-hemispheric gradient effect might be between - 1 and + 5ppmv (Anklin et al., 1995), this difference might be partially related with interhemispheric gradient but it is mostly caused by chemical reaction in the ice. This is confirmed by the amount of impurities in Greenland ice and the Antarctic ice (Barnola et al., 1995). In addition, during the last glacial period, atmospheric CO₂ in Greenland during the interstadial is higher than those during the stadial by 50-90 ppmv on average (Smith et al., 1997), however this high variations during the last glacial period were not observed in Antarctic ice cores (Oeschger et al., 1988).

Thus to obtain less in situ CO₂ production in ice, a low carbonate concentration and H₂O₂ in an ice core are important. Luckily, Antarctic ice cores have relatively low concentrations of H₂O₂ and carbonates and have low temperature compared to Greenlandic ice cores, which can reduce the risk of CO₂ contamination (Tschumi and Stauffer, 2000).

2.4. Gas age calculation challenge

At equivalent depth in an ice core, the age of the air is younger than the age of the surrounding ice. Thus, ice cores have different chronologies for the air and ice phases. The difference between the age of the air and ice at a given depth is referred to as delta age (Δ age); the analogous difference in depth between air and ice with the same age is referred to as delta depth (Δ depth). If the gas trapping process occurs slowly, as is the case at the low-accumulation drilling sites in the Antarctic interior, Δ age is larger.

Δ age is usually calculated by firn densification models which usually take into account temperature, accumulation rate, wind speed and insolation change. To improve the relative chronology between ice and gas, delta depth between gas and ice can also be calculated using $\delta^{15}\text{N}$ data, which reflects the height of the diffusive column. From $\delta^{15}\text{N}$ data, the depth difference between synchronous events in the ice matrix and gas bubbles is estimated. The uncertainties of the $\delta^{15}\text{N}$ method are often smaller than those of modelling or orbital wiggle-matching. In this thesis, we use a Δ age calculation to improve the chronology of EDC during MIS 6, and this revision is treated in greater detail in Chapter 6.

Chapter 3

Introduction to gas extraction methods

Reconstructing atmospheric variability of CO₂ from natural ice is challenging for different reasons. As discussed in the previous Chapter, physical processes (particularly the layering of the trapped gas and the formation of clathrates) and chemical processes (in situ reactions, CO₂ dissolution) may affect the measurement. The small amount of air sample available (only ~10 % of the volume of an ice core (i.e. ~100 cm³ at standard pressure and temperature in 1 kg of Antarctic ice core sample) make the measurement even more challenging. In addition, because of the small amount of gas extracted, contaminations due to desorption and adsorption of CO₂ in the measurement line and at the surface of cell containing samples may easily occur (Zumbrunn et al., 1982). Thus, developing an optimal methodology is important to observe small variations of atmospheric CO₂.

Attempts to reconstruct atmospheric CO₂ concentrations from ice cores have relied so far on discrete measurements, using either wet extraction (Kawamura et al., 2003), crushing extraction (Ahn et al., 2009; Bereiter et al., 2013) or sublimation extraction (Schmitt et al., 2011). In Chapter 3.1, these different extraction techniques are described (Table 3.1). Four aspects are mainly discussed here, which are important factors to select how to measure data: internal contamination caused by the technique, sample size, extraction efficiency and sample throughput (amount of samples measured in a day). The new crushing extraction system, Ring system, characterized in this work of thesis is not described here, but fully discussed in chapter 5. In Chapter 3.2, application of extraction methods on different ice types is introduced.

3.1. Wet extraction

Wet extraction would be the easiest way for reconstructing atmospheric CO₂ from the polar ice cores. This method is usually used to reconstruct CH₄, N₂O, CO concentrations, $\delta^{15}\text{N}$ of N₂, $\delta^{18}\text{O}$ of O₂, the isotope of O₂/N₂, the isotopes of CH₄ and total air content (Bock et al., 2010; Capron et al., 2010; Landais et al., 2012; Schilt et al., 2010; Sowers et al., 1997) (Figure 3.1). The wet extraction system described here was developed for CO₂ at the Japanese National Institute of Polar Research (NIPR) (Kawamura et al., 2003).

In this method, air bubbles are extracted from the ice by melting the sample in a vacuum chamber. While the ice is heated in a warm water bath, air is released from the ice and passed through two cold traps at -100°C for water vapour removal (Nakazawa et al., 1993). Then, the extracted gas is collected in a sample tube at -269°C . Less than 10 min are required to melt the 300–350 g of the ice and collect the air. Afterward, the sample tube is left at ambient temperature over night to make sure the air components are well mixed, and the gas is then analysed by gas chromatography (GC). 3–4 samples a day can be measured (Kawamura et al., 2003).

This system shows 100 % extraction efficiency on clathrate and bubbly ice. In addition, short time is required to melt and collect the gas, thus, the possibilities of atmospheric CO_2 contamination caused by adsorption and desorption and water–gas interactions can in principle be reduced. However, during the melting phase, CO_2 can be artificially produced via carbonate–acid reactions in the ice core ($2\text{H}^+ + \text{CO}_3^{2-} \rightarrow \text{CO}_2 + \text{H}_2\text{O}$) and/or via oxidation of organic material (Anklin et al., 1995; Kawamura et al., 2003; Stauffer and Tschumi, 2000). Moreover, CO_2 dissolves in the meltwater in a larger amount with respect to other main atmospheric gases (Sowers and Jubenville, 2000). This method provided limited success using the Dome Fuji ice core, which, relative to Greenland and coastal Antarctic ice cores, contains lower amounts of chemical impurities and dust concentration (Kawamura et al., 2003). However, the CO_2 dataset from the Dome Fuji ice core is still offset from other dry gas extraction datasets by up to 20 ppmv, which might be related with a reaction of carbonates with the melt water (Kawamura et al., 2003). Thus, the melt extraction technique is not qualified to produce high precision CO_2 data; and there are still doubts on extracting gas from the wet extraction system.



Figure 3.1. Pictures of the melting extraction system for atmospheric CH_4 concentrations at Seoul National University (SNU) (Photos courtesy of J. Ahn). On the left, the ice sample stored in the chamber before melting. On the right, the multiple chambers containing the melted samples. The principle of wet extraction for CH_4 is similar to that for CO_2 .

3.2. Sublimation system

The sublimation method consists of extracting the air from the ice using a direct conversion from solid to gaseous phase without passing through the intermediate liquid state (Figure 3.2). In the sublimation system developed at the University of Bern (UBern), a 30 g ice sample is sublimated with an IR lamp under low pressure (below 4.6 mmHg) (Schmitt et al., 2011) (Figure 3.2). The sample is placed in a glass container above an IR lamp for 50 min. Then, the air bubbles liberated from the ice are flushed through a water trap at -150°C and collected in a glass tube at liquid helium temperature. The glass tube is then warmed to release the air, which is analysed by mass spectrometry.

The sublimation method for CO_2 enables 100 % extraction efficiency for both bubbly ice and clathrates. In addition, it minimize the risk of possible reactions in liquid water as well as artefacts due to sample contamination. However, the overall processing time is about 4 hours per sample, which represents the major limitation of this method (Schmitt et al., 2011). In addition, the extraction of one sample takes ~ 50 minutes, which is an order of magnitude higher than the time required for the dry gas extraction system (~ 5 min) or wet extraction system (~ 10 min). During the long processing time, CO_2 desorbed from the surfaces of the sublimation system can be released (Zumbrunn et al., 1982), leading to a contamination of the measurement. However, Zumbrunn et al. (1982) stated that, due to different material, adsorption and desorption effects from glass sublimation vessels are less pronounced than those from the dry gas extraction systems, which are generally made of stainless steel. Last, a quasi-

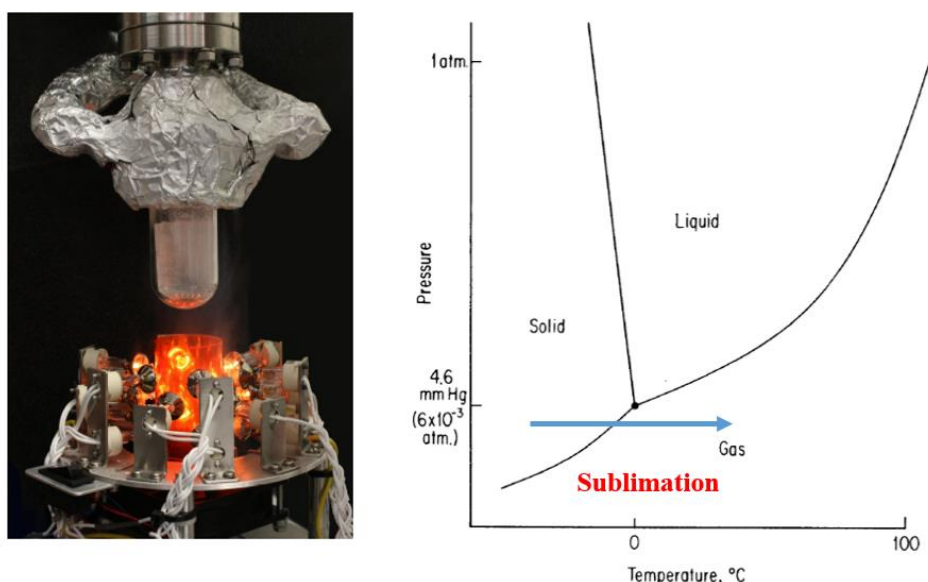


Figure 3.2. In the picture on the left the sublimation system. The glass bulb containing the sample is placed above an IR lamp (Schmitt et al., 2011). The plot on the right illustrates the phase diagram for water. Below 4.6 mmHg, water sublimates rather than melt (Wilson and Donahue, 1989).

liquid layer can form when the ice sample is sublimated at the ice melting point, in which CO₂ concentrations can be altered by chemical reaction (Lourantou, 2008).

3.3. Dry extraction

Ice core CO₂ studies most commonly use dry gas extraction systems. The principle of dry gas extraction consists of pulverizing the ice mechanically in order to extract air without melting the ice under vacuum. The extracted gas is analysed. Several pulverisation methods have been developed for CO₂ extraction. This section introduces three types of pulverisation systems: ball mill, needle cracker and centrifugal ice microtome. In this section, a comparison of measurements made using these three systems is presented. Two other pulverisation-style extraction methods are not treated in this chapter: the cheese grater (Etheridge et al., 1988) and micro-crusher systems (Wahlen et al., 1991). Readers are referred to the citations for further details.

3.3.1. Ball mill

The first CO₂ concentration measurements were obtained from the ball mill system developed by Delmas et al. (1980) at IGE. In this system, an ice sample is placed in a 150 cm³ chamber with five small balls and three large balls (8 and 12 mm diameter, respectively) (Figure 3.3). ~ 40g ice samples are used for a single measurement. A vertical crusher agitates the chamber with an up-down linear



Figure 3.3. The ball mill chamber where an ice sample is crushed containing the eight stainless-steel balls (left) and the vertical crusher (right) located in a walk-in freezer.

motion, at a speed of 100 cycles per minute in a walk-in freezer at -20°C (Figure 3). The balls of varying diameter liberate the air bubbles trapped the ice sample. After crushing, the chamber is attached to the measurement line where the extracted gas is expanded and analysed by gas chromatography (GC). The

ball mill shows extraction efficiencies of ~62% for bubbles and ~52% for clathrates on average (Schaefer et al., 2011). 3–4 samples per day can be measured. Prior to this thesis, the precision of the ball mill method was ~ 1.5 ppmv previously (1σ) (Lourantou, 2008). During this thesis, the precision of the method was further improved to 1 ppmv. This system and the improvements made will be discussed more in detail in chapter 4. The ball mill system presents sources of contamination similar to those of other dry gas extraction methods. While crushing a sample in a freezer, the extraction chamber must be detached from the measurement line. The inlet is protected with parafilm in order to minimize contamination from ambient air and condensation of water vapour, but it is not possible to completely prevent the movement of ambient air. The flexible pipe connecting the chamber may be contaminated by ambient air during the crushing. In addition, atmospheric CO₂ can be contaminated by surface adsorption and desorption in the chamber while waiting for the measurement line to be vacuumed (for 10 min) before GC measurements.

3.3.2. Needle cracker

The needle cracker method was developed by Zumbunn et al. (1982) and Neftel et al. (1982) at the University of Bern (UBern). Modified needle crackers have been developed at Oregon State University (OSU) and Seoul National University (SNU). In this section, the needle cracker at SNU is described.



Figure 3.4. The picture on the right shows the dry extraction system line at SNU. The red box indicates the six sample tubes stored in He-closed cycled refrigerator at ~10.5 K. The picture on the right show the needle crusher and the chamber where an ice sample is stored.

The principle of this system consists in extracting gas from the ice in a double walled vacuum chamber with a certain number (91 at OSU) of steel needles installed in the upper part of chamber (Figure 3.4). The needles installed in the upper chamber repeatedly pierce the ice sample with an up-

down linear motion (Ahn et al., 2009). While air is extracted, the chamber is maintained at -35°C to -40°C to prevent ice sample from melting. The extracted gas is collected and condensed in a stainless-steel sample tube which is placed in a cryogenic system at $\sim 10.5\text{ K}$. The collected air is analysed by GC. CO_2 can be reconstructed with a small sample size (8–15 g at SNU and 7 g at UBern), thus allowing replicates from the same depth layer in a relatively easy manner. The precision of the system is $\sim 1\text{ ppmv}$ at SNU and 2.5 ppmv at UBern (Ahn et al., 2009; Indermühle et al., 1999). 6 and 12–20 samples per day are measured at SNU, and UBern, respectively. At SNU, extraction efficiency for an 8–15 g bubbly ice sample is $\sim 85\%$, extraction efficiency for a clathrate ice sample is below 80% (Ahn et al., 2009). The extraction efficiencies are $\sim 70\%$ for bubbly ice and $\sim 50\%$ for clathrate ice at UBern (Bereiter, 2012; Indermühle et al., 1999).

The advantage of the needle crusher is the small sample size required for a single measurement, important for the analysis of old ice as well as for the possibility to perform replicates from the same depth interval and therefore better statistics. However, the amount of possible contamination is high with respect to the total amount of air contained in the sample, making measurements sensitive to small amounts contaminations. In order to handle at best all possible analytical errors, blank tests using artificial ice and standard gas should be conducted regularly. Additionally, because of the non-homogeneity of the ice matrix, small sample sizes are not always well-adapted and may require several duplicates in order to understand a given atmospheric scenario.

3.3.3. Centrifugal Ice Microtome (CIM)

The Centrifugal Ice Microtome method was developed by Bereiter et al. (2013) at UBern to overcome the limitations of the needle crusher. The aim of this system was to improve the extraction efficiency, maximize the possible sample throughput, minimize mechanical friction in the device and minimize inner area of the chamber. Today, most of the CO_2 measurements at UBern are performed using the CIM method.

In the CIM system (10 cm diameter microtome), the gas is extracted by shaving the ice using centrifugal force and a magnetic bearing. Ice is placed in the sample holder in a vacuum chamber at -27°C and is rotated anti-clockwise by magnetic bearings with a speed of up to 2000 rotations per minute. The ice is pushed in the direction of the inner mantle surface by the centrifugal force, and shaved by a shaver knife installed at the bottom of the mantle (Figure 3.5). The sample holder is rotated until the ice is completely pulverized. Then, the extracted gas is injected into an optical gas analyser. Except for loading samples and cleaning the powdery ice produced by shaving ice, all steps are operated automatically. The precision of this method is $\sim 1\text{ ppmv}$ (Nehrbass-Ahles, 2017). It can measure up to ~ 20 samples a day which is the maximum sample throughput of all existing analytical CO_2 systems for

ice core studies, requiring small sample size (~3–15g) and high extraction efficiency (~95 % for bubbly ice and ~90 % for clathrate ice) (Bereiter, 2012). 3 replicates are made from each given depth interval (Nehrbass-Ahles, 2017). However, this system presents drawbacks similar to those of the needle cracker, due to the small sample size.

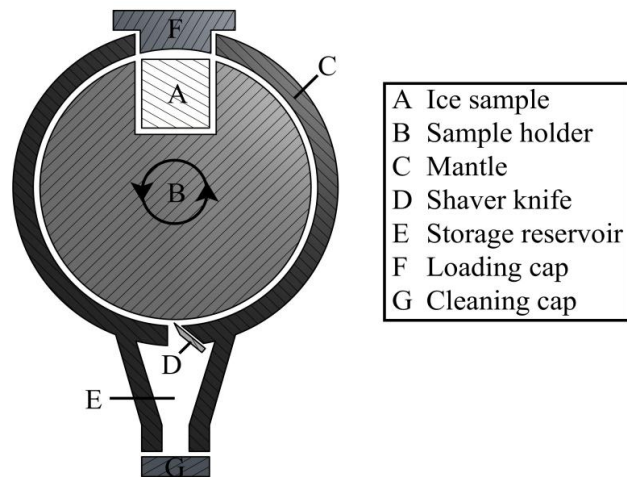


Figure 3.5. This illustration shows a cross section of the CIM dry extraction system. Letters show the parts of the device. Image adapted from Bereiter et al. (2013). The ice sample (A) is placed in the sample holder and crushed by a shaver knife (D) fixed on the mantle (C). The sample is rotating in a anti-clockwise direction and the produced powdery ice is stored in storage reservoir (E).

3.3.4. Drawbacks of dry extraction

Dry extraction systems allow to reconstruct CO₂ data easily with high precision and high work efficiency in comparison with wet and sublimation systems. However, in contrast with those, the extraction efficiency of dry gas extraction systems depends on the physical properties of the ice (e.g., bubbly, clathrate or a mix between the two) and it does not reach 100%. Existing dry extraction methods show 60–95 % extraction efficiency for bubbly ice and 50–90 % extraction efficiency for fully clathrate ice (Ahn et al., 2009; Bereiter et al., 2013; Lüthi et al., 2010; Sowers and Jubenville, 2000). This difference of efficiency for different physical properties leads to bias on the absolute CO₂ concentrations. This point will be discussed more in detail in Chapter 3.4.

3.4. Application of extraction methods on different ice types

Air can be extracted from bubbly ice easily because, when the bubble is opened, the air is instantaneously released. Thus, even when using different extraction systems, atmospheric CO₂ reconstructed from bubbly ice in the same core shows negligible offsets, mainly affected by different extraction efficiencies and possible contaminations of the sample.

In contrast with bubbly ice, releasing gas from clathrates is more challenging. When crushed, clathrate ice does not release air instantaneously, but rather following an exponential trend. Thus, if the extraction efficiency of a system is much lower for clathrate ice, it can be improved by waiting for additional air to be released (this is the case for the needle crusher, for example) (Ahn et al., 2009). Once the extraction efficiency is optimized, the CO₂ offsets between different measurement systems are negligible. On the other hand, when the air is extracted from the depth where bubble and clathrates co-exist, the so called Bubble–Clathrate Transformation Zone (BCTZ) (Chapter 2.2), different extraction efficiencies can lead to biased CO₂ concentrations when measured using dry extraction methods which have different extraction efficiencies on bubbly and clathrate ice (Lüthi et al., 2010; Schaefer et al., 2011). During clathrate formation, the gas is partitioned into clathrates due to the different gas diffusivities and solubilities (Salamatin et al., 2001). Thus during clathrate formation, CO₂ has consistently been observed to be depleted in bubbles and enriched in clathrates, although, the physical processes responsible for this enrichment are still under debate (Schaefer et al., 2011). Degassing from clathrates takes much longer than air release from bubbles; thus, if air from the clathrate ice is not extracted entirely, CO₂ concentrations can be biased.

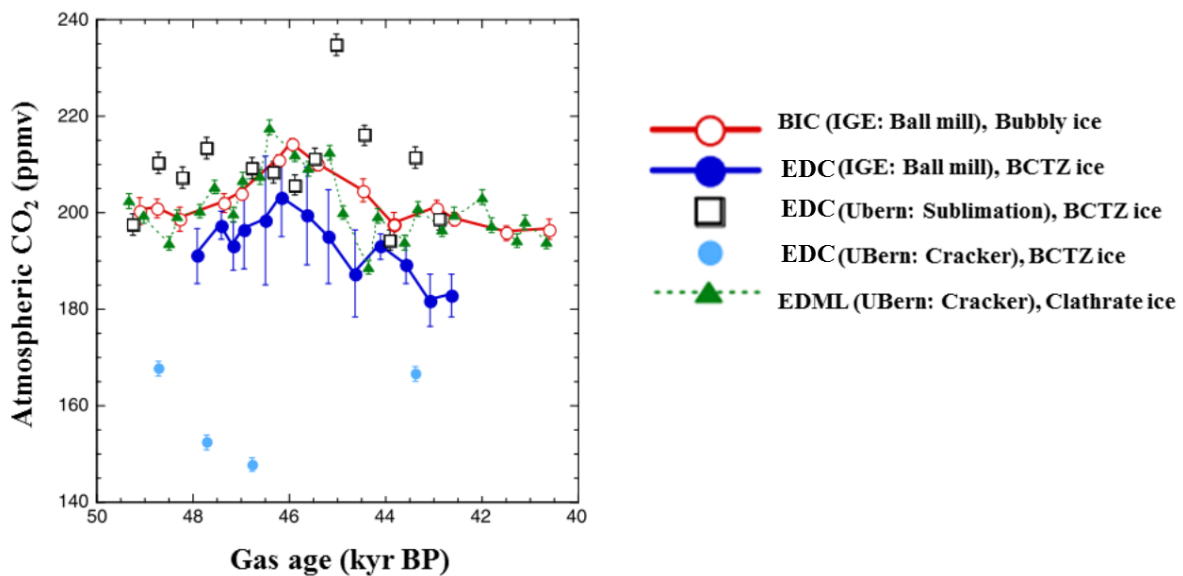


Figure 3.6. CO₂ concentrations from bubbly (BIC), clathrated (EDML), and BCTZ (EDC) ice measured by different extraction methods. Red circles and dark blue circles show atmospheric CO₂ concentrations reconstructed by ball mill from bubbly ice (BIC) and BCTZ (EDC) respectively (Schaefer et al., 2011).

Figure 3.6 illustrates how different extraction efficiencies impact data quality. CO₂ concentrations were measured from ice core from different sites. Different ice samples of the same age are therefore obtained: bubbly (Byrd ice core; hereafter BIC), clathrate (EPICA Dronning Maud Land; hereafter EDML), and BCTZ (EPICA Dome C; hereafter EDC) ice sample. Three different extraction methods were employed: ball mill at IGE, needle cracker and sublimation methods at UBern. When

CO₂ is reconstructed using the ball mill system, concentrations progressively increase from the first to the last injection into the GC. This is due to the delay of air release from the clathrates. Thus, CO₂ concentration is biased in the BCTZ, and data precision is compromised. In addition, CO₂ concentrations from bubbly ice are positively offset with respect to those measured in BCTZ ice. These results show that due to the different extraction efficiencies for bubbles and clathrates, CO₂ data can be biased and data precision is low when CO₂ is reconstructed using the ball mill method in the BCTZ.

For the needle cracker at UBern, the difference between extraction efficiencies on bubbly ice and clathrate ice is 20 %, which represents the largest difference among dry gas extraction systems. This limits the measurement precision for the EDC ice core. In figure 3.6, Atmospheric CO₂ concentrations from EDC measured with needle cracker at UBern (light blue) are much lower than those measured at IGE (dark blue). CO₂ data from the sublimation method are assumed to best reflect the absolute atmospheric CO₂ concentrations. However, data shown here, measured from the BCTZ and the uppermost clathrate zone using sublimation, show large scatter suggesting that clathrate layers also pose problems with the sublimation technique (Lüthi et al., 2010).

Table 3.1. Summary of various extraction methods discussed in this Chapter

Extraction principle		Dry extraction			Sublimation	Wet extraction	
		Ball mill	CIM	Needle cracker			
Lab		IGE	UBern	UBern	OSU/SNU	UBern	NIPR
Sample size [g]		40	3-15	7	8-15	30	300
Precision [ppmv]		~1	~1	2.5	~1	2	1.5
Extraction efficiency	Bubble [%]	~62	≥ ~95	~70	~85	~100	~100
	Clathrates [%]	~52	≥ ~90	~50	≤ ~80	~100	~100
Sample throughput (per day)		3-4	12-20	12-20	6	2	3-4
Number of replicates		1	3	4	7	1-2	1
Analysis method		GC	Optical gas analyser	laser absorption spectroscopy	GC	mass spectrometry	GC
Reference		This study; Schaefer et al. (2011); Lourantou (2008)	Nehrbass-Ahles (2017); Bereiter et al. (2013)	Lüthi et al. (2008); Indermühle et al. (1999)	Ahn and Brook (2014); Ahn et al. (2009)	Eggleston et al. (2016); Schmitt et al. (2011)	Kawamura et al. (2003)

Chapter 4

Improvement in the precision of the existing extraction method: the ball mill system

The main goal of this thesis is to understand atmospheric CO₂ variabilities on millennial time scales during the MIS 6 period (185 kyr BP–135 kyr BP) and its comparison with atmospheric CO₂ during the last glacial period. To reach this goal, high precision measurements are demanded. For example, previous studies of the last glacial period show that when the duration of North Atlantic stadial is short, CO₂ varied by less than 5 ppmv (Ahn and Brook, 2014). Therefore to observe how atmospheric CO₂ variability is related with climate change on millennial time scales during the MIS 6 period, a precision of less than 2 ppmv is required.

CO₂ concentrations during MIS 6 were reconstructed by the method developed at IGE about 40 years ago, the ball mill system, which already experienced a significant improvement during the time period 2009–2010 when partial automation was setup. The precision of the system was evaluated in the frame of this PhD by conducting blank tests, before conducting the MIS 6 measurements. Three problems were highlighted, associated with the previous methodology: no correction for contamination was applied before whereas we found a significant term; the precision of the ball mill system was not optimal to observe small variabilities; sample throughput was limited to two measurements per day. These three problems have been solved or improved, thus, the overall procedure was revised in this thesis.

In this chapter, in Chapter 4.1, the existing dry gas extraction system, referred to as the ball system, and the Gas chromatography (GC) used for the gas analysis are introduced in detail. Then, the improved experimental procedure for each step is presented in Chapter 4.2. We improved the existing measurement system and revised the calculation during the first two years: We also increased the number of measurements possible per day, improved the measurement precision, and developed a method to calculate absolute CO₂ concentration values. These improvements are presented in Chapter 4.3. The conclusion of this Chapter is provided in Chapter 4.4.

4.1. Ball mill system and Gas chromatography analysis

The CO₂ measurement process at IGE can be divided into 2 parts: a gas extraction and a gas analysis part (Figure 4.1). The extraction system is used to pulverize the samples to liberate the air from the ice. This extracted air from the ice moves into a transfer line and then to a GC via a sample loop.

The gas is then analysed by GC. In this section, the ball mill extraction system and analysis parts are presented in detail.

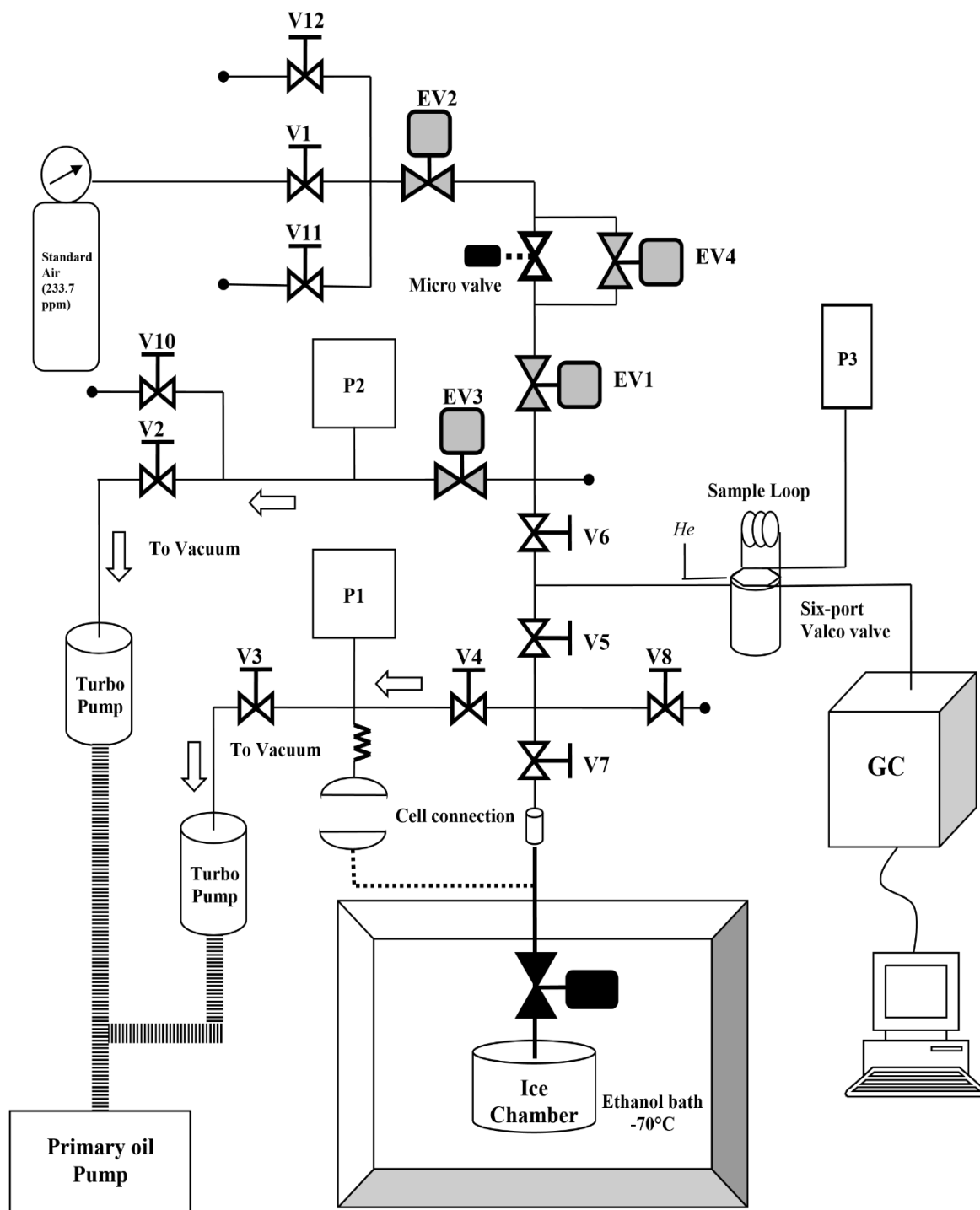


Figure 4.1. Schematic diagram showing the dry extraction line and GC at IGE. Arrows indicate the direction of the gas flow toward vacuum. V and EV indicate manual Valve and Electronic Valve respectively. P indicates pressure gauges.

4.1.1. The dry extraction

The dry extraction setup consists of four main parts: a vacuum system, an ice chamber system, a vertical crusher and an ethanol bath (Figure 4.1). The vacuum system is to remove ambient air from the chamber and in the whole vacuum line. It is composed of 2 turbo-molecular pumps (Pfeiffer Vacuum TMH 071 P) coupled with a primary oil pump (Pfeiffer Vacuum DUO 10M). 3 pressure gauges connected to the sample line allow us to monitor the vacuum and/or pressure conditions. Two pressure gauges (P1 and P2 in Figure 4.1, Pirani gauge providing a qualitative measurement) are installed in between each pump and the CO₂ measurement line and 1 pressure gauge (P3 in Figure 4.1, MKS Instrument MKS 690a 13TRA called Baratron gauge) is installed in front of sample loop. P3 accurately measures the pressure of the gas which is injected into the GC, through membrane deformation. The accuracy of the Baratron gauge MKS 690a 13TRA is $\pm 0.05\%$. The gas pressure of the sample loop is affected by temperature according to the gas law. Thus, the room temperature – and thus of the sample loop – is controlled by air conditioning at $20 \pm 2^\circ\text{C}$.

The ice chamber – called the ball mill system – is a leak proof stainless steel container where the ice sample (~40g) is stored together with five small stainless steel balls and three large stainless steel balls (8 and 12 mm diameter, respectively, Figure 3.3). The inner volume of the cell is 150 cm³. The ball mill cover includes a threaded plug through which the gas can flow, limiting the transfer of ice powder into the analytical system following ice crushing. A manual valve Nupro SS4H allows to isolate the ice chamber from the atmosphere or from the analytical line. In the IGE lab, there are five chambers made so far, and are numbered. In this thesis, we used three ball cells (chamber #1, 4, and 5), while chamber # 2 and 3 were left aside because these two chambers were broken. The chamber is detachable from the extraction line. The chamber is connected to the line when ambient air in the chamber is removed before crushing a sample and when the extracted air from the ice is analysed by GC. When the chamber is connected to the measurement line, the chamber is stored in an ethanol bath maintained at about -60 to -70°C to protect the ice sample from melting and to be used as a water trap as well. Once immersed in the ethanol bath, the valve of the chamber is manually or closed with a tongue and groove pliers (KING TONY 345122DG).

Each ice sample is crushed by attaching the sample container to a vertical crusher, with an up-down linear motion, at a speed of 100 cycles per minute (Figure 3.3). The vertical crusher is located in a freezer at $-18 \pm 2^\circ\text{C}$ to protect the ice sample from melting.

4.1.2. The analytical line system

The analysis part consists of the gas transfer line and GC (Figure 4.1). The gas line is connected to a standard gas tank. In the gas transfer line, 12 manual valves (Bellows-Sealed Nupro Valves,

hereafter V) and 4 electronic valves (Nupro Stainless Steel Bellows Sealed Valve, SS-4BK-1C, hereafter EV) are installed to control the flow of gas. The entire gas (or sample) line is made of electro polished stainless steel with a 1/4" diameter, except the sample loop having a 1/8" diameter. V has a stainless steel stem tip pressing against a Kel-F Teflon seat and is made of electro polished stainless steel, which can be handled manually. Manual valves are used to handle the air which is stored in a chamber.

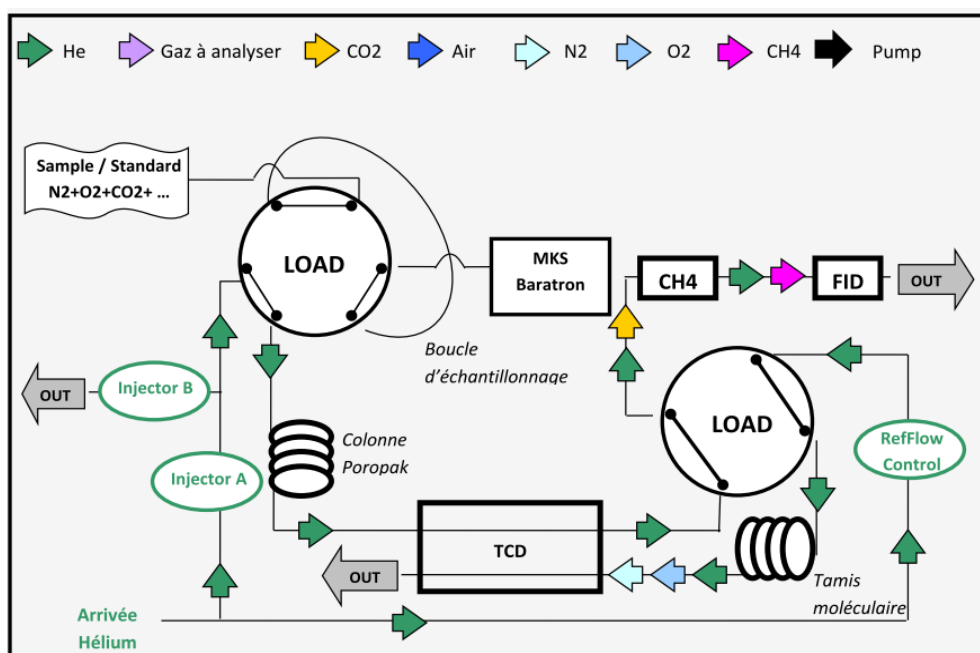


Figure 4.2. Diagram of a gas chromatograph at IGE. This diagram shows after the gas is separated into Air ($N_2 + O_2$) and CO_2 , how air and CO_2 move into a TCD and a FID respectively. The arrows indicate the movement of the air components.

Table 4.1. Settings for gas chromatography at IGE

Carrier gas (He) flow rate	VICI 4 way, Inject	25.8 ml/mn
	VICI 4 way, Load	65 ml/mn
Sample loop volume		1 cm ³
Length of sample loop		1 m
Oven temperature		80°C
Column packing material		Porapak N
Column mesh		80/100
Column line material		Electropolished stainless steel
Column length		2m
Column internal diameter		0.069 inch

EVs are activated when a calibration of the GC response is performed. The switch positions of EVs are controlled by a homemade LabVIEW programme. EV1 is used to inject the gas into the measurement line. EV2 is a supply line of standard gas. V1, installed in front of the standard gas line, is always opened, thus when EV2 is open, standard gas can be injected into the line. EV3 is used to vacuum the line. EV4 is a bypass valve used to eliminate the remaining standard gas in the line. An Air-Liquide metering valve is installed between EV1 and EV3 to adjust the flow of the standard gas into the analysis line. The GC is a device for qualitative and quantitative analysis of multi-component gases. GC separates and analyses the gas analytes by distributing the different gas molecules between a stationary phase and a mobile phase. The analytes are mixed with a carrier gas (the mobile phase) and they pass through a separation tubing (containing the stationary phase, in our case Porapak N 80/100 mesh). The speed of gases throughout the entire column differs depending on the affinity of each gas species with the stationary phase; therefore, the components are sorted out sequentially through the outlet of the column. In our case, the extracted gas from the ice is separated into Air (N_2+O_2+Ar) and CO_2 . Air (N_2+O_2+Ar) having a lower affinity than CO_2 for Porapak N. When exiting the chromatographic column, air (N_2 , O_2 and Ar) is transported by the carrier gas through a Thermal

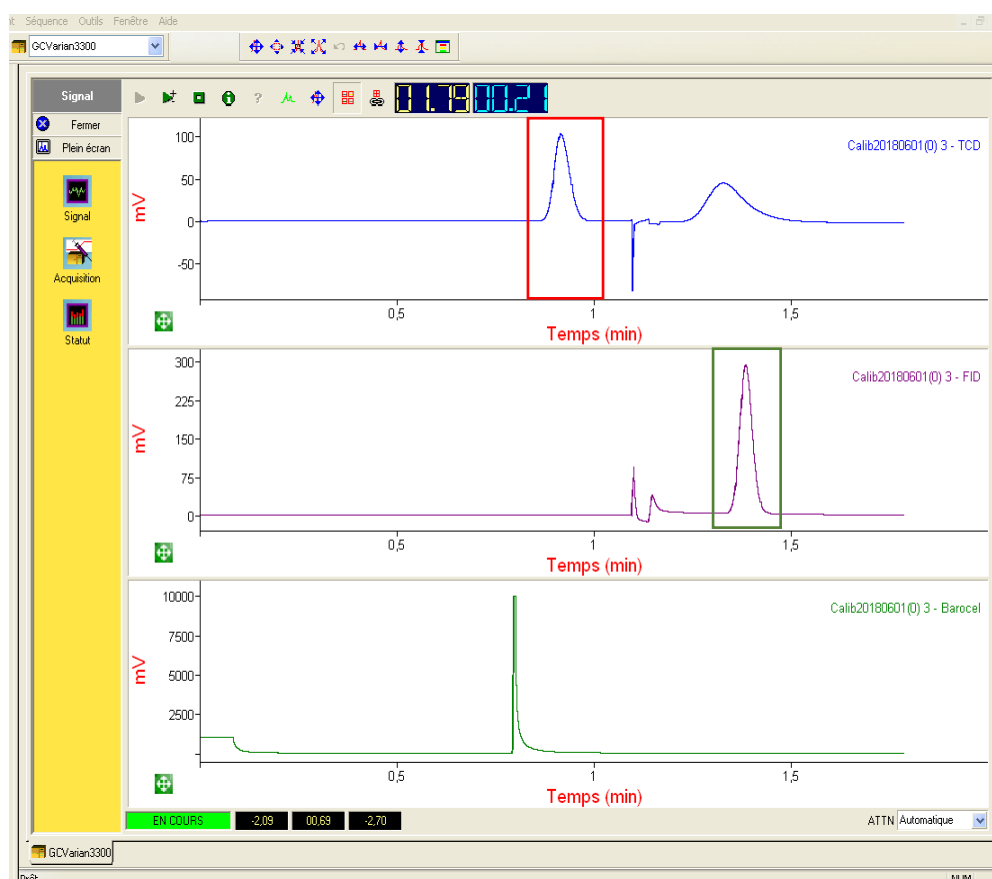


Figure 4.3. AZUR program. This figure shows how the TCD (Top), FID (middle) and Baratron (bottom) signals look like when a sample is measured for 2 min 30 sec. Red (green) square indicates the time range used for calculating the area of air and of CO_2 , respectively.

Conductivity Detector (TCD, Figure 4.2). The TCD detects the changes in the heat loss rate of a column effluent and compares it with a reference flow of pure carrier gas; it depends on the difference of heat capacity of the analyte with respect to the carrier gas. CO₂ is converted to CH₄ on a hot nickel catalyst fed with pure hydrogen, and is carried through a Flame Ionization Detector (FID) (Figure 4.2). Methane is combusted in the FID through a hydrogen air flame, and electrodes are used to detect the quantity of ionized carbon produced during combustion. The concentration of CO₂ is determined through calibration of the FID response when varying amounts of a reference gas is injected into the GC column.

A Varian 3300 GC is used at IGE (Barnola et al., 1983; Bellier, 2004; Laurantou, 2008; Pepin, 2000). Helium is used as the carrier gas. The GC settings used for the experiment are summarized in Table 4.1. 2 min 30 sec is required for a single measurement.

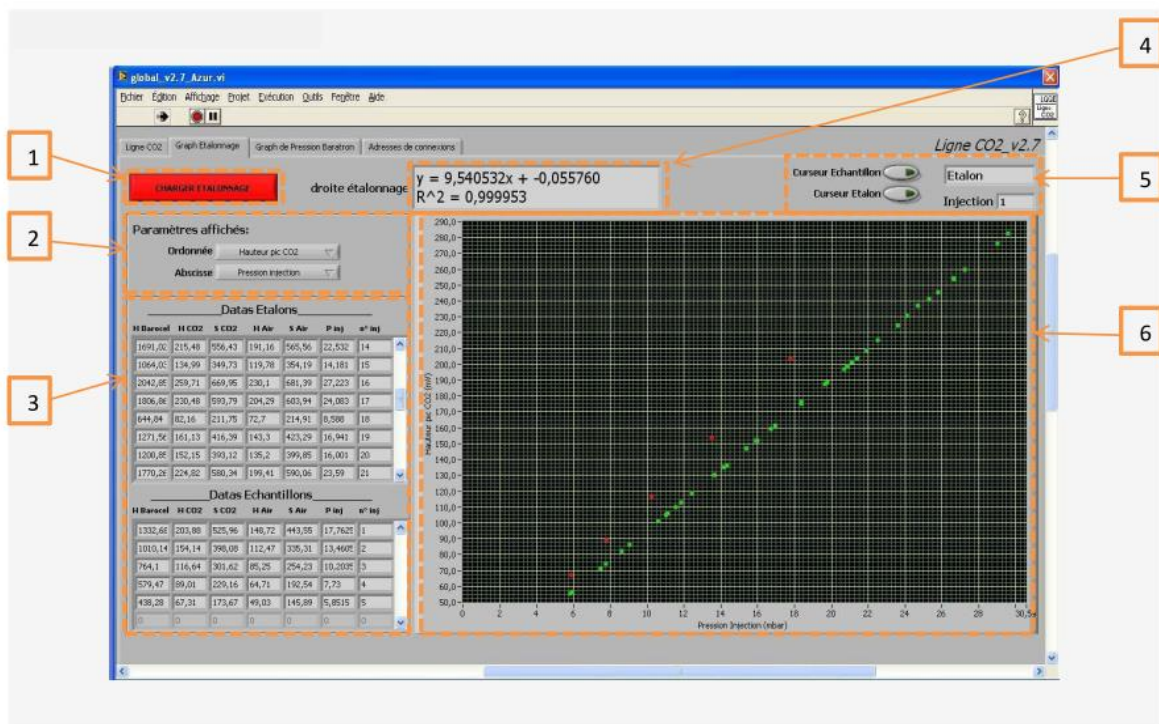


Figure 4.4. A LabVIEW program. (1) A button is to insert a data file produced by LabVIEW into the program to plot data set and a calibration curve in this program. (2) The selection of parameters for x and y axes. Among 6 parameters, one parameter can be chosen for each axis: the height of air, the height of CO₂, the area of air, the area of CO₂, the pressure of the injection and Barocel. (3) The table containing the information of samples and a calibration curve. (4) The linear regression equation (ax+b), which is estimated for the calibration curve. (5) The information of the selected point in the graph (6) A graph with the calibration curve and CO₂ data. The calibration curve is in green and CO₂ data in red.

The calibration curve obtained by GC can be viewed in real time via a commercial software called Azur. Figure 4.3 shows the variation of the TCD, FID and Baratron (pressure in the extraction line) signals for a single measurement. Each curve corresponds to the time evolution of the output signal of the sensors, in millivolts. The integrated area of the air and CO₂ peaks with respect to baseline is used to calculate CO₂ concentrations, instead of using their peak height, for greater accuracy. All information, such as the height and area of CO₂ and air which are obtained by TCD, FID and the pressure gauge measured by the Baratron gauge, is transmitted and recorded in numeric format in LabVIEW. The LabView software allows us to plot the calibration curve. Figure 4.4 shows an example. The different amount of standard gas brought in the extraction line and injected into the GC, required to obtain the calibration curve, is automatically set by inserting the information about the desired range of calibration gas pressure and of the number of injections, the EV valves being operated by this program.

4.2. Experimental procedure

The experiment is carried out in the following order: preparation of the sample and analytical line, gas extraction, gas transfer and gas analysis. For the gas analysis, a control and a sample calibration are made. The control calibration curve is made with 10 individual injections of standard gas to validate the everyday stability of the GC before measurements are made. The calibration curve is made with 30 individual injections of standard gas, in two steps: 15 points are obtained before analysing the sample and 15 points after the sample analysis.

4.2.1. Cell Preparation

The extraction chamber is prepared the day before the measurement. First, the chamber, balls and the cap are cleaned using distilled water and dried in an oven at 50 °C for 4 hours to eliminate water vapour in the cell. Then, the chamber is cooled down at room temperature for 15 min, and is sealed using a rubber O-ring with 1mm thickness (58X1 FPM 80). The chamber is evacuated for 10 min to eliminate ambient air in the cell (Figure 4.5), and then purged and filled with pure nitrogen to protect the surface of the cell from contamination by ambient air (opening and closing the nitrogen valves followed by further evacuation three times). The cell is then cooled for at least 2 hours in a freezer at -18°C.

During the night, the ethanol bath is cooled down to -70°C with two cooling systems (Figure 4.6). If the ethanol bath does not reach -70°C by the morning, it is further cooled with liquid nitrogen until it reaches -70°C. The analytical line is evacuated with 2 turbo molecular pumps over 12 hours to remove ambient air and water inside. Before measurement, the connecting part of the line is checked for leaks. V5 and V3 (Figure 4.1) are closed for 1 min. If the difference between the pressure before closing and after closing is under 2.0×10^{-3} mbar, the condition of the line is considered suitable.

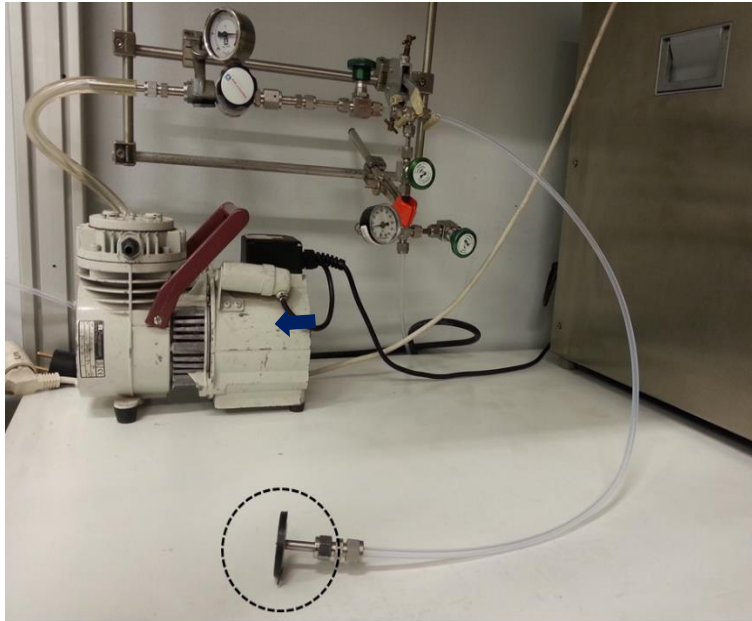


Figure 4.5. The chamber preparation line, which is used to remove ambient air in the cell and inject pure nitrogen into the cell. The dotted circle in black indicates the inlet which is connected to the chamber. The blue arrow points to the supply line which connects the pure nitrogen bottle to the chamber.

4.2.2. Sample preparation

Ice core samples are prepared in the cold room at $-18\text{ }^{\circ}\text{C}$ just before gas extraction and analysis in order to minimize the possibility of adsorption of lab air on the cleaned surface. The operator wears a pair of latex gloves over a pair of cold-temperature gloves to avoid contaminating the ice with liquid or solid components.



Figure 4.6. Two cooling systems, FT902 Immersion Cooler (left) and Huber TC100E (right)

The band saw used to cut the ice sample is first cleaned using a piece of artificial ice made with MilliQ water. For each ice sample, all the surfaces are trimmed off to remove ~ 0.5–2.0 cm. This outer layer can be altered via molecular diffusion with respect to ambient air during storage in the freezer (Bereiter et al., 2009), the latter study having shown that CO₂ concentrations increase in the layers closer to the surface of the ice core. The amount of outer layer ice to be removed is estimated considering the duration and temperature of storage (Bereiter et al., 2009).

The ice core is cut into a 40 g sample. The existence of cracks in the ice is checked, as the ice around cracks might be contaminated by drilling fluid. 2 mm of ice surface around cracks are removed if there are cracks in the sample.

Each sample is brushed to remove powdery ice from the surface. After placing the sample in the chamber, the latter is sealed with a 1 mm-indium wire and tightened with 4 nuts using a manometric wrench. The chamber is then placed into the ethanol bath (cooled to ~-70°C) to reduce water vapour in the cell.

4.2.3. Gas extraction

The chamber is then connected to the vacuum line (Figure 4.1 and 4.7). The valve of the cell is opened, and the chamber pumped for ~20 min to evacuate ambient air. While pumping the cell, another cooling system (FT902 Immersion Cooler, Figure 4.6) is operated to maintain the bath at -60/-70°C. Then leak-tightness of the chamber is checked by closing V3 and V5 for 1 min. If the pressure is stable and the pressure gauge P1 reads under 5.10^{-2} mbar, then pumping is conducted again for 10 min to further sublimate the surface of the ice sample for cleaning. If not, the sealing conditions of the cell are checked and the procedure is repeated. The valve of the cell is closed. The ethanol bath containing the chamber is moved to the freezer and the latter is mounted on the crusher. The four sealing nuts are checked with the manometric wrench and adjusted with the same force

The sample is crushed using the 100 cycle per minute vertical crusher for 90 seconds in total (two intervals of 15 seconds, and two intervals of 30 seconds). The sample is not crushed continuously for 90 sec, since some pieces of ice can move together with the balls in the chamber without the ice being crushed (Barnola, 1984). The cell is then connected to the dry gas extraction line again while keeping the cell closed, and the connection is pumped for 10 min to remove ambient air. Vacuum conditions are checked again by closing V3 and V5 for 1 min. The pressure of the chamber should reach below 1.0×10^{-2} mbar. If so, the extracted air sample is sent to the GC via a sample loop connected with a six-port two-position Valco valve, which is installed outside the GC. The extracted gas from the ice is analysed five times by closing the chamber valve after each sample gas injection. This allows to keep part of the sample gas in the chamber for further injection at lower pressure, and thus to benefit from a statistical evaluation of the reproducibility in the measurement sequence.

A six-port two-position Valco valve, which is installed outside the GC. The extracted gas from the ice is analysed five times by closing the chamber valve after each sample gas injection. This allows to keep part of the sample gas in the chamber for further injection at lower pressure, and thus to benefit from a statistical evaluation of the reproducibility in the measurement sequence.

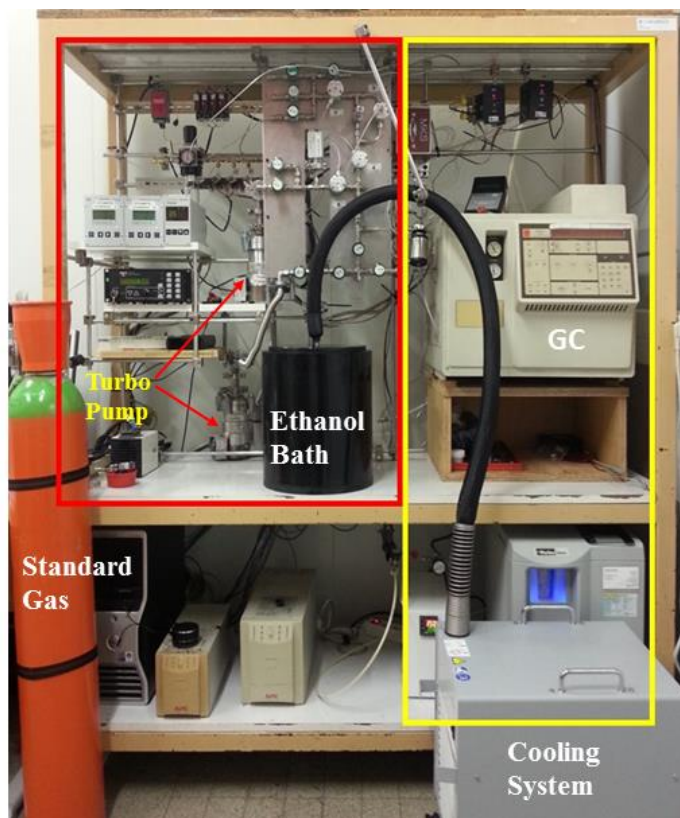


Figure 4.7. The dry gas extraction system (square in red) and Gas chromatography analysis (square in yellow).

4.2.4. Blank tests

Due to the complexity of the extraction procedure, it is important to finely control the procedure step by step and to identify all possible sources of contamination. There are three possible sources of CO₂ contamination with our analytical procedure. First, the CO₂ content obtained from the ice can be contaminated by adsorption and desorption on the surface of materials and in the gas extraction line. Secondly, the crushing process can produce artificial CO₂ because of the friction of metal parts inside the chamber. Lastly, the leak-tightness of the tip of the valve can impact on data quality, as it wears with time, leading to possible gas fractionation by diffusion. Thus, particular attention should be placed on the torque applied in order to avoid wearing of the valve.

In order to quantify CO₂ contamination due to the measurement process, numerous blank tests were conducted, in a much more systematic manner than before. A blank test consists of conducting measurements using artificial bubble-free ice and a standard gas with a known concentration of CO₂ by following the same analytical procedure as with a natural ice sample. CO₂ contamination is therefore estimated from the observed difference between the concentration of the standard gas and the one measured during the blank test (Figure 4.8). After inserting the bubble-free ice into the cell, the cell is vacuumed down to 1.0×10^{-3} mbar for 30 min while cooled at -70°C on the ethanol bath. Afterwards, standard gas (233.7 ± 0.4 ppmv of CO₂ in air, certified by Air Liquide) is injected in the cell. The gas is then left equilibrating in the cell for 10 minutes. Then the gas is analysed twice by successive injections into the extraction line and sample loop. These two measurements allow us to validate the baseline of the system. Afterwards, the bubble-free ice is crushed and the gas is analysed 5 more times.

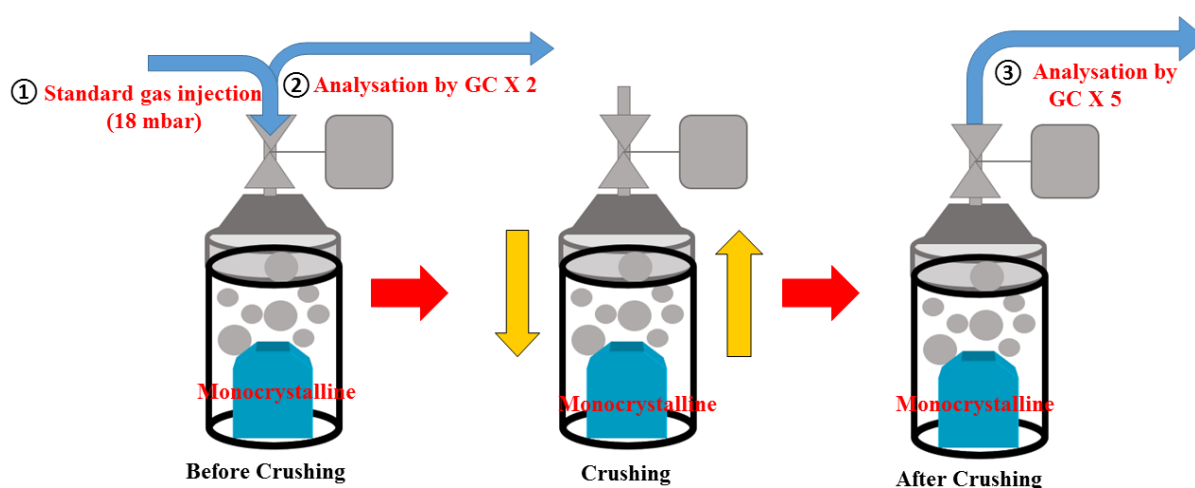


Figure 4.8. An illustration showing how to conduct the blank test.

Each chamber shows different contamination levels. Therefore, blank tests are conducted on each chamber every 10 measurements of natural ice. The difference between the results before and after crushing is used to correct the dataset comprising 10 samples. This correction will be introduced in the following section.

4.2.5. Analysis of atmospheric CO₂ concentration

4.2.5.1. Calibration

The CO₂ concentration of natural ice samples is determined by using repeated injections of a calibration gas of known CO₂ concentration, injected in the GC at different pressure (and thus with different amount of CO₂ molecules). To do so, a calibration curve, also known as a standard curve, is used. For every analysis, the GC system is calibrated again using the same dry standard air.

First, the calibration curve using standard air samples is established by a first order linear equation linking the area of the CO₂ peak to the area of the air peak:

In this thesis, the CO₂ concentration of the standard air tank used for the calibration procedure is 233.7±0.4 ppmv. This concentration is calibrated by two standard air CSIRO1677 with 260.26±0.2 ppmv and CB09707 having 238.34±0.04 ppmv in June, 2016. CSIRO1677 and CB09707 are certified by Commonwealth Scientific and Industrial Research Organisation and National Oceanic and Atmospheric Administration respectively. The air pressure of each calibration curve ranged between 3 and 17 mbar. The linear function is as follows.

$$SCO_{2,standard} = a * Sair_{,standard} + b \quad (4.1)$$

where $SCO_{2,standard}$ is the area of the CO₂ peak obtained with the standard gas and $Sair_{,standard}$ is the area of the air peak. a and b are the coefficients of the first order linear equation.

4.2.5.2. CO₂ calculation

The CO₂ concentration $[CO_2]_{sample}$ of the extracted air from the ice is calculated using the linear relationship between the ratio of surface area to air pressure and the CO₂ mixing ratio, as follows:

$$\frac{[CO_2]_{sample}}{[CO_2]_{standard}} = \frac{SCO_{2,sample} - b}{SCO_{2,standard} - b} \quad (4.2)$$

$$\frac{[CO_2]_{sample}}{[CO_2]_{standard}} = \frac{SCO_{2,sample} - b}{a * Sair_{,standard}} \quad (4.3)$$

$$[CO_2]_{sample} = \frac{[CO_2]_{standard} * (SCO_{2,sample} - b)}{a * Sair_{,standard}} \quad (4.4)$$

4.2.5.3. Water vapour percentage calculation

The water vapour percentage of the 5 injections from a sample is systematically determined to verify the data quality. Powdery ice produced by crushing can move from time to time into the extraction line and into the GC when the valve of the chamber opens, due to the pressure gradient between the chamber and the extraction line. In addition, the water vapour amount can vary depending on the temperature of the ethanol bath.

Table 4.2. An example of how to calculate the water vapor percentage

$$P = a * S_{\text{air}} + b \qquad a = 0.042452 \qquad b = -0.122807$$

P_{measured}	S_{air}	$P_{\text{estimated}}$	$P_{\text{measured}} - P_{\text{estimated}}$	%
13.6	323	13.59	0.01	0.1%
10.7	254	10.66	0.04	0.4%
8.7	205	8.58	0.12	1.4%
6.9	163	6.80	0.10	1.5%
5.6	132	5.48	0.12	2.1%

The total pressure measured by the Baratron gauge during expansion of the sample gas into the extraction line includes the pressure of the dry gas extracted from the ice and the water vapour pressure produced by sublimation of the powdery ice ($P_{\text{air}} + P_{\text{water}} = P_{\text{total}}$). The water vapour percentage is calculated as follows.

$$\text{Water vapour percentage} = \frac{P_{\text{measured}} - P_{\text{estimated}}}{P_{\text{measured}}} \qquad (4.5)$$

where P_{measured} is the value measured with the Baratron gauge, P_3 . $P_{\text{estimated}}$ is obtained by the linear relationship between the total pressure and the surface of the air peak (being dry air) from the calibration curve ($P_{\text{air}} = a * S_{\text{air}} + b$). In the absence of water vapour, the value of P_{measured} and $P_{\text{estimated}}$ are equivalent. Thus the difference between P_{measured} and $P_{\text{estimated}}$ gives information about the percentage of water vapour. Table 4.2 shows an example of how the water vapour is calculated throughout the five consecutive injections. Constants a and b are obtained by the linear relationship between S_{air} and P_{air} .

4.2.5.4. Data correction

Measured CO_2 should be corrected for contamination caused by the analytical procedure (Chapter 4.2.4) by comparing measured CO_2 in blank tests with the standard gas value. However, it is not feasible to correct CO_2 concentrations directly. The CO_2 mixing ratio is calculated as the ratio between partial pressure of CO_2 and total pressure in the measurement line, which is a relative value. Thus, CO_2 concentration, and the concentration of CO_2 contamination, are dependent on the total pressure. To avoid this dependence, we correct the absolute value (partial pressure) of CO_2 in the air by the expected partial pressure of CO_2 contamination, as estimated from blank tests.

Table 4.3. This table show how to calculate partial pressure of CO₂ contamination. This blank test was conducted on 30.08. 2017. For this measurement, standard gas with 233.7±0.4 ppmv of atmospheric CO₂ is used.

Blank test before crushing	233.5 ppmv	Del ($[\text{CO}_2]_{\text{standard}} - [\text{CO}_2]_{\text{Blank test before crushing}}$)	0.2 ppmv
----------------------------	------------	---	----------

N	P _{total}	[CO ₂] _{measured}	$([\text{CO}_2]_{\text{measured}} - [\text{Del}]) - [\text{CO}_2]_{\text{standard}}$	P _{CO₂ contaminated}
	[mbar]	[ppmv]	[ppmv]	[mbar]
1	8.7	234.2	0.6	0.0056
2	7.0	235.2	1.7	0.0116
3	5.7	234.9	1.4	0.0080
4	4.5	234.3	0.8	0.0037
5	3.7	234.6	1.1	0.0041
Average	5.9	234.6	1.1	0.0066

Table 4.3 shows how the average partial pressure of CO₂ contamination is calculated with the blank test results. The top row shows the blank test result when standard gas is analysed, without adding crushed ice to the measurement system. Thus, this value can be used to calculate the baseline of the system. The CO₂ difference (Del) between the blank test before crushing and the standard gas value is only 0.2 ppmv. For the test described in rows 1-5, artificial ice was crushed in the sample chamber containing the standard gas, before injecting the gas into the GC. These blank tests were used, as indicated in the table, to determine the average partial pressure of CO₂ contamination.

To correct the data, the average partial pressure of CO₂ contamination is removed from the total pressure of sample, as follows:

$$[\text{CO}_2]_{\text{corrected}} = \frac{\overline{P}_{\text{total}} * [\text{CO}_2]_{\text{sample}} - \overline{P}_{\text{CO}_2(\text{Con})}}{\overline{P}_{\text{total}}} \quad (4.6)$$

P_{total} represents the average of total pressure measured in the sample loop before analysing gas by the GC. P_{CO₂(con)} is the average partial pressure of atmospheric CO₂ calculated by the blank test (Table 4.3). P_{total}*[CO₂]_{sample} indicates the partial pressure of CO₂ mixing ratio of a sample.

4.3. Improvements with respect to the existing setup

During the first 10 months of this PhD, numerous blank tests were conducted to understand the system and to determine possible causes of variability. Three problems were found: First, the previous published data were uncorrected for contamination, assuming that it was negligible. Secondly, we

observed that varying amounts of powdery ice produced by crushing could sublime into the extraction line, leading to lower precision. Last, only 2 samples could be measured in a day. Low sample throughput made it difficult to improve the temporal resolution within reasonable time limits. These three problems were solved or improved during this thesis. For the data correction, blank tests were conducted to understand the amount of artificial CO₂ added by crushing and the analytical process. The new data correction was developed to obtain an absolute CO₂ value. The blank tests and the new data correction are already discussed in Chapter 2.2. Thus, here the improvements to the precision and sample throughput are discussed here.

4.3.1. Reduction of water vapour inputs

From one sample gas injection to another, the amount of water vapour produced through sublimation of ice powder into the extraction line can vary, depending if ice particles are able or not to move from the chamber into the extraction line. Table 4.4 shows a typical example of such variability.

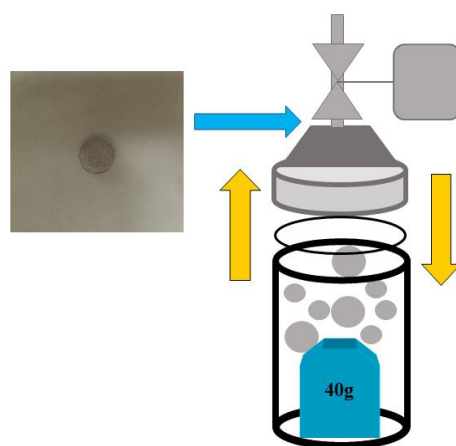


Figure 4.9. This figure shows a screen (a diameter of 1/4" and pore size of 10 micron) inserted in the cell.

Water vapour is unusually high for the second and fifth measurements. The temperature of the ethanol bath being maintained at around $-70\sim -60^{\circ}\text{C}$, the water vapour content in the cell should be very low (0.010817 mbar at -60°C). The second and fifth measurements also show atmospheric CO₂ concentrations lower than the standard gas concentration. One possible explanation lies in the “carrier gas” effect of water vapour between the chamber and the extraction line. When the chamber valve is opened and a large amount of water vapour is produced by sublimation of powdery ice, part of the water vapour diffuses back into the chamber due to its low temperature (thus acting as a cold trap). During the retro-diffusion of water vapour, CO₂ could be preferentially carried back into the chamber, leading to a lower concentration measured in the injected gas.

In our updated protocol, a filter was installed between the cell cover and its valve to prevent the movement of powdery ice from the cell (Figure 4.9). A screen with a diameter of 1/4" and pore size of 10 microns was used. After inserting a filter in the line, high water vapour percentages were no longer observed and the precision of the data largely improved. Figure 4.10 shows the improvement of the precision. Blue dots indicate 6 analyses from a sample of the Vostok ice core on 30th March 2016. This was conducted without a filter. The orange dots and grey dots are CO₂ data from the EPICA / Dome C (EDC) ice core while the filter was installed, measured on 13th Sep in 2017 and 11th August 2017 respectively.

Table 4.4. An example of data from a blank test performed on cell 1 on 14th April 2015. CO₂ concentration of standard gas is 237 ± 4.7 ppmv and the average. CO₂ concentration of the six measurements is 234.7 ± 11.5 ppmv (1σ)

N ^o measurement	Total pressure	[CO ₂] _{measurement}	[CO ₂] _{measurement} -[CO ₂] _{standard}	Water vapour
	mbar	ppmv	ppmv	%
1st	13.3	238.6	1.6	4.1
2 nd	10.5	233.2	-3.8	7.6
3 rd	8.5	241.1	4.1	3
4 th	6.8	242.3	5.3	3.3
5 th	5.5	210.1	-26.9	57.6

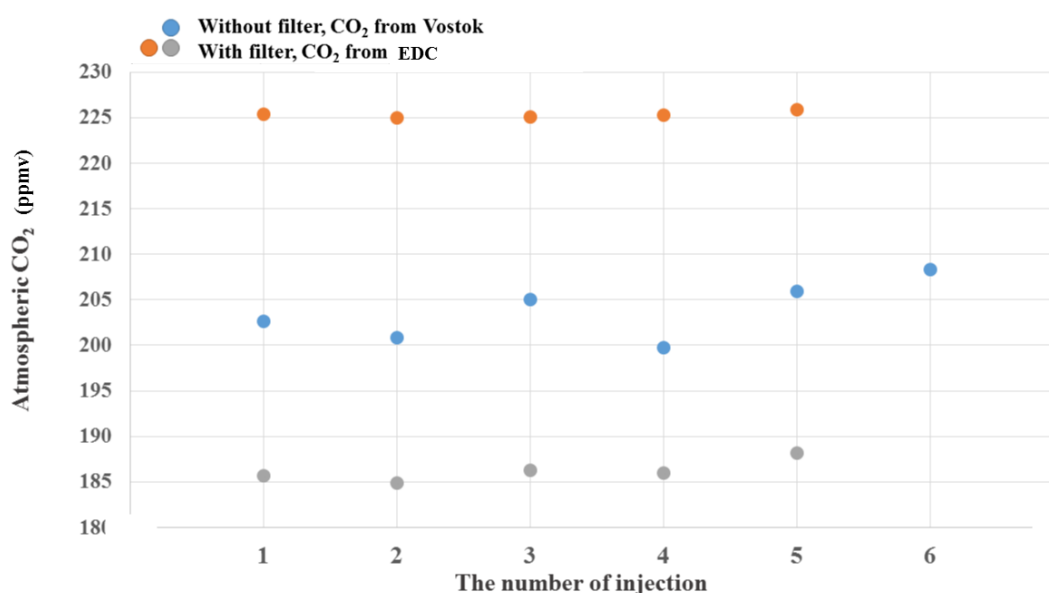


Figure 4.10. This graph shows the improvement of the data precision after inserting a filter in a cell. Grey dots: CO₂ concentration from EDC measured on 11th August 2017. Concentration is 186.2 ± 1.1 ppmv. Blue dots: CO₂ concentration from Vostok measured on 30th March 2016. Concentration 202.8 ± 2.7 ppmv. Orange dots: CO₂ concentration from EDC measured on 13th September 2017. Concentration is 225.3 ± 0.3 ppmv. All data were measured from the clathrate ice.

The five injections of the Vostok gas samples provide a precision of 2.7 ppmv. On the other hand, the EDC data show a precision of 0.3 and 1.1 ppmv respectively, considerably improved compared to the Vostok example. Following this technical improvement, the average error bar on the dataset obtained over the MIS 6 period is ~1 ppmv, i.e. among the best of all ice core CO₂ measurement systems.

4.3.2. Improvement of sample throughput

Cooling down the ethanol bath between -60 and -70°C is a time consuming process when using a single cooler. In order to improve the sample throughput per day, we introduced a second cooler, FT902 (Figure 4.6). This allowed us to obtain the desired temperature in a much faster manner. We could then measure 4 samples maximum within 9 hours. However 3 samples a day were usually measured, in order to allow for 1 hour of vacuuming to remove water vapour in the line after each measurement.

4.4. Conclusion

Through a careful and regular evaluation of blanks of the analytical system and through reducing the amount of water vapour introduced in the extraction line, I could significantly improve the CO₂ analytical system of IGE. The ball mill extraction system now reaches a reproducibility of about 1 ppmv (1 σ). This precision is one of the best performances for CO₂ measurement in ice cores. However only 3-4 samples can be measured per day, which is still a limiting factor of this method when compared with, e.g., the analytical system developed at the University of Bern. Considering that improving temporal resolution of CO₂ data is the main target in the CO₂ field, additional improvements on sample throughput are needed.

Chapter 5

A new high efficiency dry extraction technique for the measurement of atmospheric CO₂ in Antarctic ice cores

In Chapter 4, I discussed our upgraded ball mill method showing a measurement reproducibility of about 1 ppmv (1σ) when coupled with the Gas chromatography (GC) analysis. This represents, up to today, one of the best performances for CO₂ measurement in ice cores. Even though the analytical system provides 1 ppmv of precision, the accuracy is affected by other parameters, such as ice core quality and handling during the sample preparation. To improve the accuracy of the measurement, replicates from the same depth interval are essential. However, the large sample size is required for the ball mill system (~40 g) and the limited ice samples are available. In addition, it has been observed that the ball mill technique does not provide a homogeneous and fine crushing, with consequently low extraction efficiency.

As discussed in Chapter 3.2, dry gas extraction has a different extraction efficiency depending on the presence of bubbles and/or clathrates in the ice sample. This phenomenon leads to biased CO₂ concentration when the gas is extracted from BCTZ. For instance, the ball mill method is not suitable to fill the gap during the 35-20 kyr BP interval in the EPICA Dome C, EDML, and TALDICE ice cores which include BCTZ ice (Neff, 2014; Parrenin et al., 2012; Schilt et al., 2010). Therefore, maximizing the possible extraction efficiency of the extraction system and minimizing the different extraction efficiency between bubbles and/or clathrate ice would provide a better accuracy on the reconstruction of atmospheric CO₂ variations in BCTZ.

To reach these goals, we develop a new dry extraction method called the ring mill system which not only would aim for a better extraction efficiency but also would require a smaller ice core sample. In Chapter 5.1 the new chamber and the crushing system are described, and in Chapter 5.2 the distribution curves of the powdery ice produced by ring and ball mills are compared in order to explain the improvement of the extraction efficiency. Its precision and accuracy using artificial ice and its application to clathrate of EDC samples are reported to discuss the performance of this new system. Because of the limited number of data obtained in this thesis, we could not fully characterize the system, and further investigations will be required. Future plans are also discussed in Chapter 5.3, followed by conclusions (section 5.4).

5.1. The Ring mill system

The ring mill technique consists of a planetary grinding system and a ring chamber (Figure 5.1). The principal difference with respect to the ball mill is that the ice core sample placed in a chamber is crushed by rotating the chamber horizontally. This ring mill system is usually applied for the fine grinding of solid materials such as quartz or mud, seeds or ores. This is the first time that a ring mill method was applied in ice-core sciences.

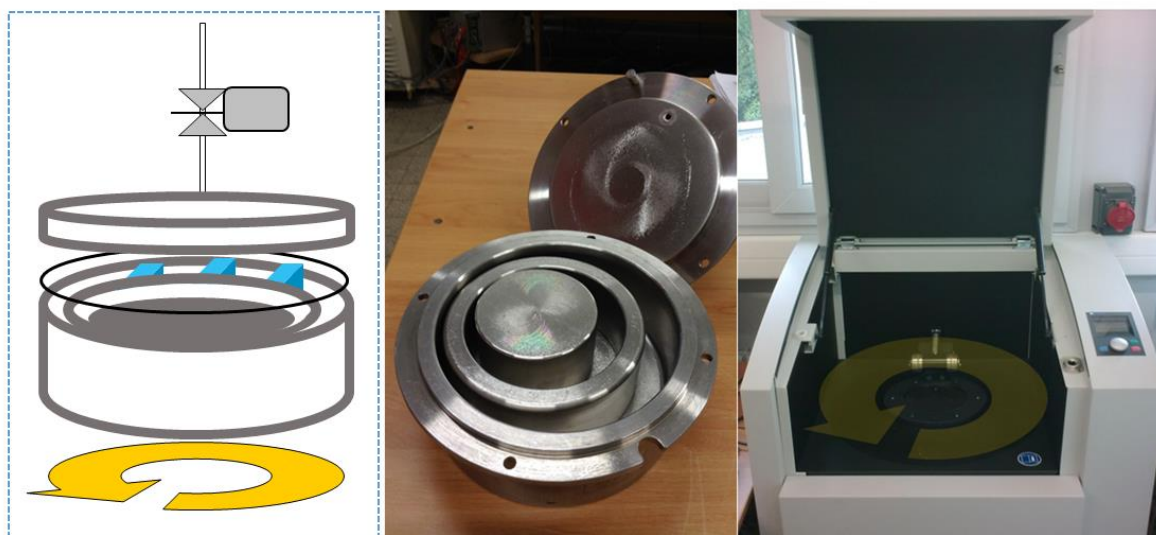


Figure 5.1. On the left-hand side a schematic of the ring chamber showing how the sample (in blue) is located in the chamber, and how the chamber is sealed with a 1.5 mm thickness indium wire (in black). At the centre, a picture of the ring chamber. On the right-hand side the planetary grinding system. Yellow arrows indicate the direction of the rotation.

The free volume of the ring mill is $\sim 390 \text{ cm}^3$. In a chamber (height: 6 cm, external diameter: 15 cm), a hollow cylinder (diameter: 10.5 cm) and a circular cylinder (diameter: 7.4 cm) are placed. All the parts are made of stainless steel. A 20–40 g sample of ice is cut into three pieces with a thickness of 1.5 cm. The ice pieces are then placed in between the two cylinders (Figure 5.1). The chamber is sealed with a 1.5 mm thickness indium wire. This chamber is tightened with four screws, which are tuned by a manometric key in order to apply consistently the same strength. Three different chambers have been manufactured so far, and each chamber is numbered in the chronological order of manufacturing.

A Retsch RS200 planetary mill, a powerful and quick grinding system, is used to crush samples into fine powders, under $1 \mu\text{m}$. The planetary mill rotates the chamber on an orbit around its centre. The cylinders inside the chamber are rotated by the grinding system to crush the sample. With a speed of 700 rpm (rotations per minute), only 5 sec are required to crush a sample.

The procedure of extraction and analysis are similar to the ball mill measurement. There is only one difference between the two techniques: the planetary mill crusher is not installed in a walk-in freezer, therefore the ice core samples are crushed at 20 °C. However, since the crushing is fast, the chamber, cooled to -70 °C in an ethanol bath, is exposed to room temperature only for ~1 minute, which is not long enough to cause any eventual melting of the sample.

5.2. Distribution of grain size of the ice powder

The maximum extraction efficiency on clathrate ice can be obtained by releasing air from all the clathrates present in the sample. Considering that the diameter of clathrate ice crystals in Antarctic ice cores is between 0.02-0.20 mm (Uchida et al., 2011), the size of all powdery ice produced by crushing should be smaller than 0.20 mm to reach the maximum extraction efficiency. Therefore, in order to understand the improvement of the extraction efficiency on clathrate ice, the size of the powdery ice produced by ring and ball mill methods was measured with gas-free single-crystal ice and the Vostok ice core samples and compared.

The grain size of ice powder produced by crushing a sample was measured by a sieve tower (Fritsch and Retsch) which consists of six different sizes of woven wire screens (above 2 mm, 1–2 mm, 0.5–1 mm, 0.25-0.5 mm, 0.1–0.25 mm and below 0.1 mm). The distributions were measured as follows: after crushing the sample, the residual ethanol present on the external surface of the crushing chamber was removed by flushing compressed air, for a clean manipulation of the sample. With tissue, the ethanol cannot be removed sufficiently, thus, residual ethanol can flow into the chamber when it is opened. Afterward, the chamber was moved into a walk-in freezer at -18°C. The powdery ice was placed in a sieve tower and shaken by hand to separate grains for ~1 min. Then, the ice powder collected on the six screens were measured by a precision weight balance (METTLER PM 400) with a precision of 0.004 g. However, because of turbulences produced by the air flow in the freezer, the precision was degraded to ± 0.35 g during the measurements, which represents 1.75 and 3.5 % for 20 and 40 g samples, respectively.

Figure 5.2 shows the grain size distribution of the ball systems. The grain size distribution of the ball system with 40 g samples and the ring system with 40 and 20 g samples were compared. The measurements on the ring system were conducted using Vostok ice core samples in May 2016, while the ones with ball mill system were conducted using gas-free single-crystal ice in Dec 2018.

In the grain size distribution of the ball mill system in figure 5.2, the powdery ice of diameter greater than 2 mm is the largest portion, about 43.3 %. However, for the ring system, only 2.8 % and 1.8 % of sample grain sizes are greater than 2 mm for 40 and 20 g samples, respectively. This result shows that the ring mill can crush samples into finer grains for both 20 and 40 g sample sizes. Large

pieces of ice (visible by ice) were not observed with the ring mill, and the crushed ice was well homogeneous.

To understand the extraction efficiency on the clathrate ice, we should now focus on the grain sizes below 0.25 mm. For the ball mill system, ~12.4 % of the grain size distribution falls below 0.25 mm against, ~36 (45) % for the ring mill system with 40 (20) g sample. The distribution of grain size for ring system shows that ~64 (55) % of grains from a sample of 40 (20) g are larger than 0.25 mm. This indicates that the extraction efficiency of the ring system is better than that of the ball system, but still limited on clathrate ice. The trapped air in clathrate ice is not extracted 100 % by the ring mill system. Moreover, a similar distribution of grain size is found whether the 40 or 20 g samples are pulverised by the ring mill system.

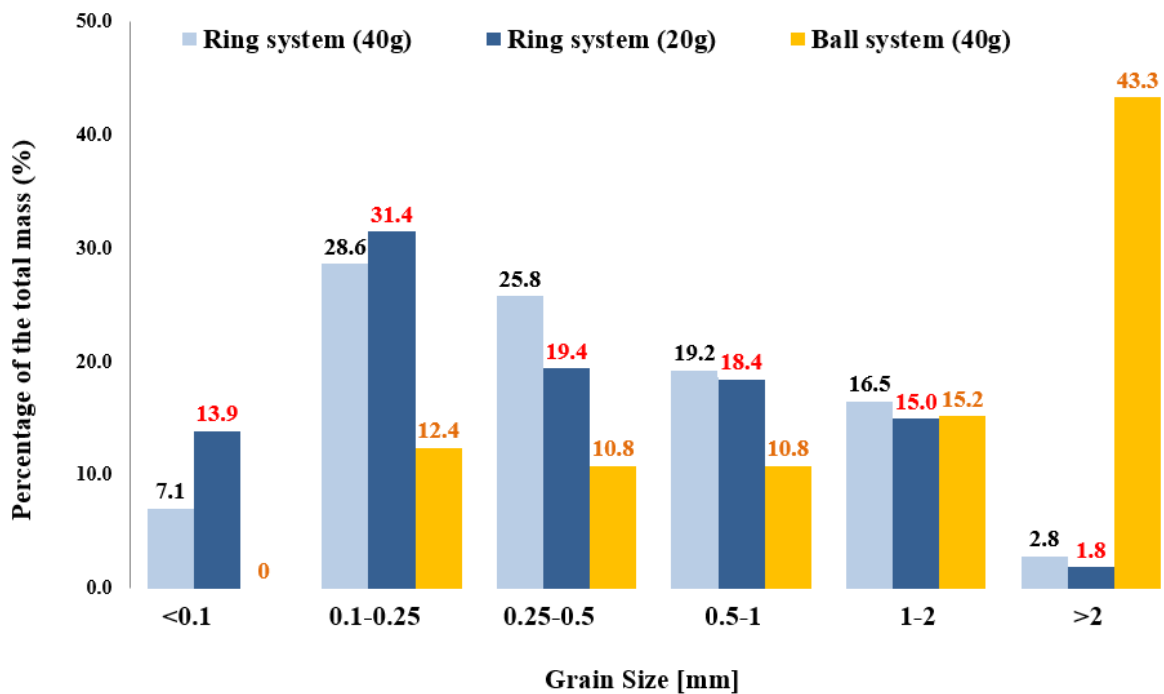


Figure 5.2. The grain size of the powdery ice produced by the ball mill (yellow) and ring mill systems (blue and sky blue) at IGE. Each value indicates the percentage of each of the six size categories (above 2 mm, 1–2 mm, 0.5–1 mm, 0.25–0.5 mm, 0.1–0.25 mm and below 0.1 mm).

The previous studies reported that the ball mill system has ~62 and ~52 % air extraction efficiency on bubbly and clathrate ice (Schaefer et al., 2011). However the grain size distribution of the ball system shows that ~87.6 % of grains are larger than 0.25 mm.

Our result is also compared with published data by Bereiter et al. (2013) measured at the University of Bern (UBern) by a centrifugal ice microtome (CIM) and needle cracker with an extraction

efficiency of 90 %–95 % (9.5 g) and 50 %–70 % (16 g), respectively (Bereiter, 2012). Figure 3 shows the distribution of the powdery ice produced by the ring and the ball mill at IGE and the needle cracker and the CIM at UBern.

The grain size distributions from the newly developed CIM and ring mill systems, both show a finer grinding than the ball mill and needle cracker. The most substantial portion of the grains from the needle cracker and ball mill are larger than 2 mm. In contrast, the percentages of grains over 2 mm from the CIM and ring mill systems are negligible. The ring mill and CIM are capable of crushing ice samples into fine structures, whereas the needle cracker and ball mill systems have large amounts of residual powder greater than 2 mm in diameter.

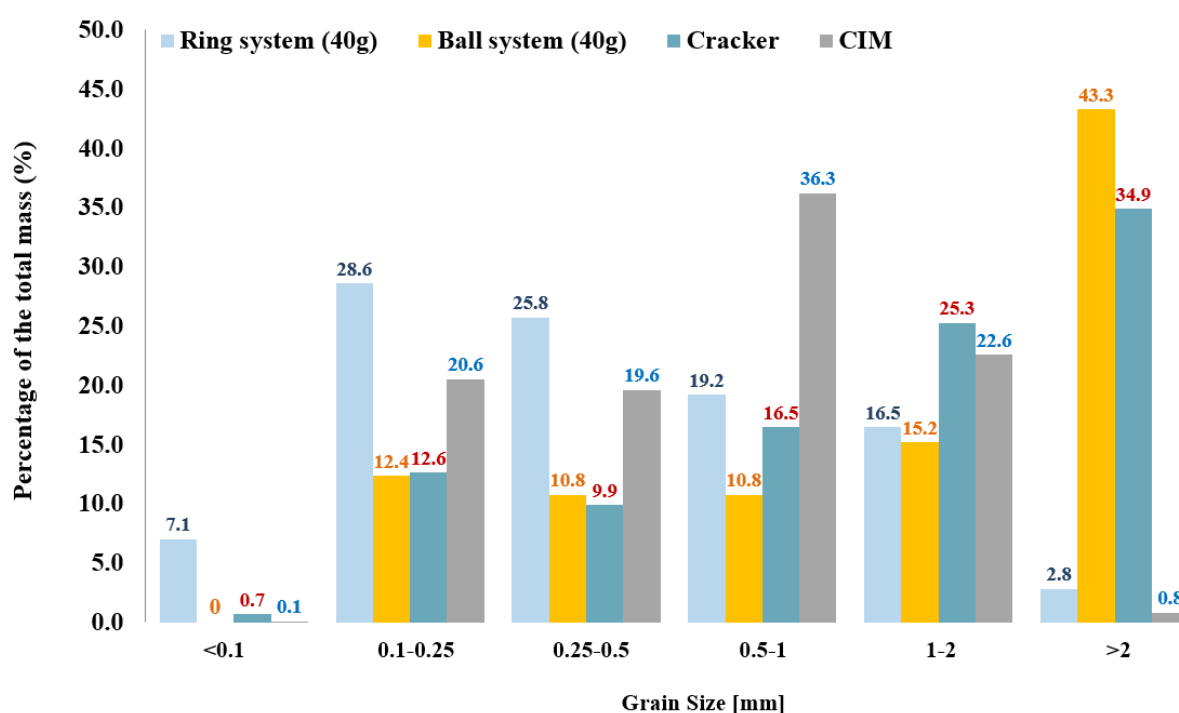


Figure 5.3. The grain size of the powdery ice produced by ring mill system (sky blue) and ball mill (yellow) in our laboratory is compared with that by cracker (turquoise blue) and CIM (grey) at UBern. Each value indicates the percentage for each size category. In the data measured by CIM in figure 3, a fixed knife of CIM is positioned in the microtome for producing coarser powders.

The distribution of the ring mill is shifted to lower sizes with respect to the CIM distribution. The largest portion of ice mass for the ring mill falls to grain sizes between 0.1–0.25 mm, while for CIM the largest portion is at 0.5–1 mm. Grain sizes below 0.25 mm make up only 20.7 % of the CIM distribution, compared to 35.7 % for the ring system. Thus we can conclude that the ring mill provides the finest grain size distribution and therefore the best extraction efficiency with respect to the existing dry extraction methods.

5.3. Results and discussion

5.3.1. Results from blank tests

For understanding the accuracy of the new system, blank tests were conducted with 40 g artificial monocrystalline ice and standard gas mixture (containing 233.7 ± 0.4 ppmv of CO_2 in dry air) over two years (2016/17) with the three different ring chambers. Blank tests were conducted using similar gas pressure than for Antarctic ice cores (first expansion of ~ 6.6 mbar on average).

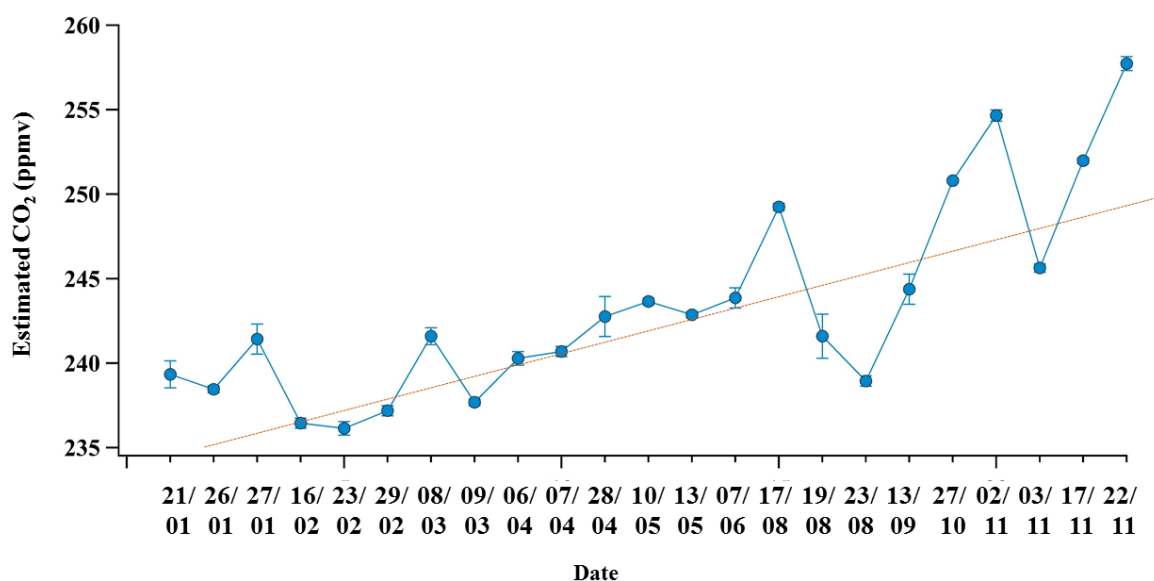


Figure 5.4. The blank test in 2016 conducted by ring system #2. The x-axis shows the date of the measurement. The dotted red line indicates the trend line.

For the blank tests (as for all the GC measurements conducted at IGE) the surface of the gas chromatography peak of CO_2 does not depend only on the CO_2 concentration but also on the total pressure of gas injected into the chamber. However, when the standard gas is injected into the chamber, the pressure cannot be adjusted precisely. Thus, CO_2 concentrations of the blank tests were estimated using the partial pressure of CO_2 contamination assuming that ~ 7 mbar of standard gas (STD: 233.7 ± 0.4 ppmv) is injected into the GC. Blank tests were conducted on each chamber, because even if the gas is analysed by the same GC, using the same sampling line, and following the same crushing procedure, effects of absorption/desorption of atmospheric CO_2 and CO_2 degassing will vary from chamber to chamber.

Figure 5.4 shows CO_2 concentrations of the blank tests conducted using ring mill #2 over one year in 2016. In total, 23 blank tests measurements were conducted. The average precision of each

measurement, shown as error bars in the figure, is 0.5 ppmv, which is comparable with the precision obtained with the ball mill technique for the same sample size. This result confirms that the ring crushing followed by five injections into the GC can lead to good precision. However, figure 5.4 shows the degradation of the crushing cell over time, which would compromise the accuracy of the measurements. The latter, from January 21st to June 7th 2016 (expressed as the standard deviation of the 14 blank tests) was ~ 2.6 ppmv (1σ) with an averaged concentration of 241.4 ppmv (7.7 ppmv higher than the expected concentration of the standard gas mixture). However, after CO₂ reached the highest concentration on 17th August, the measurements showed a larger scattering, with a continuous and rapid increase of CO₂ concentration since then. Here, the average value was 244.5 ppmv above the expected concentration and an accuracy of 5.5 ppmv was observed. The measurement degradation after June 7th is related to the increase of scratches on the internal surface of the chamber and its cap, which were created by the rotation of the rings in the chamber. By conducting the blank tests regularly, the time frame of when the accuracy degrades and the contamination increases can be identified.

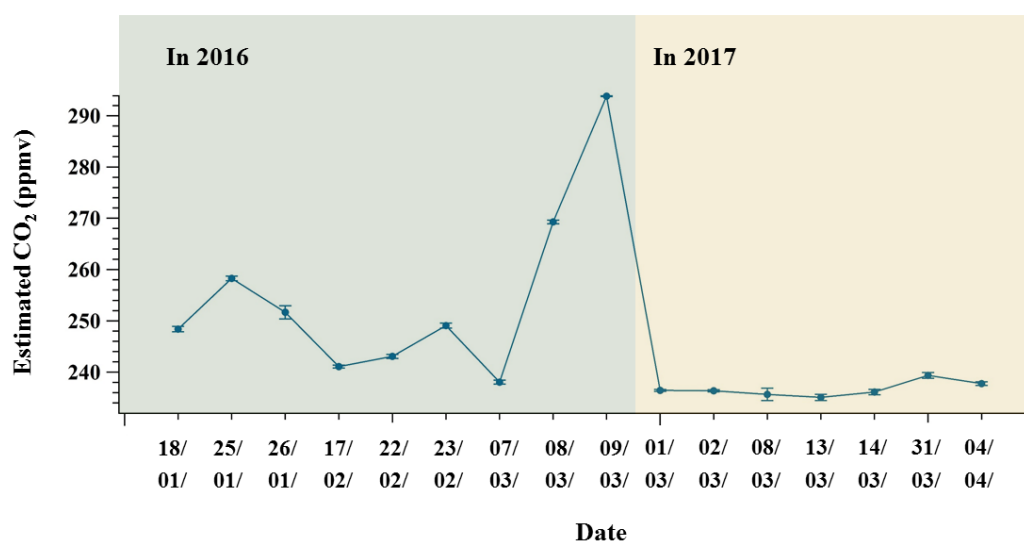


Figure 5.5. The blank test results by ring mill #1 in 2016 and 2017. Data in the green area were measured in 2016, and report an increase of CO₂ contamination in March 2016. Data in the yellow area were collected in 2017 after polishing the internal surfaces of the ring mill.

Moreover, the long-term precision can vary depending on the measurement period (Figure 5.4), indicating some remaining instability in the system. The long-term precision during 8th March-7th June, for example (standard deviation between the 6 blank test measurements), was 1.5 ppmv, which represents the best precision achieved in 2016. On the other hand, during the period from October 27th to November 22nd, the precision degraded to ~ 4.5 ppmv (5 blank tests). According to the three data points on November 3rd, 17th and 22nd, CO₂ concentration continuously increased by 10.6 ppmv (from

247.4 to 258.0 ppmv) in less than 20 days. If samples were measured over this period, we could only measure them with an accuracy not better than 10 ppmv. This phenomenon might be related with the condition of the GC and sample line. However, according to the blank tests conducted six times with ball #5 during 17 Aug–2 Nov, the standard deviation of the data set is 1.3 ppmv, which shows that the whole system was stable during this period. We can therefore conclude that the condition of GC and the sample line do not have an impact on this result, and that the degradation of the measurement is directly related to the condition of the ring mill.

Because of the reasons mentioned above, we conduct the blank tests every five measurements for monitoring the state of the system. Because the initial number of blank tests performed was limited, the frequency of testing could be adjusted after additional measurements. In addition, when the initial blank tests were conducted, the chamber had already been used. Thus, we do not know exactly when the scratches on the chamber surface started to produce larger artificial CO₂ contamination. Additional measurements are needed to understand on this, using a new or polished chamber.

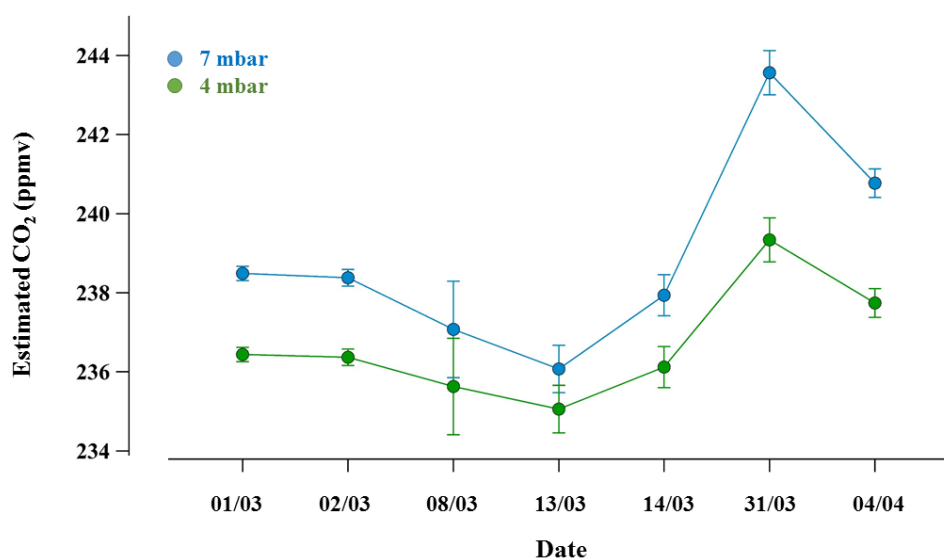


Figure 5.6. Blank test results with Ring #1. From these seven data points recorded at slightly different pressures, we estimated concentrations at 7 mbar (green line) and 4 mbar (blue line).

Figure 5.6 shows CO₂ concentrations which were estimated with the partial pressure of CO₂ contamination of the blank tests using ring #1 in 2017. We make two series of tests, one at higher pressure, 7 mbar (corresponding to ~40 g of ice) and one at lower pressure, 4 mbar (corresponding to ~20 g of ice).

The blue and green lines in Figure 5.6 show raw CO₂ estimates, from a real dataset recorded at variable pressure, for 7 and 4 mbar of standard gas injected into the cell. The standard deviation of the

7 and 4 mbar experiments are 1.4 and 2.5 ppmv, respectively. The pressure of CO₂ produced by the crushing should be constant and that therefore the high pressure measurement will be less affected by contaminations.

In conclusion, the extraction efficiency of the ring mill system using both 20 and 40 g samples is higher than that of the ball mill system using a 40 g sample. However, the ring system measurement precision (~2.6 ppmv, 1 σ) is worse than that of the ball mill system (1 ppmv). To measure CO₂ concentrations precisely with the ring system, conducting a blank test after at least every 5 measurements is essential, and a 40 g sample should be used.

5.3.2. Results from Antarctic ice cores

To examine the accuracy of the new system on clathrate ice and BCTZ ice, we measured CO₂ concentrations in both clathrate and BCTZ ice from three different ice cores: EDC, TALDICE and Vostok. Atmospheric CO₂ at 53.2 kyr BP and 148.4 kyr BP were reconstructed from BCTZ and clathrate ice, respectively, from the Vostok ice core. Four depth intervals of TALDICE ice were also taken, which consist of BCTZ and clathrate ice. However, due to the lower quality of the Vostok ice core and the limited number of samples of TALDICE, we could not verify our system, and additional measurements with the TALDICE ice core to test the system will be required. These measurements are not introduced here. Atmospheric CO₂ during the MIS 6 period shows an offset between ring and ball mill systems, which might be related with different analytical methods. This offset will be discussed here.

Atmospheric CO₂ in EDC during the MIS 6 period (190–135 kyr BP) was reconstructed by ring mill (11 data points) and ball mill (150 data points) (Figure 5.7). Samples of 25 g and 40 g were used for the ring and ball mills, respectively. Figure 5.7 shows CO₂ concentrations in EDC ice core measured with both extraction systems. Unfortunately, because of the limited amount of samples available, the data could not be reconstructed by both methods at the same depth interval. Thus, in order to calculate the CO₂ offset caused by the systems, CO₂ concentrations by ball mill system at the same depth as the ring system data were reconstructed by linear interpolation. The data were corrected for the contamination effect in the same way. The average CO₂ offset between the two datasets was found to be 8.9 ± 5.9 ppmv. CO₂ concentrations measured by the ring system are systematically higher than CO₂ concentrations measured by the ball mill system except for one data point at ~170.8 kyr BP. This difference might be related with the lower extraction efficiency of the ball with respect to the ring system on the clathrate ice. The EDC ice core was drilled in 1999 and, during the storage, more than 50% of the initial hydrates present in the fresh ice may have been decomposed and transformed into secondary bubbles, or gas cavities (Lipenkov, *Pers. Comm.*). This possible hydrate decomposition should reduce the discrepancy of the measurements between the two extraction methods, which is not evident from the measurements.

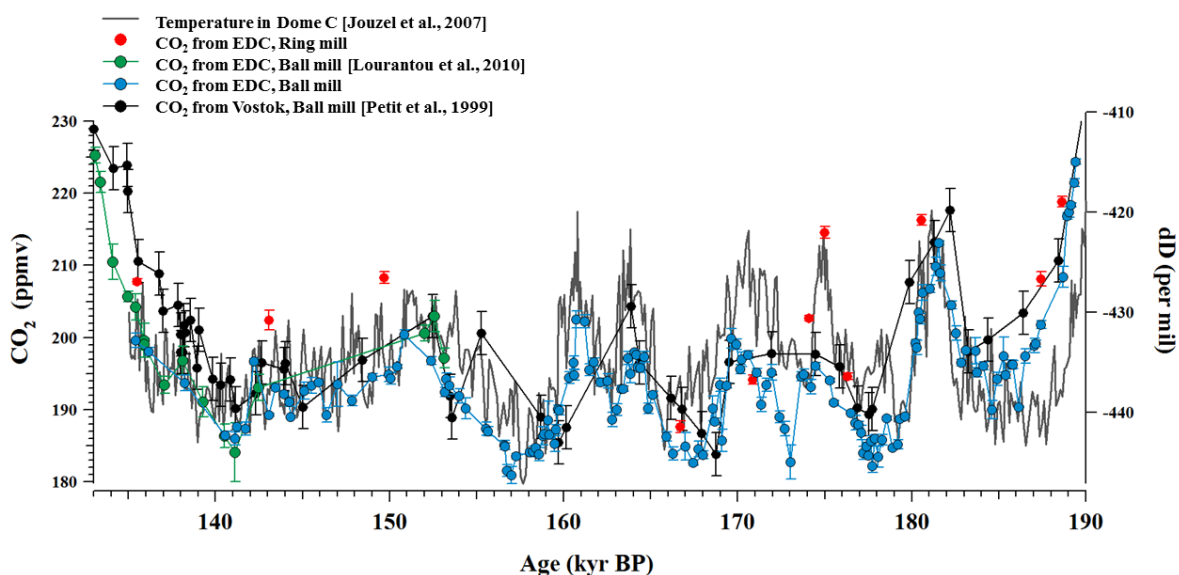


Figure 5.7. Atmospheric CO₂ in EDC and Vostok ice cores during MIS 6 period (190-135 kyr BP) with temperature variabilities in EDC (Jouzel et al., 2007; Lourantou et al., 2010a; Petit et al., 1999). All atmospheric CO₂ data set were measured at IGE. Blue dots and red dots indicate atmospheric CO₂ in EDC measured by the ball mill system and the ring mill system respectively (in this thesis). Green dots show data from EDC reconstructed by the ball mill system (Lourantou et al., 2010a). Black dots show atmospheric CO₂ in the Vostok ice core measured by the ball mill system (Petit et al., 1999). The precision of the ring mill during these measurements was ~ 2 ppm on Ring #1, 2 and 3.

5.4. Conclusion

The ring system for CO₂ measurement was designed in order to minimize the size of the sample and improve the extraction efficiency. The new system crushes samples of 20-40 g in 5 sec by rotating the chamber on the horizontal plane. From the measurements of the grain size distribution we can conclude that this system provide the best finest powder with respect to other existing extraction methods. However its efficiency is not yet close to 100% for clathrate ice. The precision of the ring mill system is ~2 ppmv on average, and this precision may differ depending on the timing when the measurement is conducted. Thus, a blank test result conducted every 5 measurements should be performed for data correction. The ring system therefore provide a higher extraction efficiency at the price of a lower measurement precision. Further investigations are therefore required for making the system more stable over time and for improving its precision. Using larger samples to reconstruct CO₂ concentrations should be considered. In this case, fewer replicates can be made, but inaccuracies related to contamination in the ice core can be minimized. In this thesis, due to the limited number of

measurements, the accuracy of the new system could not be verified. Additional measurements on the TALDICE are needed.

Chapter 6

Manuscript in preparation

Millennial-scale atmospheric CO₂ variations during the Marine Isotope Stage 6 period (190-135 kyr BP)

Jinhwa Shin⁽¹⁾, Christoph Nehrbass-Ahles⁽²⁾, Roberto Grilli⁽¹⁾, Jai Chowdhry Beeman⁽¹⁾, Frédéric Parrenin⁽¹⁾, Grégory Teste⁽¹⁾, Amaelle Landais⁽³⁾, Loïc Schmidely⁽²⁾, Jochen Schmitt⁽²⁾, Thomas Stocker⁽²⁾, Hubertus Fischer⁽²⁾ and Jérôme Chappellaz^{(1)*}

(1) CNRS, Univ. Grenoble-Alpes, Institut des Géosciences de l'Environnement (IGE),
Grenoble, France

(2) Climate and Environmental Physics, Physics Institute, and Oeschger Center for Climate
Change, University of Bern, Switzerland

(3) Laboratoire des Sciences du Climat et de l'Environnement, LSCE/IPSL, CEA-CNRS-
UVSQ, Université Paris-Saclay, 91191, Gif-sur-Yvette, France

*Corresponding author: Jérôme Chappellaz (jerome.chappellaz@univ-grenoble-alpes.fr)

Abstract

Understanding natural carbon cycle / climate feedbacks on various time scales is highly relevant for anticipating future climate changes. Here we make profit of contrasting climatic conditions during the last two glaciations to evaluate the comparative amplitude and dynamics of atmospheric carbon dioxide concentration changes. We reconstructed a new high-resolution, high precision data of atmospheric CO₂ from the EPICA / Dome C ice core during MIS 6 (190 to 135 kyr BP). Five CO₂ peaks with an amplitude of 15 to 25 ppmv are revealed. They appear remarkably associated with Antarctic temperature changes at millennial time scale, as depicted from water isotopes from the same core. Their amplitude is roughly correlated with the duration of North Atlantic stadial. Using methane as a stratigraphic marker of abrupt warmings in the northern hemisphere, we deduce the existence of two modes of CO₂ variations during MIS 6. One, corresponding to the earliest part of MIS 6 at around 181.5 ± 0.2 kyr BP, where carbon dioxide maxima (CDM) 6 lags abrupt warming in the Northern Hemisphere by only 100 ± 360 yrs, and the other one, for CDM 3 (169.7 ± 0.2 kyr BP) and CDM 4 (174.5 ± 0.2 kyr BP) where the lag is much longer, $1,100 \pm 280$ yrs on average. These two modes of CO₂ relationship with abrupt warmings in the northern hemisphere may reflect a major change in the organization of the Atlantic Meridional Overturning Circulation (AMOC), itself related with the intensity of the hydrological cycle.

6.1. Introduction

At multi-millennial time scales, atmospheric CO₂ is primarily governed by carbon exchange with the oceans and the land biosphere; therefore changes of these two reservoirs of carbon can impact atmospheric CO₂ levels (Friedlingstein et al., 2006). Understanding the relationship between the carbon cycle and climate is an important issue for accurate projections of future climate change.

Air bubbles occluded in Antarctic ice cores are a unique archive which permits us to look into the history of atmospheric CO₂. Existing records cover the last 8 glacial-interglacial cycles (Lüthi et al., 2008), i.e. the last 800 kyr before present (BP, present is defined as 1950). In addition to revealing the ~100 ppmv changes associated with glacial-interglacial transitions, existing records also indicate the existence of millennial-scale oscillations of the order of 20 ppmv, occurring during the last glaciation, that strongly co-vary with temperature in Antarctica on millennial time scales (Bereiter et al., 2012). However, the mechanisms responsible for these oscillations are still subject to debate. The comparison between the last two glacial periods, Marine Isotope Stage 3 (MIS 3, 60–27 kyr BP) and the earliest part of Marine Isotope Stage 6 (early MIS 6, 185–160 kyr BP) can provide better clues on the mechanisms at work, due to different boundary conditions of the climate system.

During the early MIS 6 period, six millennial-scale climate oscillations are observed in Antarctic temperature, in the North Atlantic region, and at low latitudes, similar to observations covering MIS 3 (Cheng et al., 2016; Jouzel et al., 2007; Margari et al., 2010) (Figure 6.1). During the MIS 6e at around 175 kyr BP, summer insolation levels in the Northern Hemisphere approached interglacial values (Berger, 1978). Due to the stronger Northern Hemisphere insolation, the intertropical convergence zone (ITCZ) was shifted northward, intensifying monsoon systems in low latitude regions, such as in Asia, Italy and Israel (Ayalon et al., 2002; Bard et al., 2002; Cheng et al., 2016), and leading to a weaker overturning circulation (Margari et al., 2010).

During MIS 3, millennial-scale variability was marked by opposite temperature variations in the Northern and Southern Hemispheres, referred to as the bipolar seesaw mechanism (EPICA Community Members, 2006). An similar inverse relationship between planktonic $\delta^{18}\text{O}$ records from the Portuguese margin in the North Atlantic, co-varying with Greenland temperature proxies, and benthic $\delta^{18}\text{O}$ at the same place, co-varying with temperature in Antarctica (Shackleton et al., 2000), indicates that the bipolar see-saw mechanism took place both during MIS 3 and MIS 6. However, events of iceberg discharge into the North Atlantic, which impacts oceanic circulation, appeared to be much more frequent during MIS 3 than during MIS 6 (Margari et al., 2010; Margari et al., 2014). The North Atlantic overturning cell was weaker during MIS 6 than during MIS 3, and the shape of the $\delta^{18}\text{O}_{\text{benthic}}$ record (Figure 6.1D) is almost right-angled triangular, which may indicate that the AMOC cell was shallower (Margari et al., 2010).

In order to investigate if the different boundary conditions between MIS 6 and MIS 3 could have impacted the relationship between atmospheric CO₂ and climate, we reconstructed atmospheric CO₂ concentrations from the EPICA Dome C (EDC) ice core (75°06'S, 123°24'E) with 150 new data points spanning MIS 6 (190 to 135 kyr BP), largely improving existing records previously obtained from the Vostok ice core (Petit et al., 1999). With our new reconstruction, the average temporal resolution during MIS 6 reaches 360 yr compared to 1,000 yr in the Vostok record. Over the early time period of MIS 6 when millennial-scale variability is observed in the Antarctic climate record (185-160 kyr), the total of 100 new CO₂ measurements provide a temporal resolution of ~280 yr.

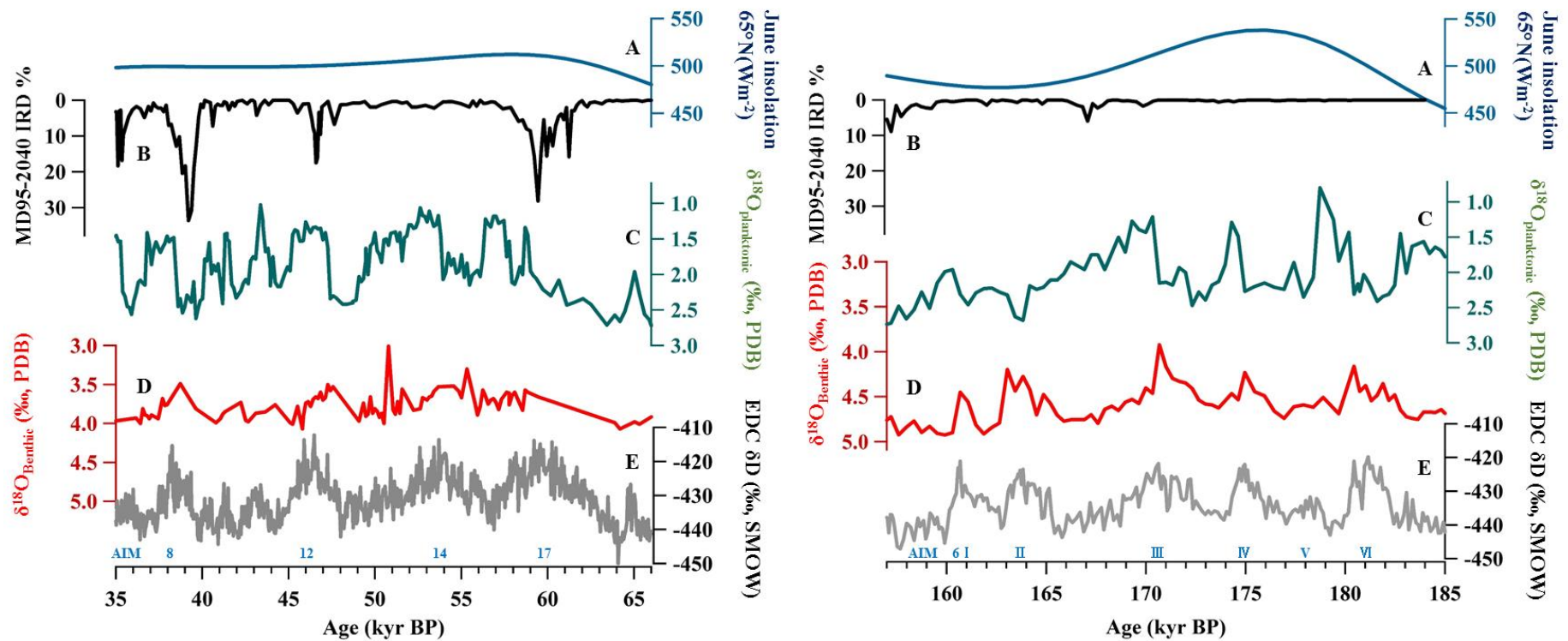


Figure 6.1. Comparison of climate related signals during MIS 3 (left) and 6 (right) period. **A:** 21 June insolation at 65°N (Berger, 1978). **B:** Ice-rafted debris (IRD) input in the Iberian margin core MD95–2040 (de Abreu et al., 2003). **C:** $\delta^{18}\text{O}$ of planktonic foraminifera in the Portuguese margin marine Core MD01–2444 (Margari et al., 2010). **D:** $\delta^{18}\text{O}$ of Benthic foraminifera in the Portuguese margin marine Core MD01–2444 (Margari et al., 2010). **E:** Temperature in Antarctica from δD composition of the EDC ice core (Jouzel et al., 2007).

6.2. Methods

6.2.1. CO₂ measurements

Atmospheric CO₂ was reconstructed using the traditional dry ball mill gas extraction system and gas chromatography at IGE (Schaefer et al., 2011). Each data point presented in this study corresponds to a single 40 g ice sample measured five times (five consecutive injections of the same extracted gas). 5 mm were trimmed from the ice core surface in order to remove the ice that could be altered through molecular diffusion between the ice lattice and outside air during storage in the freezer (Bereiter et al., 2009). The precision of the system was ~1 ppmv during these measurements. Absolute values of CO₂ measurements are referenced to a gas standard (synthetic air built by Air Liquide company) containing 233.7±0.4 ppmv of CO₂ in dry air on the NOAA and CSIRO reference scale. The new EDC CO₂ data were corrected for CO₂ contamination, based on blank tests conducted with artificial bubble-free ice combined with the Air Liquide gas standard. On average, the correction corresponds to a reduction of the measured CO₂ concentration by 1.7 ppmv.

150 individual ice samples were measured in the depth range from 1787.5 to 2036.7 m along the EDC ice core, corresponding to the time period 135.4 to 189.4 kyr BP on the AICC2012 chronology (Bazin et al., 2013), thus leading to a mean temporal resolution of 360 yr (280 yr over the time period 160-185 kyr BP).

6.2.2. CH₄ measurements

We measured 63 additional samples for their CH₄ content, using the wet extraction method at IGE, allowing to improve the temporal resolution of existing CH₄ data during the MIS 6 period from ~600 yrs to 360 yrs on the AICC2012 chronology (Loulergue et al., 2008) (Figure 6.2).

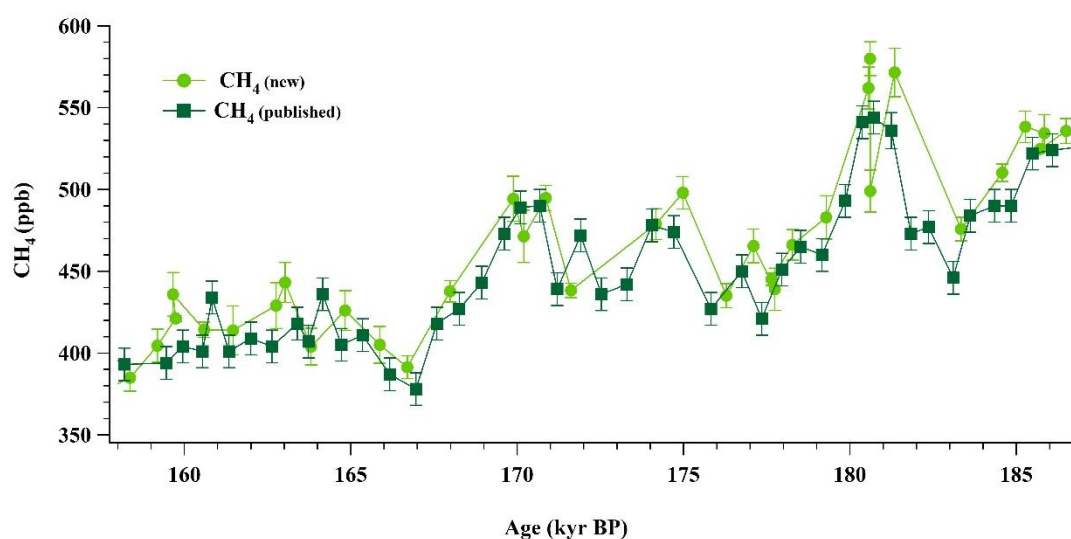


Figure 6.2. Atmospheric CH₄ concentrations from EDC ice core during MIS 6. Both dark green squares (Loulergue et al., 2008) and light green circles (in this study) are obtained at IGE.

The previous CH₄ dataset (Louergue et al., 2008) from EDC was produced at both institutes IGE and University of Bern (UBern). Because of different extraction methods, a systematic offset of 6 ppbv between IGE and UBern was observed (Louergue et al., 2008). In order to produce a coherent dataset, 6 ppbv were added to the data obtained at IGE (Louergue et al., 2008). However, in this study, to combine previous data with the new CH₄ data measured at IGE, 6 ppbv was subtracted from the previous compiled CH₄ record.

6.2.3. Nitrogen isotopes

Isotopes of molecular nitrogen in air bubbles were measured by a melting technique at the Laboratoire des Sciences du Climat et de l'Environnement (LSCE), France. The gas was extracted from the ice by a wet extraction technique and the released air was analysed by a dual-inlet mass spectrometer (Delta V Plus; Thermo Scientific). The analytical method and data correction are described in Landais et al. (2004). In total, 151 samples from 88 depth intervals between the depths of 1875.0 and 2124.7 m below the surface were measured, corresponding to 153.9 to 204.7 kyr BP (Figure 6.3). Measurements for 63 depth intervals (over 88) were duplicates. The average resolution on the AICC2012 chronology is ~580 yrs.

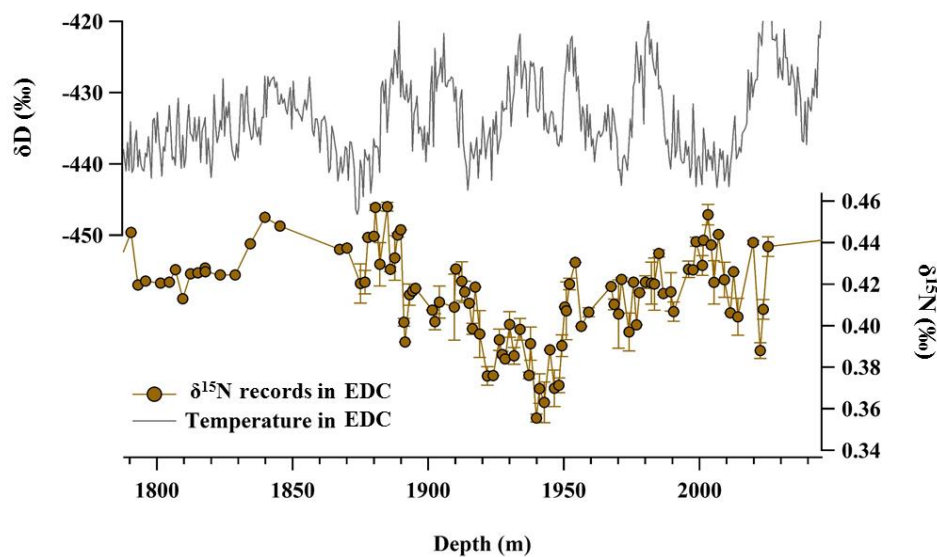


Figure 6.3. δD and $\delta^{15}N$ from Dome C ice core plotted as a function of depth. For $\delta^{15}N$, 88 new data points are added to the previous measurements (Landais et al., 2013). The error bar indicates the standard deviation of replicate.

6.2.4. Gravitational correction

The CO₂ record was corrected for gravitational fractionation, using the $\delta^{15}N$ isotope ratio (Sowers et al., 1992). The equation is as follows (Craig et al., 1988) :

$$[\text{CO}_2]_{\text{gravcorr}} = (1 - \delta^{15}\text{N}_2 \times (\text{M}_{\text{CO}_2} - \text{M}_{\text{air}})) \times [\text{CO}_2]_{\text{measured}} \quad (6.1)$$

where $[\text{CO}_2]_{\text{gravcorr}}$ is the corrected CO_2 data, $[\text{CO}_2]_{\text{measured}}$ is the concentration of CO_2 obtained on each sample, and M is the molecular weight of a species.

The 88 new data points (Figure 6.3) and existing $\delta^{15}\text{N}$ measured (from 156.4–139.2 kyr i.e. 1787.5 to 1870.2 m of depth) by Landais et al. (2013) were used to obtain the gravitational correction. $\delta^{15}\text{N}$ data were linearly interpolated in age to each corresponding CO_2 data point. On average, the correction corresponds to removing 1.2 ppmv to the measured CO_2 concentration.

6.2.5. Ice age revision by estimating Δdepth from $\delta^{15}\text{N}$ in air of ice core

Temperature variations in ice cores are recorded in water isotopes, which, unlike CO_2 , are measurement from the ice matrix. Air enclosed in an ice core moved into the porous firn layers at the top of the ice sheet through gas diffusion, and became trapped in ice at the so-called Lock-In Depth (LID, around 50-120 m below the surface depending on accumulation and temperature at the site). An age difference thus exists between the ice and the air at a given depth. In the conditions of the EDC ice core, the age difference can reach 5,000 yr and is associated with a large uncertainty (several hundred years, Loulergue et al., 2007). $\delta^{15}\text{N}$ of molecular nitrogen in air bubbles can be used to determine LID and to calculate the depth difference between synchronous events in the ice matrix and bubbles, called Delta depth (Δdepth), thus creating a more precise relative chronology of the gas phase with respect to the ice phase (Parrenin et al., 2013). We use the Δdepth calculation to adjust the ice chronology of Dome C, and the air chronology from AICC2012 remains in place.

We calculate the height of the air column in the firn, h , from $\delta^{15}\text{N}$ of N_2 measurements, by the following equation (Craig et al., 1988; Dreyfus et al., 2010; Sowers et al., 1989):

$$h = h_{\text{conv}} + (\delta^{15}\text{N} - \Omega(T) \Delta T_{\text{diff}}) \left(\frac{\Delta m \cdot g \cdot 1000}{RT} \right)^{-1} \quad (6.2)$$

In this equation, ΔT_{diff} is the temperature difference between the top and the bottom of the diffusive zone. $\Omega(T)$ is the thermal diffusion sensitivity, which has been estimated from laboratory measurements by Grachev and Severinghaus (2003). Δm is the mass difference between ^{14}N and ^{15}N (kg mol^{-1}), g is the gravitational acceleration (9.825 m s^{-2} for Antarctica), R is the universal gas constant ($8.314 \text{ J mol}^{-1} \text{ K}^{-1}$). Finally, h_{conv} is the height of the convective zone, which is considered as negligible at Dome C according to current observations (Landais et al., 2006). The variation of the convective height is related to changes in wind stress. According to Krinner et al. (2000), wind on the East Antarctic plateau varied little during the LGM (last glacial maximum), which is analogous to MIS6, and the convective zone was confirmed to be very thin during the LGM by Parrenin et al. (2012). Thus, we assume that h_{conv} is negligible during MIS6. Δdepth is calculated from the height of the air column using

a constant firn average density and a modelled vertical thinning function suggested by Parrenin et al. (2013).

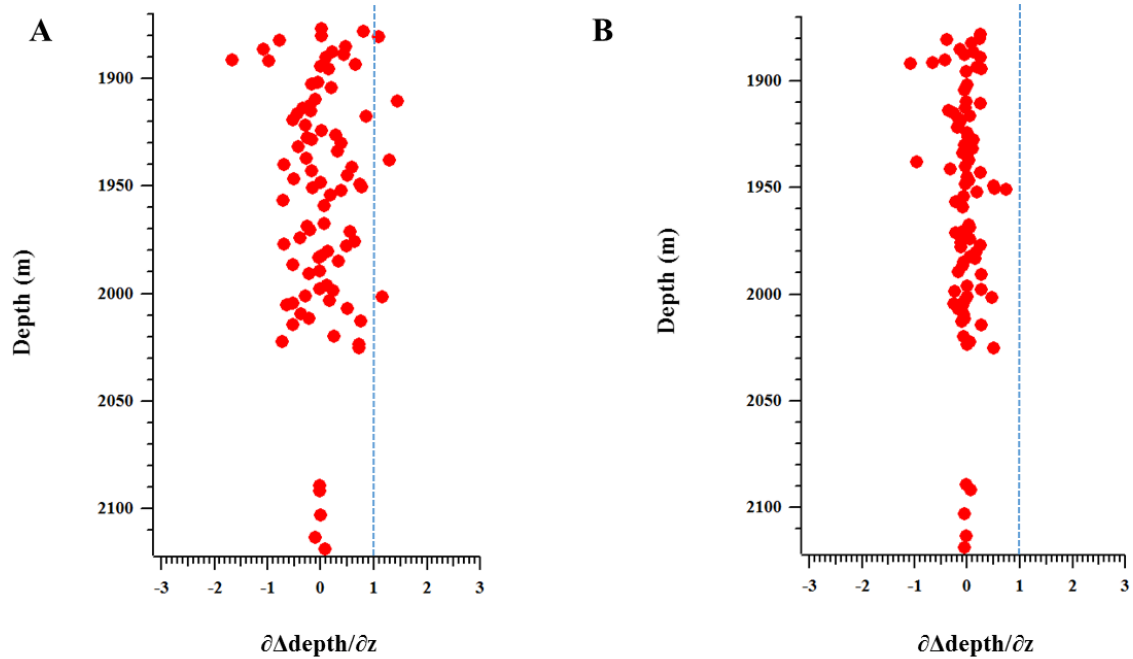


Figure 6.4. $\partial\Delta\text{depth}/\partial z$ as a function of depth. (A) from the raw $\delta^{15}\text{N}$ measurements. (B) from the 3-points running mean of $\delta^{15}\text{N}$ measurements. Vertical dashed line indicates when $\partial\Delta\text{depth}/\partial z$ function is 1.

Raw $\delta^{15}\text{N}$ data cannot be used directly to calculate Δdepth , because the age distribution of bubbles trapped at a given depth inside the same ice sample (Fourteau et al., 2017) can introduce noise into the record, notably through layer inversions. Although the latter should not strongly affect our record to its resolution larger than the scale of inversion events (Fourteau et al., 2017), the change in Δdepth between two different depths (z) in the ice core, denoted $\partial\Delta\text{depth}/\partial z$, deduced from the raw $\delta^{15}\text{N}$ data, shows values higher than 1, that could correspond to stratigraphic inversions in the gas phase (Figure 6.4). We thus applied a 3-points moving average to reduce this effect on the $\delta^{15}\text{N}$ data, corresponding to the smallest number of consecutive points necessary to bring $\partial\Delta\text{depth}/\partial z$ below 1 (Figure 6.4). Δdepth as estimated using the 3-points moving average is shown in Figure 6.5. The Δdepth values are used to update the EDC gas chronology from the original AICC2012 one, and the ice chronology remains unchanged. For MIS 6, this method significantly reduces the relative age uncertainty between air and ice, compared to the original AICC2012 chronology (Annex I). The relative age uncertainty between ice and air is 900 yrs on average.

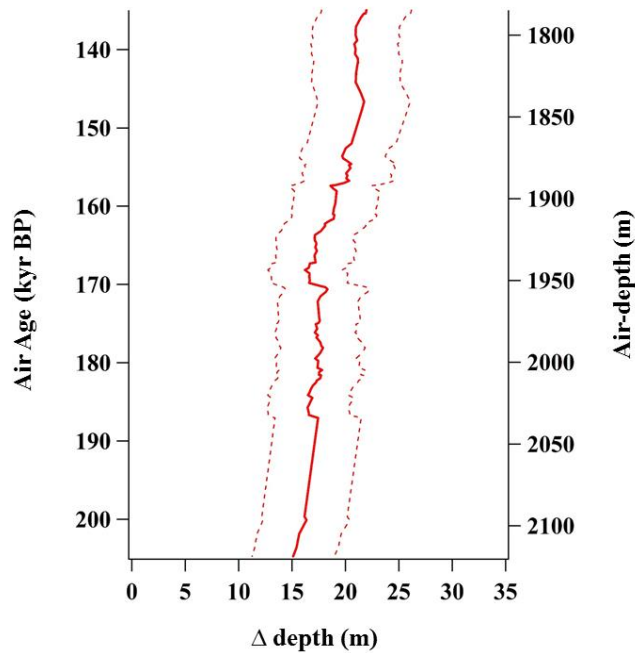


Figure 6.5. Δ depth (bold line) for EDC from 1787.5 to 1870.2 m below the surface, deduced from $\delta^{15}\text{N}$ and the thinning function calculated in this depth range. The two dash lines corresponds to the analytical uncertainties.

6.2.6. Age scale revision of the MD01–2444 marine sediment record

The MD01–2444 Marine sediment core from the Portuguese margin (Margari et al., 2010) is an important reference for the interpretation of our CO_2 record, as it is well-resolved during MIS 6, and as it provides high resolution benthic and planktonic foraminiferal proxy records. However, in order to make optimal use of the record, its relative chronology with respect to EDC requires additional tuning. The original MD01–2444 age scale was built by matching the benthic $\delta^{18}\text{O}$ record (Shackleton et al., 2000) to the δD record from EDC put on the EDC03 ice age scale (Parrenin et al., 2007), using 11 tie points selected by Margari et al. (2010) as shown in Table 6.1. The age of the sediment record was linearly interpolated between tie points. In order to revise the age scale, we recalculated the age of the tie points using the AICC2012 chronology.

Table 6.1. Ages of the tie points of MD01–2444 record on the EDC03 and new ice age scales.

MD01–2444 (m)	Ice depth -- Dome C (m)	Age Control points (EDC03 age scale, kyr BP)	New ice age -- Dome C (In this study, kyr BP)
22.02	1769.067	136.100	135.671
22.5	1798.500	141.686	141.828
23.7	1839.750	149.586	150.650

24.48	1888.150	159.105	160.679
24.72	1905.750	162.476	163.830
25.32	1934.143	168.273	170.669
25.71	1953.050	172.009	174.958
25.95	1969.550	175.461	178.889
26.01	1976.700	177.065	180.433
27.03	2026.200	188.009	190.334
27.3	2046.000	192.231	194.366

6.3. Results

6.3.1. The new high-resolution and high precision CO₂ record during MIS6

Figure 6.6 shows the new atmospheric CO₂ record from EDC during MIS 6, compared to the existing CO₂ data from Vostok (Petit et al., 1999). Both were measured using the ball mill extraction system at IGE. Atmospheric CO₂ from EDC is placed on the revised AICC12 air age scale and atmospheric CO₂ record from Vostok is placed on the AICC2012 air age scale (Bazin et al., 2013). The error bars indicate the standard deviation of 5 consecutive injections of the gas extracted from each sample into the GC. The average standard deviation of the EDC data set is ~1 ppmv, whereas it reaches ~3 ppmv for Vostok.

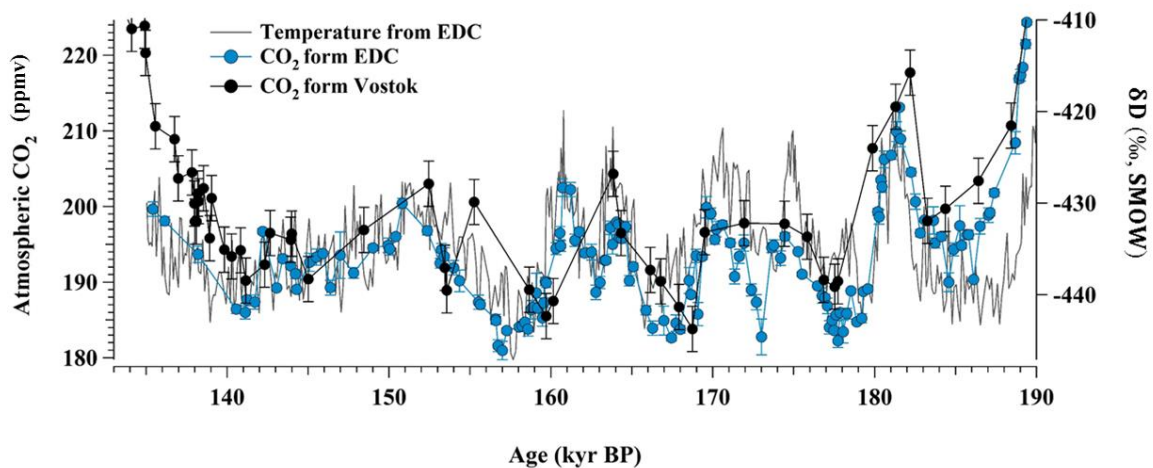


Figure 6.6. Atmospheric CO₂ from EDC (blue, this work) and Vostok (black, Petit et al., 1999) ice cores, compared to the δD of water at EDC (temperature proxy) (Jouzel et al., 2007) from 190–135 kyr BP.

Atmospheric CO₂ variability in the EDC shows similar general patterns as the one retrieved from the Vostok ice core, although new features appear thanks to the largely improved time resolution. However, CO₂ concentrations from Vostok appears systematically higher than those from EDC by 4.6

± 4.8 ppmv on average. Two main arguments may explain this offset: the Vostok record was not corrected for gravitational fractionation (amplitude comparable to the EDC one, i.e. a reduction of 1.2 ppmv on average), and contamination due to the extraction system was assumed as being negligible at the time of the Vostok sample measurements at IGE (Petit et al., 1999), while from the measurements conducted during this thesis it possibly amounts on average to an additional reduction of ~ 1.7 ppmv. Some of the differences in the two records might also be related with age scale uncertainties as well, due to the limited number of stratigraphic tie points between the two cores (Bazin et al., 2013). Lastly, the atmospheric CO₂ measurements from the Vostok ice core are affected by a larger analytical uncertainty than the EDC ones.

6.3.2. Relationship between temperature in Dome C and atmospheric CO₂

The lowest atmospheric CO₂ concentration observed in our new MIS 6 data set is 181.0 ± 1.22 ppmv at approximately 157.0 kyr BP, and the maximum concentration is 213.1 ± 0.3 at 181.5 kyr BP. During the entire MIS 6 interval, the new EDC CO₂ record and EDC temperature are synchronous on millennial time scales within age uncertainty on millennial time scales (160 ± 900 yrs using a maximum lag correlation coefficient estimate, and taking into account the relative age uncertainty between ice and air).

Our new record clearly shows millennial variability of CO₂ concentrations in much more details than previous records, thanks to the improved time resolution and precision of the obtained CO₂ data (Figure 6.7). MIS 6 can be divided in three sections depending on the degree of climatic variability observed in proxy data (Margari et al., 2014): early (185.2–157.7 kyr BP), transition (157.7–151 kyr BP) and late MIS 6 (151–135 kyr BP). CO₂ variations on millennial time scales are pervasive during the early MIS 6 period (185–157.7 kyr BP). During the transitional period from 157–151 kyr BP, atmospheric CO₂ increased slowly, while, during the late MIS 6 period, CO₂ variation is subdued.

The correlation coefficient, r , between CO₂ and Antarctic temperature during early MIS 6 is 0.61. During the transition it reaches 0.95, whereas during late MIS 6 it goes down to 0.34.

6.3.3. Millennial variabilities during early MIS 6 period

To better discuss millennial variability in MIS6, a Savitsky Golay filter with a 500 yr cut-off period (Bereiter et al., 2012), selected to filter out centennial-scale variability. Five major peaks, or Carbon Dioxide Maxima (CDM) and one minor (however relying on a single data point) were detected in atmospheric CO₂ during early MIS6 (Figure 6.7). The five major peaks are observed at 160.9 ± 0.3 (CDM 1), 164.1 ± 0.3 (CDM 2), 169.7 ± 0.2 (CDM 3), 174.5 ± 0.2 (CDM 4) and 181.5 ± 0.2 (CDM 6) kyr BP. Each major CDM is associated with a major Antarctic Isotope Maximum (AIM) event. However, during the short AIM V event, the corresponding CDM 5 has an amplitude of only ~ 4 ppmv and relies on a single data point, which becomes even less pronounced after filtering. Considering the uncertainty

surrounding this CDM event, it may correspond to a period of time when atmospheric CO₂ and Antarctic temperature are decoupled. Such conclusion seems confirmed when considering the relationship between atmospheric CO₂ change and the duration of North Atlantic stadials (Annex II for detail about the analysis), as shown in Figure 6.8. The magnitude of atmospheric CO₂ change is generally correlated

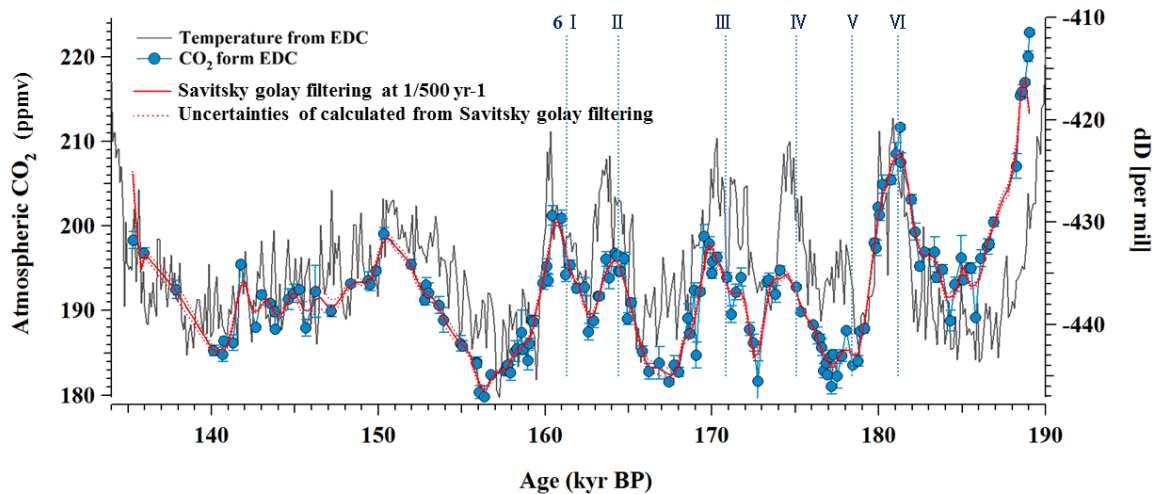


Figure 6.7. Atmospheric CO₂ from EDC (this study) and EDC water isotopic record (Jouzel et al., 2007). Red line indicates Savitsky Golay filtering curve made with a 500 yr cut-off period (red dotted line) Vertical dotted lines indicate the six CDM events that we identify during the early MIS 6.

with the North Atlantic stadial duration ($r=0.6$) during the early MIS 6 period.

We note a similar event during MIS 2, when the North Atlantic stadial duration was shorter than 1,500 yrs, atmospheric CO₂ varied less than 5 ppmv (35–22 kyr BP period, Ahn and Brook, 2014), and the same holds for the shortest North Atlantic stadials during MIS 3 (AIMs 9, 10 and 11). During the short stadials in MIS 3 and MIS 2, the CO₂ maxima do not appear to have a consistent phase relationship with AIMs (Bereiter et al., 2012) and CO₂ and δD_{ice} anomalies were not correlated during the short stadials during MIS 2 ($r = 0.0$ on average)(Ahn and Brook, 2014). However, in all three periods, CO₂ is highly correlated with δD_{ice} anomalies during the long stadials ($r = 0.84$ on average) with a stronger increase in CO₂.

We found that the amplitude of atmospheric CO₂ variations is well related with the North Atlantic stadial duration. However, the way how durations were calculated by Margari et al. (2010) is quite subjective and temporal resolution of $\delta^{18}O$ composition of planktonic foraminifera in MD01–2444 and the age scale were not enough for precisely define the duration. Additional proxy data providing

information about climate change in NH are needed to confirm the relationship between atmospheric CO₂ variations and the North Atlantic stadial duration (Annex II).

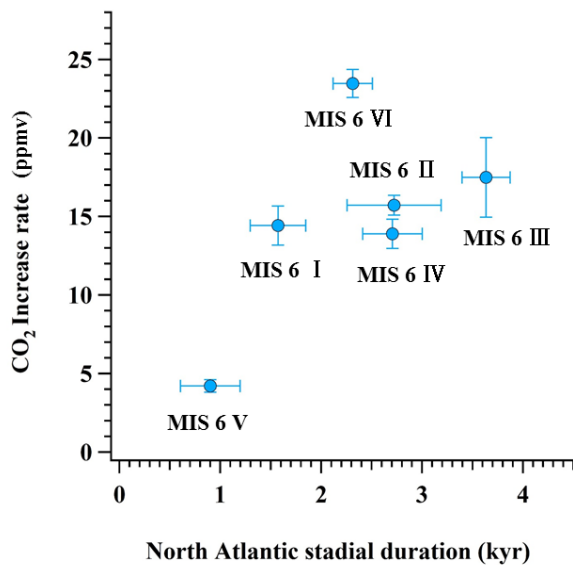


Figure 6.8. The relationship between North Atlantic Stadial duration and magnitude of CO₂ increase during the early MIS 6 period

6.3.4 Leads and lags between CO₂ and the abrupt warming in Northern Hemisphere

To better understand the link between the bipolar see-saw mechanism and atmospheric CO₂ variability on millennial time scales, we calculated the varying time lag for each CDM following an abrupt warming events in the NH (Annex III and IV). Due to the lack of a direct temperature record in Greenland covering MIS6, and due to the fact that the $\delta^{18}\text{O}$ composition of planktonic foraminifera in North Atlantic sediment cores, which could be used in principle as an indicator for abrupt warming in the NH (Shackleton et al., 2000), cannot be placed with enough precision on a common chronology with the EDC ice core, in this work CH₄ measurements performed on the EDC ice core were used as a time marker of rapid warming in the NH. Both CH₄ and CO₂ being recorded in the same bubbles, there is no inherent chronological uncertainty when comparing the timing of changes of both signals. The only remaining uncertainty is related with analytical uncertainties and with the temporal resolution of the two signals.

Figure 6.9 shows the shifts of CDM with respect to the onset of the abrupt warming in the NH. During the MIS 6 period, three abrupt NH warmings at 181.6 ± 0.25 , 175.4 ± 0.40 and 171.0 ± 0.17 kyr BP (2σ) were found. These events correspond to CDM 6, 4 and 3, respectively.

Two modes describing CO₂ variations can be identified from this chronological comparison between EDC CH₄ and CO₂. The first mode is observed for CDM 6: atmospheric CO₂ increases rapidly (by ~4.2 ppm in 100±360 yrs) following the abrupt CH₄ increase at 181.6±0.25 kyr BP. The peak of CDM 6 is nearly synchronous with the onset of the NH abrupt warming (not significant lag of 100±360 yrs, Figure 6.9). In mode 2, visible for CDM 3 and 4, CO₂ concentrations show a much slower increase over a duration of ~3.3 kyrs. This time, CO₂ during CDM 3 and 4 lags behind the onset of the NH abrupt warming by 1,300±280 yrs and 900±450 yrs, respectively (1,100±280 yrs on average). Interestingly, these two CDM events occurred during MIS 6e, when summer insolation in the NH was comparable to interglacial levels, the North Atlantic Deep Water (NADW) was shallower (Margari et al., 2010), and the hydrological cycle (estimated using speleothem δ¹⁸O) was more intense (Cheng et al., 2016) with respect to the earliest part of MIS 6. Therefore the two apparent modes of CO₂ variations during MIS 6 might be explained by these different background climate conditions (Annex V).

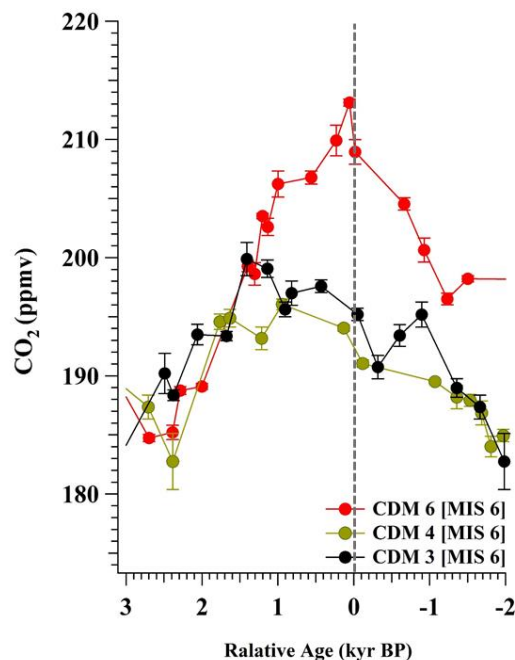


Figure 6.9. Atmospheric CO₂ variations of CDM 3, 4 and 6 with respect to the onset of NH abrupt warming. Grey dotted line indicates when climate change abruptly in the NH.

Indeed, these features during MIS 6 appears fully comparable with those observed during the last glacial period. Figure 6.10 shows the trend of CDM with respect to the onset of abrupt warming in the NH during MIS 3, and MIS 5. The three combined cover the whole sequence of rapid events of the last glacial period (Ahn and Brook, 2014; Bereiter et al., 2012). Atmospheric CO₂ during MIS 3, as shown in this Figure 6.10, was reconstructed from the Talos Dome ice core (TALDICE). For MIS 5 it was obtained from Byrd and the EPICA Dronning Maud Land (EDML) ice core (Ahn and Brook, 2008; Bereiter et al., 2012). In Bereiter et al. (2012), both TALDICE and EDML records were used during

MIS 3 and compared to the onset of abrupt warming in the NH. However here, we only use data from TALDICE which are more accurate due to the narrower age distribution of the gas trapped in the LID (Bereiter et al., 2012). Using the same method, the average value of CDM lag with respect to the abrupt warming in NH was calculated. The average CDM lags with respect to the abrupt warming in NH for the MIS 3 and 5 period are 770 ± 180 , and 280 ± 237.1 yr. Thus in the course of the last glaciation, the lag of CO₂ maxima with respect to NH millennial warmings significantly increases. We observe the same trend through the millennial events depicted during MIS 6, albeit with different absolute lags. If the earlier CO₂ maximum corresponding to CDM 6 during MIS 6 shows no significant lag, thus close to the small lag of 190 ± 110 yr observed during MIS 5, the lag between NH warming and CDM 3 and 4 is closer to the lags of CDMs during MIS 3.

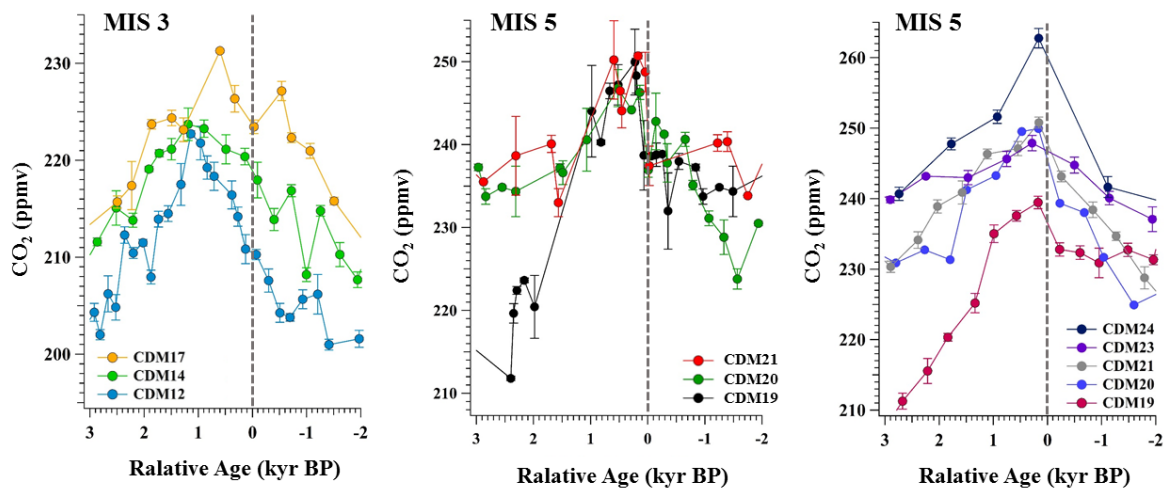


Figure 6.10. CDM lags relative to abrupt temperature increase in NH. Grey dotted line indicates when climate changes abruptly in NH. Atmospheric CO₂ was recorded from TALDICE (MIS 3), Byrd (MIS 5) and EDML (MIS 5).

6.4. Discussion

6.4.1. Atmospheric CO₂ variability on millennial time scale

We found that the amplitude of atmospheric CO₂ variations is related with the duration of North Atlantic stadials during MIS 6 (Figure 6.8). This observation may imply that the amplitude of CO₂ variations was related with the strength of AMOC perturbations during the early MIS 6 period.

The relationship between the magnitude of Antarctic temperature increase and the duration of AMOC disruption has been investigated for the last two glacial periods using a thermodynamic model (Margari et al., 2010) (Figure 6.11). The bipolar see-saw theory by Stocker and Johnsen (2003)

suggested that if AMOC perturbation is constant during North Atlantic stadials, Antarctic temperatures increase exponentially to an equilibrium level. In addition, if the strength of the AMOC largely reduces, the temperature in Antarctica will increase asymptotically. Figure 6.11 shows the relationship between the changes in temperature in Antarctica and the duration of North Atlantic stadials (Margari et al., 2010). The grey curved lines indicate how Antarctic temperature can change for different strengths of AMOC perturbation.

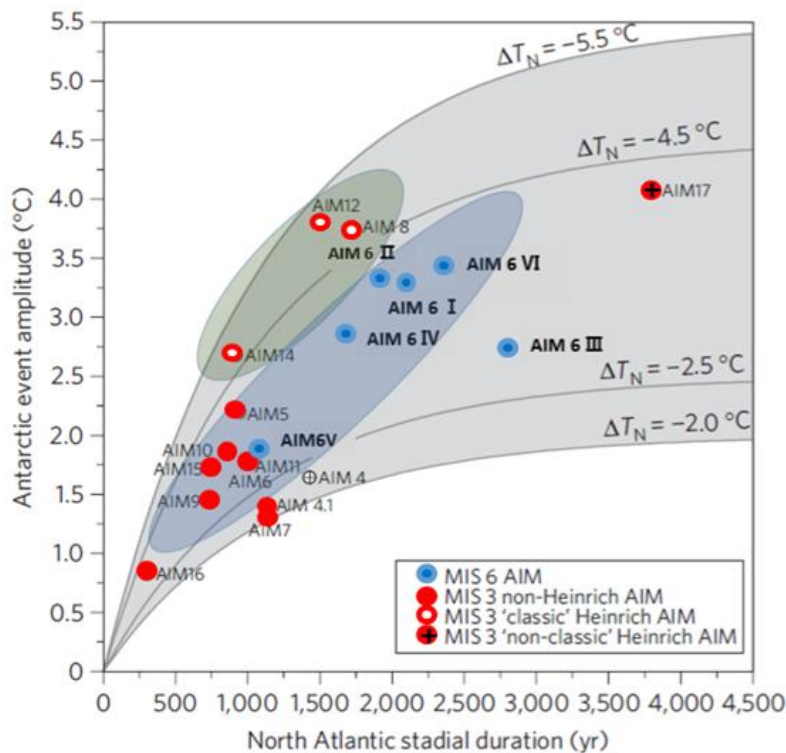


Figure 6.11. The relationship between the duration of North Atlantic stadial and the amplitude of Antarctic temperature (Margari et al., 2010). ΔT_N : the amplitude of North Atlantic cooling. Curved line in grey: Antarctic temperature response for the different ΔT_N , which is estimated by thermodynamic see-saw model (Stocker and Johnsen, 2003).

During AIM8, AIM12 and AIM14 events (Heinrich events), Antarctic warming with respect to the duration of North Atlantic stadials is higher than those during other AIM events (non-Heinrich events). This observation indicates that during the Heinrich events AMOC perturbation was stronger than that during other stadials (non-Heinrich events).

According to the model results of Margari et al. (2010), the six AIM events of MIS 6 have probably been affected by AMOC perturbations of similar strength (Figure 6.11). They are not classic Heinrich events (Figure 6.1 and 6.11), and the strength of the associated AMOC perturbations is estimated to be similar to that during non-Heinrich AIM events of MIS 3. Furthermore, duration of

North Atlantic stadials during the early MIS 6 (except for AIM 6 V) are longer than that during non-Heinrich AIM events of MIS 3. This may be explained by the increase of precipitation during MIS 6 and different boundary conditions.

This observation suggests that perturbations to AMOC might control atmospheric CO₂ concentrations during MIS 6 period, which is supported by numerical simulations (Menviel et al., 2014; Schmittner and Galbraith, 2008). Menviel et al., 2014 report that when large amounts of low-density fresh water are released into the North Atlantic, the AMOC is shut down. Thus, heat piles up in the South and moisture movement from the Atlantic to the Pacific is reduced. Therefore, sea ice retreats in the Southern Ocean. On the other hand, the North Atlantic is cooled, and the ITCZ is shifted to the south. Changes in precipitation connected to ITCZ shifts (mainly in northern Africa and northern South America) may cause variations in terrestrial carbon stocks (Menviel et al., 2008). Salinity at the surface of the Pacific Ocean is increased. Thus, AABW and North Pacific Deep Water (NPDW) transport is enhanced (Menviel et al., 2014). Enhanced NPDW transport ventilates deep Pacific carbon via the Southern Ocean. Thus, atmospheric CO₂ increases.

The relationship between the amplitude of CO₂ variations and duration of North Atlantic stadials may be explained by the response of the Deep Ocean and terrestrial biosphere to the AMOC shutdown (Menviel et al., 2014; Schmittner and Galbraith, 2008). In general, atmospheric CO₂ on millennial timescales can be controlled by CO₂ exchange between the Ocean and the Atmosphere, as well as changes of terrestrial carbon stocks. Coupled climate carbon cycle models reported that the variations of atmospheric CO₂ concentration on millennial timescales are mainly dominated by deep ocean inventory, requiring a few millennia to react to climate change (Schmittner and Galbraith, 2008). These variations of CO₂ concentration might be compensated by fast changes in the terrestrial biosphere (Bouttes et al., 2011; Menviel et al., 2014; Schmittner and Galbraith, 2008). The response of the terrestrial biosphere and Deep Ocean to AMOC are opposite, and during short stadials, a change in the carbon stock of the terrestrial biosphere can compensate the slow response of the deep Ocean. Thus, atmospheric CO₂ variation is rather muted during short stadials, even though other SH climate proxies like dust flux and Antarctic temperature show significant variations. However, during long stadials, the response of the terrestrial biosphere stops, but the deep ocean inventory still responds to climate changes, and atmospheric CO₂ varies significantly.

Another possible reason for the difference between CO₂ changes during short and long stadials may be related with the reduction of the NADW during long stadials, which would cause a stronger upwelling of deep water in the Southern Ocean (Menviel et al., 2008; Schmittner et al., 2007). When large amounts of low-density fresh water are released into the North Atlantic, NADW formation can be slowed down. These events may reduce stratification in the Southern Ocean due to an increase in salinity of the surface waters and a relative freshening of the deep water.

As a result, atmospheric CO₂ can be enriched due to upwelling and outgassing of CO₂ in the Southern Ocean (Schmittner et al., 2007). However due to lack of proxy data with precise age scales for upwelling in the Southern Ocean, this remains a hypothesis. During the short stadials in MIS 6 (AIM 6 V in Figure 6.11) and MIS 3 the behaviour of AMOC disturbance is estimated to be similar. During the last glacial period, this is supported by the marine proxy data for upwelling in the Southern Ocean which do not show strong variation during short stadials for both MIS periods (Anderson et al., 2009).

The limited available proxy data permit only an exploratory discussion of the mechanisms responsible for CO₂ variability during MIS6. To compare the behaviour of the bipolar see saw with atmospheric CO₂ variations, additional proxy data related to the strength of AMOC disturbances are needed.

6.4.2. Why did CO₂ lag the abrupt warming in the NH during MIS 6e?

Modes of CO₂ variations are present in the MIS 6 period (Figure 6.9). CDM 6 is nearly synchronous with the abrupt warming in the NH (no significant lag of 100 ± 360 yrs), while the lags for CDM 4 (900 ± 450 yrs) and CDM 3 ($1,300\pm 280$ yrs) and are much longer. This CO₂ variations are also observed during the last glacial period. In the course of the last glaciation from MIS 5 to MIS 3 (Figure 6.10), the lag of CO₂ maxima with respect to NH millennial warmings significantly increases. These two modes of CO₂ variations can be explained by the different AMOC setting from MIS 5 to MIS 3 (Bereiter et al., 2012). As observed during last glacial period, a mode change of oceanic circulation between the earliest part of MIS 6 to MIS 6e might be related with the time lags between NH abrupt warming events and CO₂ variations during the early MIS 6.

The AMOC is composed of the Antarctic Bottom Water (AABW), the upper overturning cell, and NADW, the lower overturning cell (Figure 6.12). During MIS 3 (Figure 6.10), the oceanic circulation in the Atlantic was in a “Glacial” state while during the MIS5 was more in a “modern-like” state. Differently from MIS 5, in MIS 3 NADW was shallower thus and carbon-rich AABW extended to the north. At the onset of Dansgaard-Oeschger (DO) events, AMOC is thought to accelerate rapidly, delivering heat to the north and resuming the formation of NADW. When the NADW cell expands, AABW is withdrawn and an upwelling of carbon-rich deep water in the Southern Ocean is enhanced.

Therefore, due to the northward expansion of AABW before the onset of DO events in the MIS 3 period, additional carbon may have been added to the atmosphere by deep water exchange from carbon enriched AABW to the NADW. Thus, CO₂ continues to be released into the atmosphere for another 500 to 1,000 years while NADW formation continues (Bereiter et al., 2012). However, during

MIS 5 due to the lack of carbon exchange between AABW and NADW in the North Atlantic, less CO₂ is thought to be released from the ocean to the atmosphere.

The temporal resolution of proxy data related to oceanic circulation during MIS 3 and 5 is unfortunately not sufficient to validate from the marine realm itself if the two different modes of CO₂ variations reflect the hypothesized mechanism described above. Modelling studies of the carbon stock in AABW and NADW during MIS 5 and 3 have been attempted. Depending on the chosen model, the modes of atmospheric CO₂ variation are also different. For example, a study conducted by Menviel et al. (2008) generates an atmospheric CO₂ decrease when the AMOC is reduced because during the glacial period, NA was cooler and drier, and CO₂ release from the terrestrial biosphere can be reduced. Only one modelling study confirms an atmospheric CO₂ release from the ocean when the AMOC resumed (Bouttes et al., 2011).

It is possible that a similar change in the AMOC may explain the presence of two modes in MIS 6. The density of the North Atlantic surface water was low during MIS 6e (180–168 kyr PB) due to the higher intensity of the low latitude hydrological cycle (Ayalon et al., 2002; Bard et al., 2002; Cheng et al., 2016; Mélières et al., 1997). From the earliest MIS 6 to MIS 6e, NADW became shallower and the lag of CO₂ maxima with respect to NH millennial warmings significantly increases. Moreover, the AMOC cell appears to have been shallower during MIS 6e relative to MIS 3 (Margari et al., 2010), and so Bereiter et al. (2012)'s hypothesis would indicate an extended CO₂ release from an expanded AABW reservoir, potentially explaining the millennial-scale delays with respect to abrupt NH warming events. Another study by Wilson et al. (2015) shows that circulation conditions in the Atlantic Ocean during the earliest MIS 6 period were similar to those during the MIS 5, with deeper NADW and AMOC than during MIS 6e. This may explain the shorter lag between abrupt NH warming and CDM 6. However, in order to explain such long lags of CDM 3 and 4, NADW should be even shallower than in MIS 3.

To further investigate the applicability of the shallow-AMOC glacial hypothesis to the CO₂ variations observed in this study, we could compare CO₂ data with proxy data which can explain ocean circulation during the MIS 6 period. However, as is the case for proxy data during the last glacial period as well, the temporal resolution is unfortunately not sufficient to explain ocean circulation on millennial time scales. In addition, because of the low accumulation in Dome C, the estimation of the exact timing of CDM from the Dome C ice core might be less accurate compared to that from the TALDICE ice core, for example, due to the narrower distribution of air age in TALDICE (Bereiter et al., 2012). To

further investigate the exact relationship between CDM and abrupt warming in the NH, additional CO₂ measurements from a higher accumulation site could be helpful.

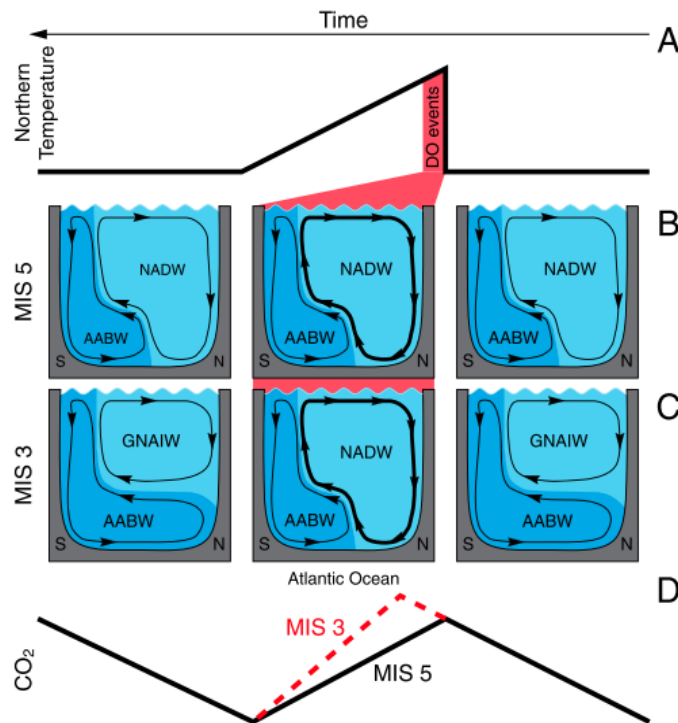


Figure 6.12. Schematic of a possible mechanism relating atmospheric CO₂ with water mass changes during the onset of DO events (Bereiter et al., 2012). (A) Layout diagram of Greenland temperature changes (B) North-South schematic of ocean circulation in the Atlantic ocean, showing how NADW (light blue) and AABW (dark blue) circulated (arrows) during DO events of MIS 5. (C) Changes of Ocean circulation of Glacial North Atlantic Intermediate Water mass (GNAIW, light blue) and during DO events in MIS 3. (D) Layout diagram of atmospheric CO₂ changes with respect to Ocean circulation in the Atlantic Ocean during DO events in MIS 5 (in black) and MIS 3.

6.5. Conclusion

We measured 150 samples of the EDC ice core to reconstruct atmospheric CO₂ during the MIS 6 period (189.4–135.4 kyr BP), with an unprecedented time resolution and analytical precision. Five millennial-scale atmospheric CO₂ changes are revealed during the early part of MIS 6 (189–160 kyr BP), with an amplitude of 15 to 25 ppmv, mimicking similar trends in Antarctic temperature. During the shortest stadials in the North Atlantic, atmospheric CO₂ variations are negligible and decoupled with temperature variabilities in EDC, probably because the duration of upwelling in the southern ocean was not sufficient to impact atmospheric CO₂. Two modes of CO₂ relationship with Northern Hemisphere warmings – as deduced from atmospheric CH₄ changes – are revealed during MIS 6. Carbon dioxide

maximum (CDM) 6 is nearly synchronous with the abrupt warming in the Northern Hemisphere (non-significant lag of 100 ± 360 yr), while the lags for CDM 3 and 4 are much longer, $1,100\pm 280$ yrs on average. These two modes of CO₂ variations might be related with a mode change of AMOC from the earliest MIS 6 to MIS 6e. Similar observations are drawn for the time period covered by our study in comparison with previous studies on MIS 3 and MIS 5 period, although the lag of CO₂ on Antarctic temperature reaches larger numbers during MIS 6e. However, the limited available proxy data from the marine realm only permits an exploratory discussion of the mechanisms responsible for CO₂ variability during MIS6. Because the boundary conditions of the last glacial period cannot be applied to MIS 6, additional proxy data and multiple modeling studies conducted during MIS 6 period are needed.

Acknowledgement

This work is a contribution to the “European Project for Ice Coring in Antarctica” (EPICA), a joint European Science Foundation/European Commission scientific program, funded by the European Union and by national contributions from Belgium, Denmark, France, Germany, Italy, The Netherlands, Norway, Sweden, Switzerland, and the United Kingdom. The main logistic support was provided by IPEV and PNRA. This is EPICA publication no. XX. It also received funding from the European Community’s Seventh Framework Programmes ERC-2011-AdG under grant agreement no. 291062 (ERC ICE&LASERS). As part of the PhD work of J. Shin, it was also supported by the LabEX OSUG@2020 project of the Grenoble Observatory of Sciences of the Universe (OSUG). Swiss authors also acknowledge long-term financial support by the Swiss National Science Foundation. The authors would like to thank G. Aufresne for assistance in the additional methane measurements, as well as X. Fain and K. Fourteau for help on the CH₄ analytical system and D. Raynaud for the very profitable discussions.

Annex I

Atmospheric CO₂ on the revised AICC12 air age scale and the AICC12 air age scale

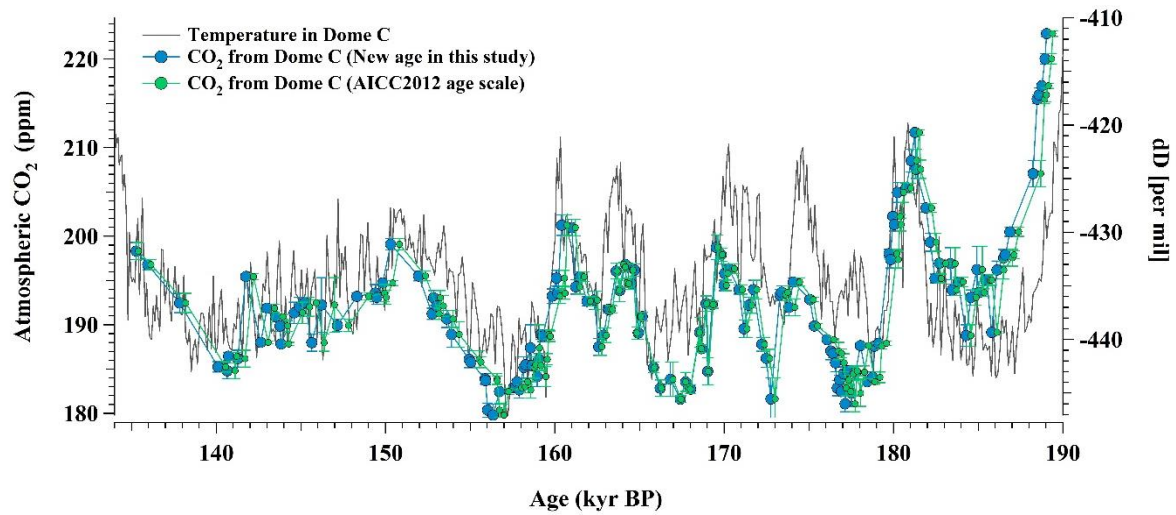


Figure 6.S1. Blue: Atmospheric CO₂ from EDC on the revised AICC12 age scale. Green: Atmospheric CO₂ from EDC on the AICC12 age scale. Grey: δD of water at EDC (temperature proxy) (Jouzel et al., 2007).

Annex II

Definition of North Atlantic stadial duration

Due to the absence of a Greenland temperature record for MIS 6, the durations of the six North Atlantic stadials identified during the MIS 6 period were previously defined by Margari et al. (2010) using the interval between the stadal transitions. Between the maximum and the preceding minimum of δD in the Dome C record is defined as the stadal transitions. However, this approach relies on the assumption that the bipolar seesaw was present during MIS 6. Here we instead use a secondary approach which was also proposed by Margari et al. (2010).

The durations of the six North Atlantic stadials were defined using $\delta^{18}O$ of planktonic foraminifera and tree pollen in MD01-2444, which reflect temperature variability in the NH (Margari et al., 2010). The interval between the maximum and the preceding minimum of both $\delta^{18}O$ of planktonic foraminifera and tree pollen in MD01-2444 were defined as the inflection point. The between two inflection points were defined as the North Atlantic stadial duration. In this approach, small variations of the two records may bias the calculation of the duration of short stadials in the NH. However, the average age difference between the durations identified using the two methods is only 205 years, which is less than the sampling resolution of MD01-2444 during MIS 6. The stadials identified for MIS 6 are shown in Figure 6.S1 and Table 6.1. The uncertainty of the duration of each stadial was estimated as half of the temporal difference between maxima and minima of $\delta^{18}O$ of planktonic foraminifera.

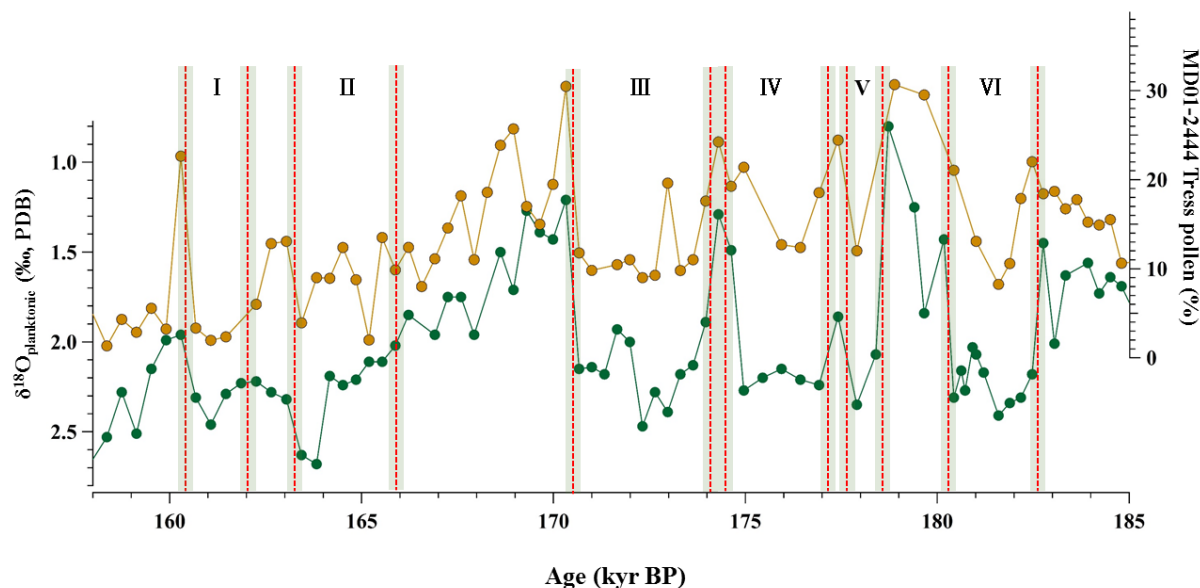


Figure 6.S2. Six variations on millennial time scales of Tree pollen percentage (top) and $\delta^{18}O$ of planktonic foraminifera (bottom) in the MD01-2444 selected by Margari et al. (2010).

Table 6.S1. The minima and maxima defining the duration of each North Atlantic stadial

	MIS 6 I		MIS 6 II		MIS 6 III		MIS 6 IV		MIS 6 V		MIS 6 VI	
	Min.	Max.	Min.	Max.	Min.	Max.	Min.	Max.	Min.	Max.	Min.	Max.
Age (kyr BP)	160.5	162.1	163.2	166.0	170.5	174.1	174.5	177.2	177.7	178.6	180.3	182.6
Uncertainty (kyr)	0.2	0.2	0.2	0.4	0.2	0.2	0.2	0.2	0.2	0.2	0.1	0.1

Annex III

Definition of the onset of abrupt climate change in the Northern Hemisphere

Over the last glacial period, rapid CH₄ jumps were always synchronous with abrupt temperature increases in Greenland within ± 50 ppbv (Huber et al., 2006). We pick intervals when CH₄ increases rapidly by at least 50 ppbv over a time period of less than 1 kyr that correspond with Antarctic isotope maxima (Loulergue et al., 2008). The timing of abrupt CH₄ increases was defined as the midpoint between the beginning of the increase of CH₄ and its maximum. The age uncertainty of the midpoint is defined by the time difference between the midpoint and either of the two endpoints.

We found three abrupt CH₄ increases during MIS 6 period at 171.0 ± 0.2 , 175.4 ± 0.4 and 181.6 ± 0.3 kyr BP (Figure S2). Due to the low accumulation rate and low temperature at the site during glacial periods, abrupt changes of CH₄ concentration might be smoothed, and identifying abrupt changes of CH₄ is more difficult than for interglacial periods. The climate change at 175.4 kyr BP does not seem to occur as abruptly as the other two, since CH₄ varied slowly over ~ 800 years. However, we include this event because corresponding data of $\delta^{18}\text{O}$ composition of planktonic foraminifera (Shackleton et al., 2000) indicate a rapid warming, and therefore an abrupt climate change in NH. Rapid increases during the last glacial period (MIS 3 and 5) are also calculated using this method to identify the onset of abrupt warming in NH. In total, eight changes are selected during this period (Figure S3–5).

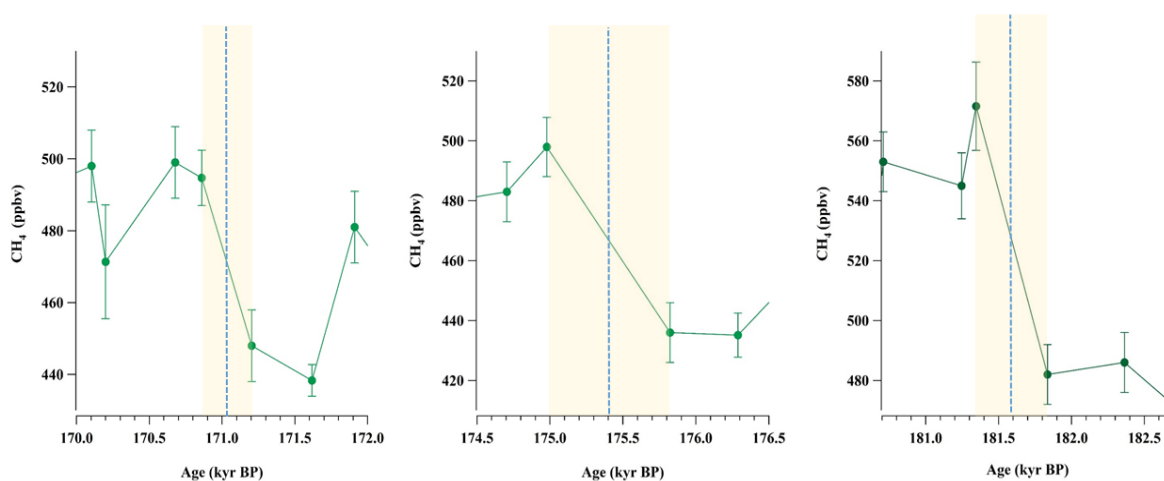


Figure 6.S3. Atmospheric CH₄ records from Dome C during MIS 6 period. Three boxes show CH₄ jumps at 171.0 ± 0.2 , 175.4 ± 0.4 and 181.6 ± 0.3 kyr BP.

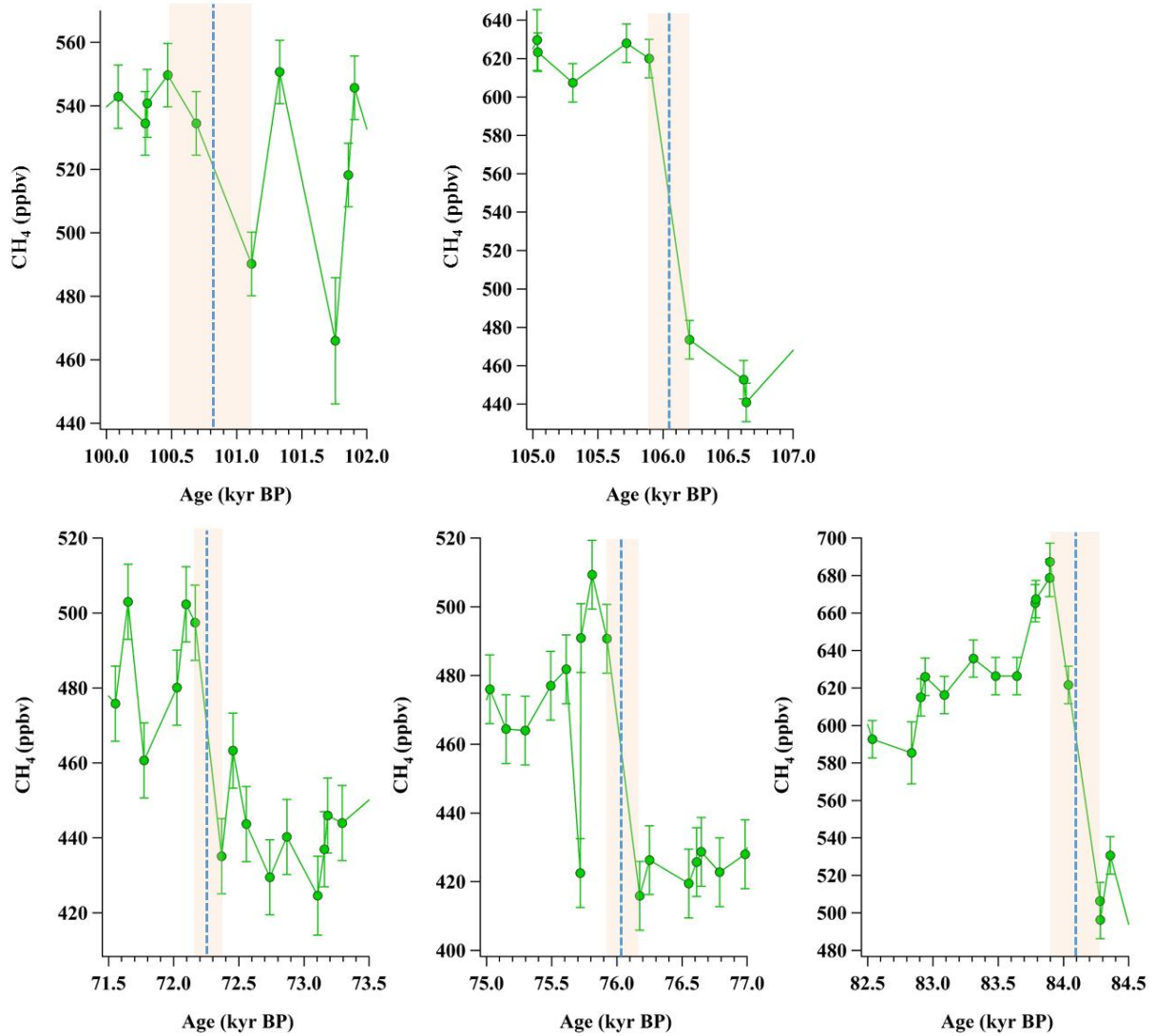


Figure 6.S4. Atmospheric CH₄ records from EDML during MIS 5 period. Two boxes show CH₄ jumps at 72.3±0.1, 76.0±0.1, 84.1±0.2, 100.8±0.5 and 106.0±0.2 kyr BP.

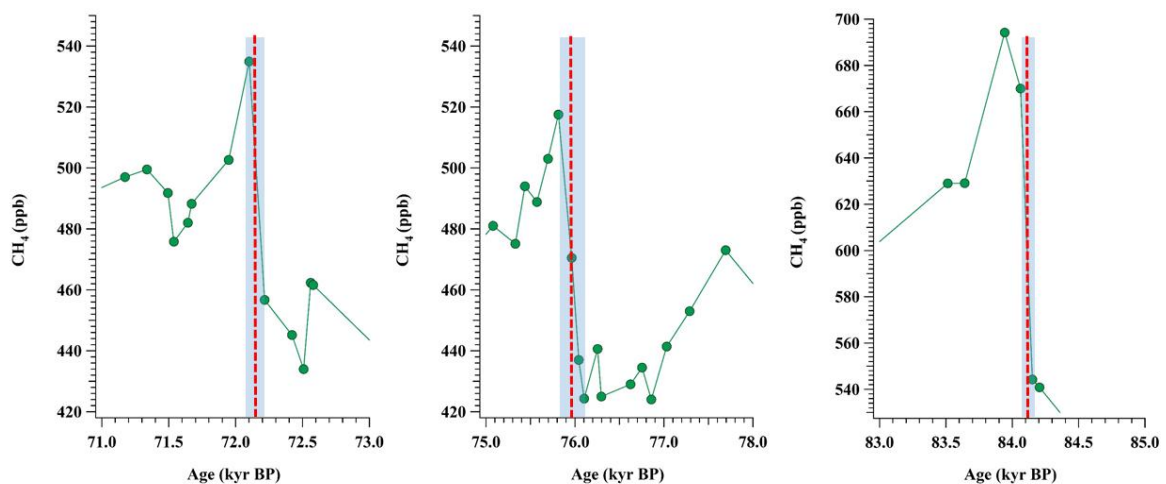


Figure 6.S5. Atmospheric CH₄ records from Byrd ice core during MIS 5 period. Three boxes show CH₄ jumps at 72.2±0.1, 76.0±0.2 and 84.1±0.04 kyr BP.

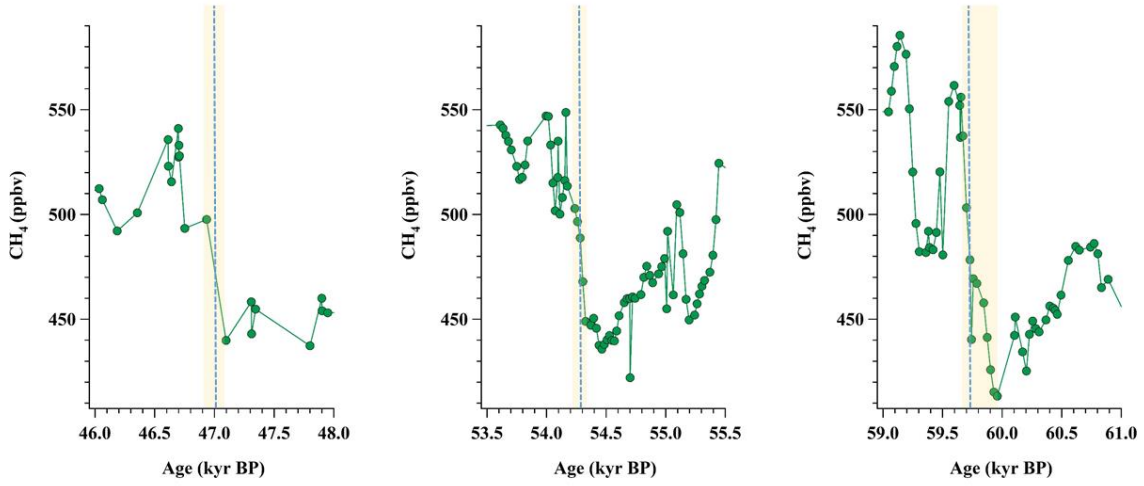


Figure 6.S6. Atmospheric CH₄ records from TALDICE during MIS 3 period. Three boxes show CH₄ jumps at 46.7 ± 0.2 , 54.2 ± 0.1 and 59.7 ± 0.1 kyr BP.

Annex IV

Definition of minima and maxima of atmospheric CO₂ and temperature

A two-steps procedure was used in order to select the maxima and minima of CO₂ concentrations during the last and penultimate glacial periods, and calculate the associated age uncertainty (Figure 6.S6–10 and Table 6.S2). First, inflection points were selected by finding zero values in the second Savitsky–Golay filtered derivative of the data. The parameters of the Savitsky–Golay filters were chosen in order to remove sub–millennial scale variations. We use the same parameters for MIS 3, MIS 5 and 6. Second, a Monte Carlo simulation was conducted, in which the original data were resampled within their uncertainty, and the absolute minima and maxima between pairs of inflection points were selected. This allows us to assign an approximate uncertainty to the timing of each minimum/maximum. The square of the age uncertainty associated with sampling (taken to be the mean sampling resolution) was added to the squared uncertainty calculated in the Monte Carlo procedure to calculate a total uncertainty value.

Table 6.S2. The minima and maxima locations of atmospheric CO₂ during the MIS 6.

	MIS 6 I		MIS 6 II			MIS 6 III			MIS 6 IV			MIS 6 VI			
	Min	Max	Min	Min	Max	Min	Min	Max	Min	Min	Max	Min	Min	Max	Min
Age (kyr BP)	156.9	160.9	162.8	162.8	164.1	167.3	167.3	169.7	173.0	173.0	174.5	177.8	177.8	181.5	185.2
$\pm 2\sigma$ (kyr BP)	0.3	0.3	0.2	0.2	0.3	0.4	0.4	0.2	0.2	0.2	0.2	0.3	0.3	0.2	0.8

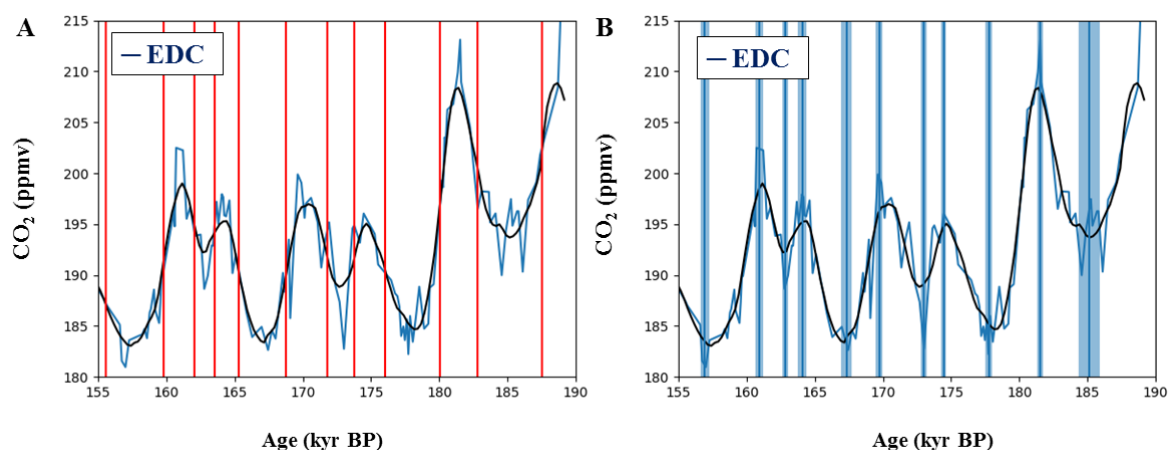


Figure 6.S7. Atmospheric CO₂ records from EDC during MIS 6. The black curve in both panels shows the Savitsky–Golay filtered CO₂ concentration data, and the blue curve shows the original data. (A) Red vertical lines mark inflection points. (B) Blue vertical lines show the minima and maxima of atmospheric CO₂ during MIS 6. The shaded blue bars indicate the timing uncertainty for each minimum/maximum.

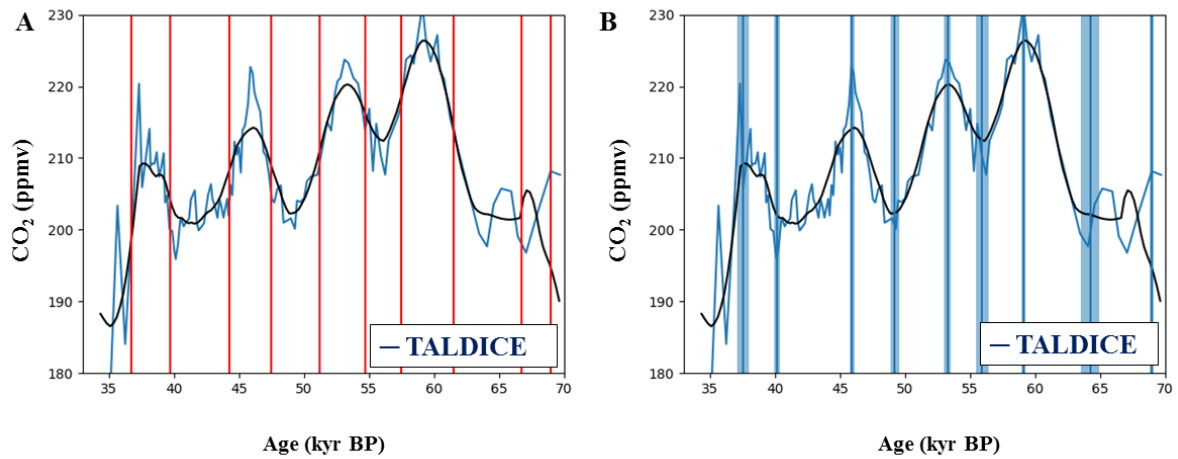


Figure 6.S8. Atmospheric CO₂ records from TALDICE during MIS 3. The black curve in both panels shows the Savitsky-Golay filtered CO₂ concentration data, and the blue curve shows the original data. (A) Red vertical lines mark inflection points. (B) Blue vertical lines show the minima and maxima of atmospheric CO₂ during MIS 3. The shaded blue bars indicate the timing uncertainty for each minimum/maximum.

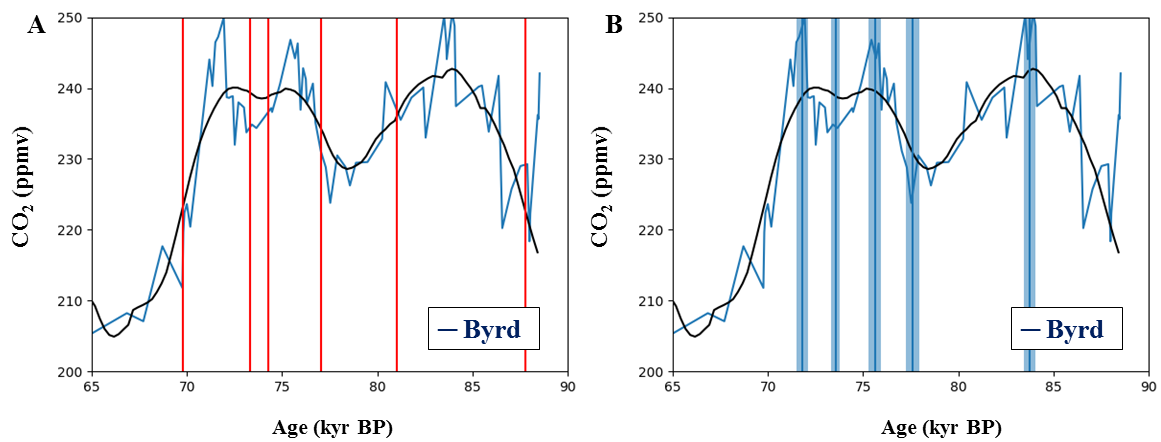


Figure 6.S9. Atmospheric CO₂ records from Byrd during MIS 5. The black curve in both panels shows the Savitsky-Golay filtered CO₂ concentration data, and the blue curve shows the original data. (A) Red vertical lines mark inflection points. (B) Blue vertical lines show the minima and maxima of atmospheric CO₂ during MIS 5. The shaded blue bars indicate the timing uncertainty for each minimum/maximum.

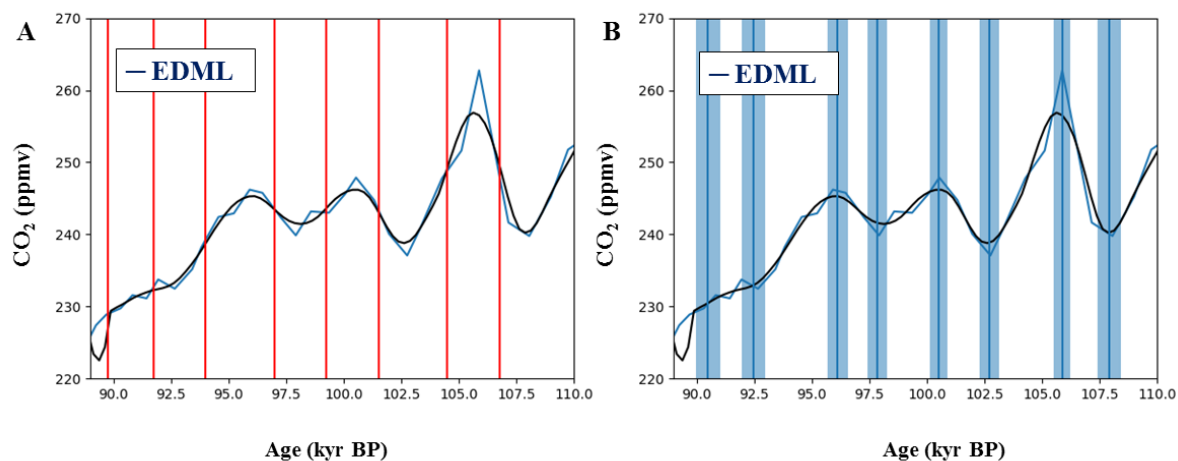


Figure 6.S10. Atmospheric CO₂ records from EDML during MIS 5. The black curve in both panels shows the Savitsky-Golay filtered CO₂ concentration data, and the blue curve shows the original data. (A) Red vertical lines mark inflection points. (B) Blue vertical lines show the minima and maxima of atmospheric CO₂ during MIS 5. The shaded blue bars indicate the timing uncertainty for each minimum/maximum.

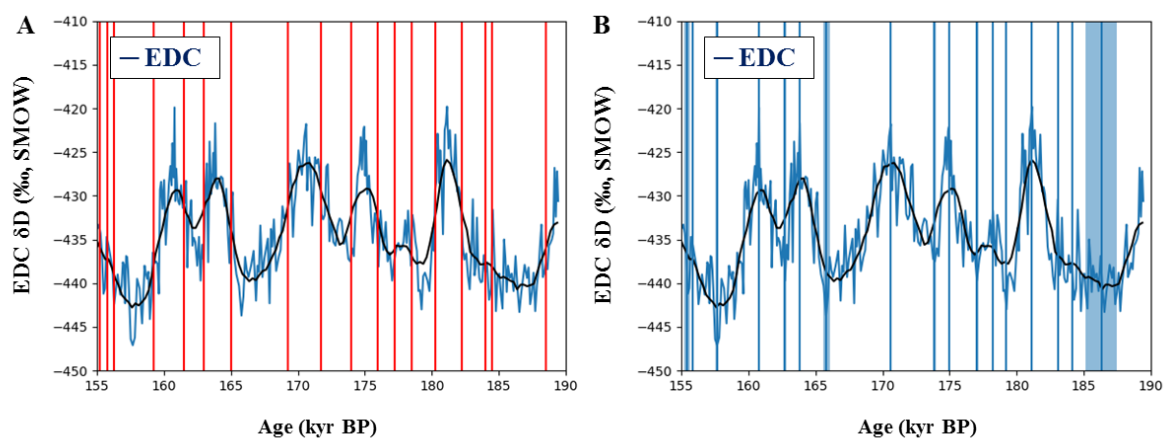


Figure 6.S11. Temperature records from EDC during MIS 6. The black curve in both panels shows the Savitsky-Golay filtered δD series, and the blue curve shows the original data. (A) Red vertical lines mark inflection points. (B) Blue vertical lines show the minima and maxima of δD during MIS 6. The shaded blue bars indicate the timing uncertainty for each minimum/maximum.

Annex V

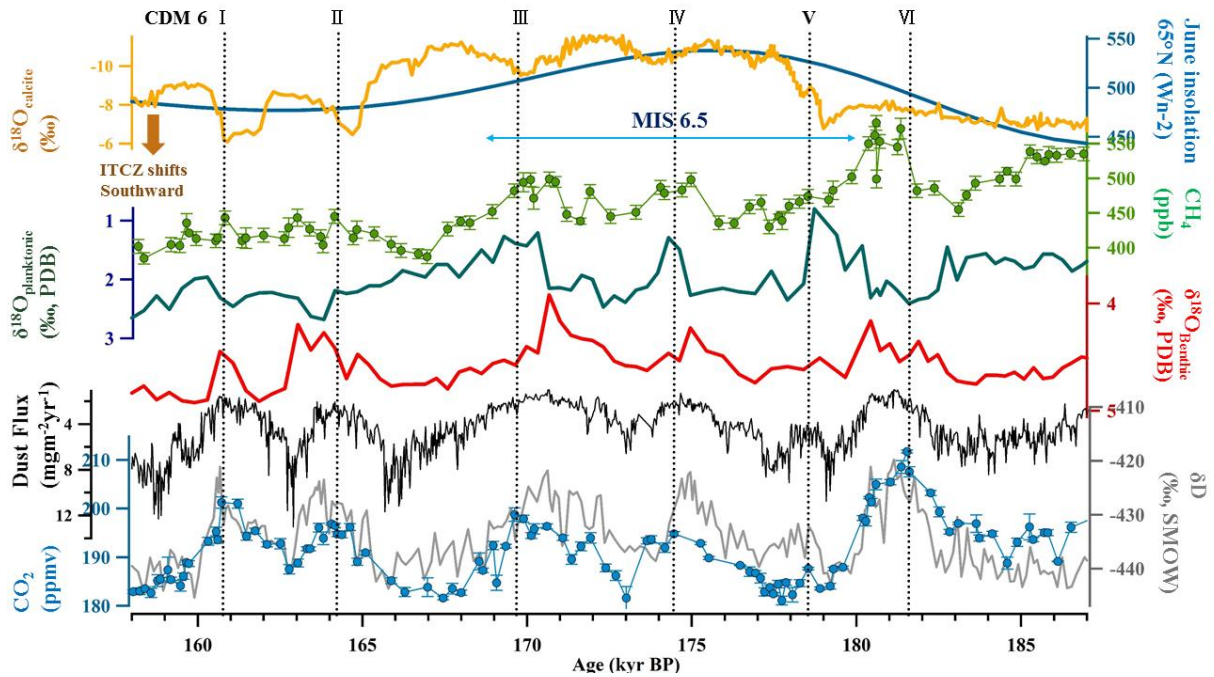


Figure 6.S12. Proxy data during the early MIS 6 period. A: $\delta^{18}\text{O}_{\text{calcite}}$ from Sanbao cave, corresponding with the strength of the East Asian monsoon (Cheng et al., 2016). B: 21 June insolation for 65°N (Berger, 1978). C: $\delta^{18}\text{O}_{\text{planktonic}}$ in the Portuguese Margin (Margari et al., 2010). D: Atmospheric CH_4 in EDC (Loulergue et al., 2008). E: Dust flux in Dome C (Lambert et al., 2012). F: $\delta^{18}\text{O}_{\text{benthic}}$ in the Portuguese Margin (Margari et al., 2010). G: Atmospheric CO_2 in this study. H: δD composition in Dome C, Antarctica (Jouzel et al., 2007). The dotted lines indicate CDM.

References

- Ahn, J., Brook, E.J., 2008. Atmospheric CO₂ and climate on millennial time scales during the last glacial period. *Science* 322, 83-85.
- Ahn, J., Brook, E.J., 2014. Siple Dome ice reveals two modes of millennial CO₂ change during the last ice age. *Nature Communications* 5, 3723.
- Anderson, R., Ali, S., Bradtmiller, L., Nielsen, S., Fleisher, M., Anderson, B., Burckle, L., 2009. Wind-driven upwelling in the Southern Ocean and the deglacial rise in atmospheric CO₂. *science* 323, 1443-1448.
- Ayalon, A., Bar-Matthews, M., Kaufman, A., 2002. Climatic conditions during marine oxygen isotope stage 6 in the eastern Mediterranean region from the isotopic composition of speleothems of Soreq Cave, Israel. *Geology* 30, 303-306.
- Bard, E., Antonioli, F., Silenzi, S., 2002. Sea-level during the penultimate interglacial period based on a submerged stalagmite from Argentarola Cave (Italy). *Earth and Planetary Science Letters* 196, 135-146.
- Bazin, L., Landais, A., Lemieux-Dudon, B., Kele, H.T.M., Veres, D., Parrenin, F., Martinerie, P., Ritz, C., Capron, E., Lipenkov, V., 2013. An optimized multi-proxy, multi-site Antarctic ice and gas orbital chronology (AICC2012): 120-800 ka. *Climate of the Past* 9, 1715-1731.
- Bereiter, B., Lüthi, D., Siegrist, M., Schüpbach, S., Stocker, T.F., Fischer, H., 2012. Mode change of millennial CO₂ variability during the last glacial cycle associated with a bipolar marine carbon seesaw. *Proceedings of the National Academy of Sciences* 109, 9755-9760.
- Bereiter, B., Schwander, J., Lüthi, D., Stocker, T.F., 2009. Change in CO₂ concentration and O₂/N₂ ratio in ice cores due to molecular diffusion. *Geophysical Research Letters* 36.
- Berger, A.L., 1978. Long-Term Variations of Caloric Insolation Resulting from the Earth's Orbital Elements 1. *Quaternary research* 9, 139-167.
- Bouttes, N., Roche, D., Paillard, D., 2011. Systematic study of the fresh water fluxes impact on the carbon cycle. *Climate of the Past Discussions* 7.
- Cheng, H., Edwards, R.L., Sinha, A., Spötl, C., Yi, L., Chen, S., Kelly, M., Kathayat, G., Wang, X., Li, X., 2016. The Asian monsoon over the past 640,000 years and ice age terminations. *Nature* 534, 640.
- Craig, H., Horibe, Y., Sowers, T., 1988. Gravitational separation of gases and isotopes in polar ice caps. *Science* 242, 1675-1678.
- de Abreu, L., Shackleton, N.J., Schönfeld, J., Hall, M., Chapman, M., 2003. Millennial-scale oceanic climate variability off the Western Iberian margin during the last two glacial periods. *Marine Geology* 196, 1-20.

- Dreyfus, G.B., Jouzel, J., Bender, M.L., Landais, A., Masson-Delmotte, V., Leuenberger, M., 2010. Firn processes and $\delta^{15}\text{N}$: potential for a gas-phase climate proxy. *Quaternary Science Reviews* 29, 28-42.
- EPICA Community Members, 2006. One-to-one coupling of glacial climate variability in Greenland and Antarctica. *Nature* 444, 195-198.
- Friedlingstein, P., Cox, P., Betts, R., Bopp, L., von Bloh, W., Brovkin, V., Cadule, P., Doney, S., Eby, M., Fung, I., 2006. Climate-carbon cycle feedback analysis: results from the C⁴MIP model intercomparison. *Journal of climate* 19, 3337-3353.
- Grachev, A.M., Severinghaus, J.P., 2003. Laboratory determination of thermal diffusion constants for $^{29}\text{N}_2/^{28}\text{N}_2$ in air at temperatures from -60 to 0 °C for reconstruction of magnitudes of abrupt climate changes using the ice core fossil-air paleothermometer. *Geochimica et Cosmochimica Acta* 67, 345-360.
- Jouzel, J., Masson-Delmotte, V., Cattani, O., Dreyfus, G., Falourd, S., Hoffmann, G., Minster, B., Nouet, J., Barnola, J.-M., Chappellaz, J., 2007. Orbital and millennial Antarctic climate variability over the past 800,000 years. *science* 317, 793-796.
- Krinner, G., Raynaud, D., Doutriaux, C., Dang, H., 2000. Simulations of the Last Glacial Maximum ice sheet surface climate: Implications for the interpretation of ice core air content. *Journal of Geophysical Research: Atmospheres* 105, 2059-2070.
- Landais, A., Barnola, J.-M., Kawamura, K., Caillon, N., Delmotte, M., Van Ommen, T., Dreyfus, G., Jouzel, J., Masson-Delmotte, V., Minster, B., 2006. Firn-air $\delta^{15}\text{N}$ in modern polar sites and glacial-interglacial ice: a model-data mismatch during glacial periods in Antarctica? *Quaternary science reviews* 25, 49-62.
- Landais, A., Caillon, N., Severinghaus, J., Barnola, J.-M., Goujon, C., Jouzel, J., Masson-Delmotte, V., 2004. Analyse isotopique de l'air piégé dans la glace pour quantifier les variations de température. *Comptes Rendus Geoscience* 336, 963-970.
- Landais, A., Dreyfus, G., Capron, E., Jouzel, J., Masson-Delmotte, V., Roche, D., Prié, F., Caillon, N., Chappellaz, J., Leuenberger, M., 2013. Two-phase change in CO₂, Antarctic temperature and global climate during Termination II. *Nature geoscience* 6, 1062.
- Loulergue, L., Schilt, A., Spahni, R., Masson-Delmotte, V., Blunier, T., Lemieux, B., Barnola, J.-M., Raynaud, D., Stocker, T.F., Chappellaz, J., 2008. Orbital and millennial-scale features of atmospheric CH₄ over the past 800,000 years. *Nature* 453, 383.
- Margari, V., Skinner, L., Tzedakis, P., Ganopolski, A., Vautravers, M., Shackleton, N., 2010. The nature of millennial-scale climate variability during the past two glacial periods. *Nature Geoscience* 3, 127.
- Margari, V., Skinner, L.C., Hodell, D.A., Martrat, B., Toucanne, S., Grimalt, J.O., Gibbard, P.L., Lunkka, J., Tzedakis, P., 2014. Land-ocean changes on orbital and millennial time scales and the penultimate glaciation. *Geology* 42, 183-186.

- Mélières, M.A., Rossignol-Strick, M., Malaizé, B., 1997. Relation between low latitude insolation and $\delta^{18}\text{O}$ change of atmospheric oxygen for the last 200 kyrs, as revealed by Mediterranean sapropels. *Geophysical Research Letters* 24, 1235-1238.
- Menviel, L., England, M.H., Meissner, K., Mouchet, A., Yu, J., 2014. Atlantic-Pacific seesaw and its role in outgassing CO_2 during Heinrich events. *Paleoceanography* 29, 58-70.
- Menviel, L., Timmermann, A., Mouchet, A., Timm, O., 2008. Meridional reorganizations of marine and terrestrial productivity during Heinrich events. *Paleoceanography* 23.
- Parrenin, F., Barker, S., Blunier, T., Chappellaz, J., Jouzel, J., Landais, A., Masson-Delmotte, V., Schwander, J., Veres, D., 2012. On the gas-ice depth difference (Delta depth) along the EPICA Dome C ice core. *Climate of the Past* 8, 1239-1255.
- Parrenin, F., Barnola, J.-M., Beer, J., Blunier, T., Castellano, E., Chappellaz, J., Dreyfus, G., Fischer, H., Fujita, S., Jouzel, J., 2007. The EDC3 chronology for the EPICA Dome C ice core. *Climate of the Past* 3, 485-497.
- Parrenin, F., Masson-Delmotte, V., Köhler, P., Raynaud, D., Paillard, D., Schwander, J., Barbante, C., Landais, A., Wegner, A., Jouzel, J., 2013. Synchronous change of atmospheric CO_2 and Antarctic temperature during the last deglacial warming. *Science* 339, 1060-1063.
- Petit, J.-R., Jouzel, J., Raynaud, D., Barkov, N.I., Barnola, J.-M., Basile, I., Bender, M., Chappellaz, J., Davis, M., Delaygue, G., 1999. Climate and atmospheric history of the past 420,000 years from the Vostok ice core, Antarctica. *Nature* 399, 429.
- Schaefer, H., Laurantou, A., Chappellaz, J., Lüthi, D., Bereiter, B., Barnola, J.-M., 2011. On the suitability of partially clathrated ice for analysis of concentration and $\delta^{13}\text{C}$ of palaeo-atmospheric CO_2 . *Earth and planetary science letters* 307, 334-340.
- Schmittner, A., Brook, E.J., Ahn, J., 2007. Impact of the ocean's overturning circulation on atmospheric CO_2 , *Ocean Circulation: Mechanisms and Impacts*, AGU Geophysical Monograph Series, pp. 209-246.
- Schmittner, A., Galbraith, E.D., 2008. Glacial greenhouse-gas fluctuations controlled by ocean circulation changes. *Nature* 456, 373.
- Shackleton, N.J., Hall, M.A., Vincent, E., 2000. Phase relationships between millennial-scale events 64,000–24,000 years ago. *Paleoceanography* 15, 565-569.
- Sowers, T., Bender, M., Raynaud, D., 1989. Elemental and isotopic composition of occluded O_2 and N_2 in polar ice. *Journal of Geophysical Research: Atmospheres* 94, 5137-5150.
- Sowers, T., Bender, M., Raynaud, D., Korotkevich, Y.S., 1992. $\delta^{15}\text{N}$ of N_2 in air trapped in polar ice: A tracer of gas transport in the firn and a possible constraint on ice age-gas age differences. *Journal of Geophysical Research: Atmospheres* 97, 15683-15697.
- Stocker, T.F., Johnsen, S.J., 2003. A minimum thermodynamic model for the bipolar seesaw. *Paleoceanography* 18.

Wilson, D.J., Piotrowski, A.M., Galy, A., Banakar, V.K., 2015. Interhemispheric controls on deep ocean circulation and carbon chemistry during the last two glacial cycles. *Paleoceanography* 30, 621-641.

Chapter 7

Conclusions and future plans

The main purpose of this thesis consists of measuring atmospheric CO₂ variations during the penultimate glacial period (or Marine Isotope Stage 6, MIS 6) on millennial time scales, and answering two main questions: How are climate variations on millennial time scale related to atmospheric CO₂ during MIS 6? Are there similarities/differences in atmospheric CO₂ variations on millennial time scale during the past two glacial periods?

To this end, during the first year of PhD, improvement of the existing ice crushing system (the ball mill) at IGE was conducted, reaching an unprecedented precision of 1 ppm (1 σ). This represents, up to today, one of the best performances for CO₂ measurement in ice cores. Three main problems of the existing ball mill system were identified: 1) the previous published data were not corrected for CO₂ contamination, which require regular calibration with standard gases. 2) Powdery ice was possibly introduced in the warm part of the sampling line causing a bias on the retrieved CO₂ concentration by the GC. The problem was solved by placing a filter on the line. 3) The original measurement procedure only allowed a throughput of two samples per day. Today, 3-4 samples per day can be measured.

Even though the analytical system provides 1 ppmv of precision, the accuracy is affected by other parameters, such as ice core quality and handling during the sample preparation. To improve the accuracy of the measurement, replicates from the same depth interval are essential. However, the number of replicates is practically limited by the large sample size required for the ball mill system (40 g), the limited ice samples available, as well as the time required for performing them.

The ball mill system provides an extraction efficiency which is not ideal for clathrate ice samples. Because of gas fractionation during the clathrate formation, the measurements of CO₂ in a Bubble–Clathrate Transformation Zone (BTCZ) may be affected by the efficiency of the extraction technique. A maximization of the latter would lead to a minimization of the possible biases, therefore to a better accuracy for reconstructing atmospheric CO₂ variations in the BTCZ. For overcoming this limitation, the ice sample should be crushed into the finest powder. A new crushing method, the ring system, was therefore developed aiming to a better the extraction efficiency.

The new system crushes samples of 20-40 g in 5 sec by horizontally rotating a chamber containing metallic concentric rings. The ice samples are crushed into finer powders than using the ball

system. However, the ring system still cannot extract 100% of the air from clathrate ice. The precision of the ring mill system is ~ 2 ppmv on average, and this precision also evolves over time due to a degradation of the crushing cell. Thus, further improvements are required in the future aiming a better precision and stability of the system. Using larger samples to reconstruct CO₂ concentrations should be considered. In this case, fewer replicates can be made, but inaccuracies related to contamination in the ice core can be minimized. In this thesis, due to the limited number of measurements, the accuracy of the new system could not be verified. Finally, the 10 kg crushing cell of the ring system is difficult to handle.

Additional measurements on the TALDICE ice core will be required to continue improving the ring system. For better understanding the accuracy of the measurement on clathrate ice, clathrate/bubble counting should be conducted on the samples and compared with CO₂ data.

In the second part of this PhD thesis, atmospheric CO₂ during the MIS 6 period was reconstructed using the improved ball mill system. CO₂ data from 150 depth intervals of EDC were reconstructed. We found one minor and five major variations during the early MIS 6 period (185-160 kyr BP). These variabilities are highly matched with Antarctic temperature during the MIS 6 period. During the short stadial in the North Atlantic, atmospheric CO₂ variations on multi-millennial timescales are negligible and atmospheric CO₂ and temperature variabilities in EDC appear decoupled. During this period, the strength of upwelling in the Southern Ocean might not have been sufficient to impact on atmospheric CO₂. In addition, two modes of CO₂ variations are present in the MIS 6 period. CDM 6 lags abrupt warming in the Northern Hemisphere by only 100 ± 360 yrs, while the lags for CDM 3 and 4 are much longer, on average $1,100 \pm 280$ yrs. These two modes might be related with a change of the AMOC between the earliest MIS 6 and the MIS 6e. These two phenomena are also observed during the last glacial period.

In this study, ice age was revised by estimating Δ depth from $\delta^{15}\text{N}$ in air of ice core due to similar age uncertainties of ice and air age of EDC. However, changing the ice chronology instead of the gas chronology is affected by the coherency of the ice core chronology with respect to the thinning function, to the history of accumulation rate, to the link with other dating constraints (Bazin et al., 2013). However, our main conclusion related with the phasing between water isotopes and CO₂ changes, this different approach are not affected. Regarding the relationship between CO₂ and NH warmings, CH₄ is used as a NH warming tracer. CO₂ and CH₄ are recorded in the same bubbles. Thus there is absolutely no effect of the chronology being used. Age revision will be conducted to improve the relative age scales between gas and ice.

References

- Ahn, J., Brook, E.J., 2008. Atmospheric CO₂ and climate on millennial time scales during the last glacial period. *Science* 322, 83-85.
- Ahn, J., Brook, E.J., Howell, K., 2009. A high-precision method for measurement of paleoatmospheric CO₂ in small polar ice samples. *Journal of Glaciology* 55, 499-506.
- Ahn, J., Brook, E.J., 2014. Siple Dome ice reveals two modes of millennial CO₂ change during the last ice age. *Nature Communications* 5, 3723.
- Anklin, M., BARNOLA, J.M., Schwander, J., Stauffer, B., Raynaud, D., 1995. Processes affecting the CO₂ concentrations measured in Greenland ice. *Tellus B* 47, 461-470.
- Arnaud, L., 1997. Modélisation de la transformation de la neige en glace à la surface des calottes polaires: étude du transport des gaz dans ces milieux poreux. Université Joseph-Fourier-Grenoble I.
- Barnola, J.-M., 1984. Etude des variations passées du CO₂ atmosphérique à partir de l'analyse de l'air piégé dans la glace: détermination du niveau pré-industriel, description de la transition âge glaciaire-holocène. Université Scientifique et Médicale de Grenoble.
- Barnola, J., Anklin, M., Porcheron, J., Raynaud, D., Schwander, J., Stauffer, B., 1995. CO₂ evolution during the last millennium as recorded by Antarctic and Greenland ice. *Tellus B: Chemical and Physical Meteorology* 47, 264-272.
- Barnola, J., Raynaud, D., Neftel, A., Oeschger, H., 1983. Comparison of CO₂ measurements by two laboratories on air from bubbles in polar ice. *Nature* 303, 410.
- Bellier, B., 2004. Etude des variations du cycle du carbone au cours de l'Holocène à partir de l'analyse couplée CO₂-CH₄ piégés dans les glaces polaires. Université Joseph-Fourier-Grenoble I.
- Bender, M., Sowers, T., Brook, E., 1997. Gases in ice cores. *Proceedings of the National Academy of Sciences* 94, 8343-8349.
- Bereiter, B., Schwander, J., Lüthi, D., Stocker, T.F., 2009. Change in CO₂ concentration and O₂/N₂ ratio in ice cores due to molecular diffusion. *Geophysical Research Letters* 36.
- Bereiter, B., 2012. Atmospheric CO₂ Reconstructions using Polar Ice Cores: Development of a New Dry Extraction Device and Insights from Highly Resolved Records. Universität Bern.
- Bereiter, B., Lüthi, D., Siegrist, M., Schüpbach, S., Stocker, T.F., Fischer, H., 2012. Mode change of millennial CO₂ variability during the last glacial cycle associated with a bipolar marine carbon seesaw. *Proceedings of the National Academy of Sciences* 109, 9755-9760.
- Bereiter, B., Stocker, T., Fischer, H., 2013. A centrifugal ice microtome for measurements of atmospheric CO₂ on air trapped in polar ice cores. *Atmospheric Measurement Techniques (AMT)* 6, 251-262.

- Blunier, T., Spahni, R., Barnola, J.-M., Chappellaz, J., Louergue, L., Schwander, J., 2007. Synchronization of ice core records via atmospheric gases. *Climate of the Past Discussions* 3, 365-381.
- Bock, M., Schmitt, J., Möller, L., Spahni, R., Blunier, T., Fischer, H., 2010. Hydrogen isotopes preclude marine hydrate CH₄ emissions at the onset of Dansgaard-Oeschger events. *Science* 328, 1686-1689.
- Bouttes, N., Roche, D., Paillard, D., 2011. Systematic study of the fresh water fluxes impact on the carbon cycle. *Climate of the Past Discussions* 7.
- Broecker, W.S., 1998. Paleocean circulation during the last deglaciation: a bipolar seesaw? *Paleoceanography* 13, 119-121.
- Buizert, C., Martinerie, P., Petrenko, V., Severinghaus, J., Trudinger, C., Witrant, E., Rosen, J., Orsi, A., Rubino, M., Etheridge, D., 2012. Gas transport in firn: multiple-tracer characterisation and model intercomparison for NEEM, Northern Greenland. *Atmospheric Chemistry and Physics* 12, 4259-4277.
- Campen, R.K., Sowers, T., Alley, R.B., 2003. Evidence of microbial consortia metabolizing within a low-latitude mountain glacier. *Geology* 31, 231-234.
- Capron, E., Landais, A., Lemieux-Dudon, B., Schilt, A., Masson-Delmotte, V., Buiron, D., Chappellaz, J., Dahl-Jensen, D., Johnsen, S., Leuenberger, M., 2010. Synchronising EDML and NorthGRIP ice cores using $\delta^{18}\text{O}$ of atmospheric oxygen ($\delta^{18}\text{O}_{\text{atm}}$) and CH₄ measurements over MIS5 (80–123 kyr). *Quaternary Science Reviews* 29, 222-234.
- Chae, N., 2011. Annual variation of soil respiration and precipitation in a temperate forest (*Quercus serrata* and *Carpinus laxiflora*) under East Asian monsoon climate. *Journal of Plant Biology* 54, 101-111.
- Clarke, G.K., Waddington, E.D., 1991. A three-dimensional theory of wind pumping. *Journal of Glaciology* 37, 89-96.
- Craig, H., Horibe, Y., Sowers, T., 1988. Gravitational separation of gases and isotopes in polar ice caps. *Science* 242, 1675-1678.
- Davidson, E.A., Verchot, L.V., Cattanio, J.H., Ackerman, I.L., Carvalho, J., 2000. Effects of soil water content on soil respiration in forests and cattle pastures of eastern Amazonia. *Biogeochemistry* 48, 53-69.
- Delmas, R.J., Ascencio, J.-M., Legrand, M., 1980. Polar ice evidence that atmospheric CO₂ 20,000 yr BP was 50% of present. *Nature* 284, 155.
- Dreyfus, G.B., Jouzel, J., Bender, M.L., Landais, A., Masson-Delmotte, V., Leuenberger, M., 2010. Firn processes and $\delta^{15}\text{N}$: potential for a gas-phase climate proxy. *Quaternary Science Reviews* 29, 28-42.
- Dunbar, N.W., Kurbatov, A.V., 2011. Tephrochronology of the Siple Dome ice core, West Antarctica: correlations and sources. *Quaternary Science Reviews* 30, 1602-1614.

- Eggleston, S., 2015. Reconstructions of atmospheric [CO₂] and δ¹³C from Antarctic ice cores over the last glacial cycle. Universität Bern.
- Eggleston, S., Schmitt, J., Bereiter, B., Schneider, R., Fischer, H., 2016. Evolution of the stable carbon isotope composition of atmospheric CO₂ over the last glacial cycle. *Paleoceanography* 31, 434-452.
- Etheridge, D., Pearman, G., De Silva, F., 1988. Atmospheric trace-gas variations as revealed by air trapped in an ice core from Law Dome, Antarctica. *Annals of Glaciology* 10, 28-33.
- Etheridge, D.M., Steele, L., Langenfelds, R., Francey, R., Barnola, J.M., Morgan, V., 1996. Natural and anthropogenic changes in atmospheric CO₂ over the last 1000 years from air in Antarctic ice and firn. *Journal of Geophysical Research: Atmospheres* 101, 4115-4128.
- Ferrari, R., Jansen, M.F., Adkins, J.F., Burke, A., Stewart, A.L., Thompson, A.F., 2014. Antarctic sea ice control on ocean circulation in present and glacial climates. *Proceedings of the National Academy of Sciences*, 201323922.
- Fischer, H., Wahlen, M., Smith, J., Mastroianni, D., Deck, B., 1999. Ice core records of atmospheric CO₂ around the last three glacial terminations. *Science* 283, 1712-1714.
- Fischer, H., Schmitt, J., Lüthi, D., Stocker, T.F., Tschumi, T., Parekh, P., Joos, F., Köhler, P., Völker, C., Gersonde, R., 2010. The role of Southern Ocean processes in orbital and millennial CO₂ variations—A synthesis. *Quaternary Science Reviews* 29, 193-205.
- Fourteau, K., Faïn, X., Martinerie, P., Landais, A., Ekaykin, A.A., Lipenkov, V.Y., Chappellaz, J., 2017. Analytical constraints on layered gas trapping and smoothing of atmospheric variability in ice under low-accumulation conditions. *Climate of the Past* 13, 1815-1830.
- Frezzotti, M., Bitelli, G., De Michelis, P., Deponti, A., Forieri, A., Gandolfi, S., Maggi, V., Mancini, F., Remy, F., Tabacco, I.E., 2004. Geophysical survey at Talos Dome, East Antarctica: the search for a new deep-drilling site. *Annals of Glaciology* 39, 423-432.
- Friedlingstein, P., Cox, P., Betts, R., Bopp, L., von Bloh, W., Brovkin, V., Cadule, P., Doney, S., Eby, M., Fung, I., 2006. Climate–carbon cycle feedback analysis: results from the C⁴MIP model intercomparison. *Journal of climate* 19, 3337-3353.
- Grachev, A.M., Severinghaus, J.P., 2003. Laboratory determination of thermal diffusion constants for ²⁹N₂/²⁸N₂ in air at temperatures from – 60 to 0 °C for reconstruction of magnitudes of abrupt climate changes using the ice core fossil–air paleothermometer. *Geochimica et Cosmochimica Acta* 67, 345-360.
- Hain, M., Sigman, D., Haug, G., 2014. The biological Pump in the Past. Reference Module in Earth Systems and Environmental Sciences, *Treatise on Geochemistry (Second Edition), The Oceans and Marine Geochemistry* 8, 485-517.
- Hillenbrand, C.-D., Cortese, G., 2006. Polar stratification: a critical view from the Southern Ocean. *Palaeogeography, Palaeoclimatology, Palaeoecology* 242, 240-252.
- Holmen, K., 1992. *The Global Carbon Cycle*, International Geophysics. Elsevier, pp. 239-262.

- Indermühle, A., Stocker, T.F., Joos, F., Fischer, H., Smith, H.J., Wahlen, M., Deck, B., Mastroianni, D., Tschumi, J., Blunier, T., 1999. Holocene carbon-cycle dynamics based on CO₂ trapped in ice at Taylor Dome, Antarctica. *Nature* 398, 121.
- IPCC, 2007. Climate change 2007: the physical science basis. Contribution of Working Group I to the Fourth Assessment Report of the Intergovernmental Panel on Climate Change, 2007, in: Solomon, S., Qin, D., Manning, M., Chen, Z., Marquis, M., Averyt, K., Tignor, M., Miller, H. (Eds.).
- Jouzel, J., Masson-Delmotte, V., Cattani, O., Dreyfus, G., Falourd, S., Hoffmann, G., Minster, B., Nouet, J., Barnola, J.-M., Chappellaz, J., 2007. Orbital and millennial Antarctic climate variability over the past 800,000 years. *science* 317, 793-796.
- Kaspers, K., Van de Wal, R., Van den Broeke, M., Schwander, J., Van Lipzig, N., Brenninkmeijer, C., 2004. Model calculations of the age of firn air across the Antarctic continent. *Atmospheric Chemistry and Physics* 4, 1365-1380.
- Kawamura, K., Nakazawa, T., Aoki, S., Sugawara, S., Fujii, Y., Watanabe, O., 2003. Atmospheric CO₂ variations over the last three glacial/interglacial climatic cycles deduced from the Dome Fuji deep ice core, Antarctica using a wet extraction technique. *Tellus B: Chemical and Physical Meteorology* 55, 126-137.
- Kawamura, K., Severinghaus, J.P., Ishidoya, S., Sugawara, S., Hashida, G., Motoyama, H., Fujii, Y., Aoki, S., Nakazawa, T., 2006. Convective mixing of air in firn at four polar sites. *Earth and Planetary Science Letters* 244, 672-682.
- Keeling, C.D., 1960. The concentration and isotopic abundances of carbon dioxide in the atmosphere. *Tellus* 12, 200-203.
- Kim, D.-G., Mu, S., Kang, S., Lee, D., 2010. Factors controlling soil CO₂ effluxes and the effects of rewetting on effluxes in adjacent deciduous, coniferous, and mixed forests in Korea. *Soil Biology and Biochemistry* 42, 576-585.
- Kobashi, T., Severinghaus, J.P., Kawamura, K., 2008. Argon and nitrogen isotopes of trapped air in the GISP2 ice core during the Holocene epoch (0–11,500 BP): methodology and implications for gas loss processes. *Geochimica et Cosmochimica Acta* 72, 4675-4686.
- Köhler, P., Knorr, G., Bard, E., 2014. Permafrost thawing as a possible source of abrupt carbon release at the onset of the Bølling/Allerød. *Nature communications* 5, 5520.
- Kuhlbrodt, T., Griesel, A., Montoya, M., Levermann, A., Hofmann, M., Rahmstorf, S., 2007. On the driving processes of the Atlantic meridional overturning circulation. *Reviews of Geophysics* 45.
- Lacis, A.A., Schmidt, G.A., Rind, D., Ruedy, R.A., 2010. Atmospheric CO₂: Principal control knob governing Earth's temperature. *Science* 330, 356-359.
- Landais, A., Barnola, J.-M., Kawamura, K., Caillon, N., Delmotte, M., Van Ommen, T., Dreyfus, G., Jouzel, J., Masson-Delmotte, V., Minster, B., 2006. Firn-air δ¹⁵N in modern polar sites and

- glacial–interglacial ice: a model-data mismatch during glacial periods in Antarctica? *Quaternary science reviews* 25, 49-62.
- Landais, A., Dreyfus, G., Capron, E., Pol, E., Loutre, M.-F., Raynaud, D., Lipenkov, V.Y., Arnaud, L., Masson-Delmotte, V., Paillard, D., 2012. Towards orbital dating of the EPICA Dome C ice core using $\delta\text{O}_2/\text{N}_2$. *Climate of the Past* 8, 191-203.
- Landais, A., Dreyfus, G., Capron, E., Jouzel, J., Masson-Delmotte, V., Roche, D., Prié, F., Caillon, N., Chappellaz, J., Leuenberger, M., 2013. Two-phase change in CO_2 , Antarctic temperature and global climate during Termination II. *Nature geoscience* 6, 1062.
- Le Quéré, C., Andres, R.J., Boden, T., Conway, T., Houghton, R.A., House, J.I., Marland, G., Peters, G.P., Van der Werf, G., Ahlström, A., 2012. The global carbon budget 1959–2011. *Earth System Science Data Discussions* 5, 1107-1157.
- Lipenkov, V.Y., 2000. Air bubbles and air-hydrate crystals in the Vostok ice core, *Physics of ice core records*. Hokkaido University Press, pp. 327-358.
- Lorius, C., Jouzel, J., Raynaud, D., Hansen, J., Le Treut, H., 1990. The ice-core record: climate sensitivity and future greenhouse warming. *Nature* 347, 139.
- Louergue, L., Schilt, A., Spahni, R., Masson-Delmotte, V., Blunier, T., Lemieux, B., Barnola, J.-M., Raynaud, D., Stocker, T.F., Chappellaz, J., 2008. Orbital and millennial-scale features of atmospheric CH_4 over the past 800,000 years. *Nature* 453, 383.
- Lourantou, A., 2008. Constraints on the carbon dioxide (CO_2) deglacial rise based on its stable carbon isotopic ratio ($\delta^{13}\text{CO}_2$). *Université Joseph-Fourier-Grenoble I*.
- Lourantou, A., Chappellaz, J., Barnola, J.-M., Masson-Delmotte, V., Raynaud, D., 2010a. Changes in atmospheric CO_2 and its carbon isotopic ratio during the penultimate deglaciation. *Quaternary Science Reviews* 29, 1983-1992.
- Lüthi, D., Le Floch, M., Bereiter, B., Blunier, T., Barnola, J.-M., Siegenthaler, U., Raynaud, D., Jouzel, J., Fischer, H., Kawamura, K., 2008. High-resolution carbon dioxide concentration record 650,000–800,000 years before present. *Nature* 453, 379.
- Lüthi, D., Bereiter, B., Stauffer, B., Winkler, R., Schwander, J., Kindler, P., Leuenberger, M., Kipfstuhl, S., Capron, E., Landais, A., 2010. CO_2 and O_2/N_2 variations in and just below the bubble–clathrate transformation zone of Antarctic ice cores. *Earth and planetary science letters* 297, 226-233.
- Marcott, S.A., Bauska, T.K., Buizert, C., Steig, E.J., Rosen, J.L., Cuffey, K.M., Fudge, T., Severinghaus, J.P., Ahn, J., Kalk, M.L., 2014. Centennial-scale changes in the global carbon cycle during the last deglaciation. *Nature* 514, 616.
- Marinov, I., Gnanadesikan, A., Sarmiento, J.L., Toggweiler, J., Follows, M., Mignone, B., 2008. Impact of oceanic circulation on biological carbon storage in the ocean and atmospheric pCO_2 . *Global Biogeochemical Cycles* 22.

- Mariotti, A., 1983. Atmospheric nitrogen is a reliable standard for natural ^{15}N abundance measurements. *Nature* 303, 685.
- Martin, J.H., 1990. Glacial-interglacial CO_2 change: The iron hypothesis. *Paleoceanography* 5, 1-13.
- Martínez-García, A., Rosell-Melé, A., Geibert, W., Gersonde, R., Masqué, P., Gaspari, V., Barbante, C., 2009. Links between iron supply, marine productivity, sea surface temperature, and CO_2 over the last 1.1 Ma. *Paleoceanography* 24.
- Menviel, L., Timmermann, A., Mouchet, A., Timm, O., 2008. Meridional reorganizations of marine and terrestrial productivity during Heinrich events. *Paleoceanography* 23.
- Menviel, L., England, M.H., Meissner, K., Mouchet, A., Yu, J., 2014. Atlantic-Pacific seesaw and its role in outgassing CO_2 during Heinrich events. *Paleoceanography* 29, 58-70.
- Mielnick, P., Dugas, W.A., 2000. Soil CO_2 flux in a tallgrass prairie. *Soil Biology and Biochemistry* 32, 221-228.
- Monnin, E., Indermühle, A., Dällenbach, A., Flückiger, J., Stauffer, B., Stocker, T.F., Raynaud, D., Barnola, J.-M., 2001. Atmospheric CO_2 concentrations over the last glacial termination. *Science* 291, 112-114.
- Nakazawa, T., Machida, T., Esumi, K., Tanaka, M., Fujii, Y., Aoki, S., Watanabe, O., 1993. Measurements of CO_2 and CH_4 concentrations in air in a polar ice core. *Journal of Glaciology* 39, 209-215.
- Neff, P.D., 2014. A review of the brittle ice zone in polar ice cores. *Annals of Glaciology* 55, 72-82.
- Neftel, A., Oeschger, H., Schwander, J., Stauffer, B., Zumbunn, R., 1982. Ice core sample measurements give atmospheric CO_2 content during the past 40,000 yr. *Nature* 295, 220.
- Neftel, A., Oeschger, H., Schwander, J., Stauffer, B., 1983. Carbon dioxide concentration in bubbles of natural cold ice. *The Journal of Physical Chemistry* 87, 4116-4120.
- Nehrbass-Ahles, C., 2017. Millennial-scale atmospheric CO_2 reconstructions using multiple Antarctic ice cores. Universität Bern.
- Oeschger, H., Neftel, A., Staffelbach, T., Stauffer, B., 1988. The dilemma of the rapid variations in CO_2 in Greenland ice cores. *Annals of Glaciology* 10, 215-216.
- Ohno, H., Lipenkov, V.Y., Hondoh, T., 2004. Air bubble to clathrate hydrate transformation in polar ice sheets: a reconsideration based on the new data from Dome Fuji ice core. *Geophysical research letters* 31.
- Ohno, H., Lipenkov, V.Y., Hondoh, T., 2010. Formation of air clathrate hydrates in polar ice sheets: heterogeneous nucleation induced by micro-inclusions. *Journal of Glaciology* 56, 917-921.
- Parrenin, F., Barker, S., Blunier, T., Chappellaz, J., Jouzel, J., Landais, A., Masson-Delmotte, V., Schwander, J., Veres, D., 2012. On the gas-ice depth difference (Delta depth) along the EPICA Dome C ice core. *Climate of the Past* 8, 1239-1255.

- Pepin, L., 2000. Variations de la teneur en CO₂ de l'atmosphère au cours des 4 derniers cycles glaciaire-interglaciaires, à partir de l'analyse de la carotte de Vostok (Antarctique): implications sur l'évolution du climat et du cycle du carbone. Université Joseph-Fourier-Grenoble I.
- Petit, J.-R., Jouzel, J., Raynaud, D., Barkov, N.I., Barnola, J.-M., Basile, I., Bender, M., Chappellaz, J., Davis, M., Delaygue, G., 1999. Climate and atmospheric history of the past 420,000 years from the Vostok ice core, Antarctica. *Nature* 399, 429.
- Rahmstorf, S., 2002. Ocean circulation and climate during the past 120,000 years. *Nature* 419, 207.
- Royer, D.L., Berner, R.A., Beerling, D.J., 2001. Phanerozoic atmospheric CO₂ change: evaluating geochemical and paleobiological approaches. *Earth-Science Reviews* 54, 349-392.
- Salamatin, A.N., Lipenkov, V.Y., Ikeda-Fukazawa, T., Hondoh, T., 2001. Kinetics of air-hydrate nucleation in polar ice sheets. *Journal of crystal growth* 223, 285-305.
- Schaefer, H., Lourantou, A., Chappellaz, J., Lüthi, D., Bereiter, B., Barnola, J.-M., 2011. On the suitability of partially clathrated ice for analysis of concentration and $\delta^{13}\text{C}$ of palaeo-atmospheric CO₂. *Earth and planetary science letters* 307, 334-340.
- Schilt, A., Baumgartner, M., Schwander, J., Buiron, D., Capron, E., Chappellaz, J., Loulergue, L., Schüpbach, S., Spahni, R., Fischer, H., 2010. Atmospheric nitrous oxide during the last 140,000 years. *Earth and Planetary Science Letters* 300, 33-43.
- Schmitt, J., Schneider, R., Fischer, H., 2011. A sublimation technique for high-precision measurements of $\delta^{13}\text{CO}_2$ and mixing ratios of CO₂ and N₂O from air trapped in ice cores. *Atmospheric Measurement Techniques* 4, 1445-1461.
- Schmittner, A., Galbraith, E.D., 2008. Glacial greenhouse-gas fluctuations controlled by ocean circulation changes. *Nature* 456, 373.
- Schmittner, A., 2005. Decline of the marine ecosystem caused by a reduction in the Atlantic overturning circulation. *Nature* 434, 628.
- Schmittner, A., Brook, E.J., Ahn, J., 2007. Impact of the ocean's overturning circulation on atmospheric CO₂, *Ocean Circulation: Mechanisms and Impacts*, AGU Geophysical Monograph Series, pp. 209-246.
- Schneider, R., 2011. Quantifying past changes of the global carbon cycle based on d^{13}CO_2 measurements in Antarctic ice cores. PhD Thesis, University of Bern.
- Schwander, J., Stauffer, B., 1984. Age difference between polar ice and the air trapped in its bubbles. *Nature* 311, 45.
- Schwander, J., 1989. The transformation of snow to ice and the occlusion of gases, *The Environmental Record in Glaciers and Ice Sheets* H. Oeschger, CC Langway, 53-67. John Wiley, New York.
- Schwander, J., 1996. Gas diffusion in firn, *Chemical exchange between the atmosphere and polar snow*. Springer, pp. 527-540.
- Schwander, J., Jouzel, J., Hammer, C.U., Petit, J.R., Udisti, R., Wolff, E., 2001. A tentative chronology for the EPICA Dome Concordia ice core. *Geophysical research letters* 28, 4243-4246.

- Severinghaus, J.P., Grachev, A., Battle, M., 2001. Thermal fractionation of air in polar firm by seasonal temperature gradients. *Geochemistry, Geophysics, Geosystems* 2.
- Severinghaus, J.P., Albert, M.R., Courville, Z.R., Fahnstock, M.A., Kawamura, K., Montzka, S.A., Mühle, J., Scambos, T.A., Shields, E., Shuman, C.A., 2010. Deep air convection in the firm at a zero-accumulation site, central Antarctica. *Earth and Planetary science letters* 293, 359-367.
- Siegenthaler, U., Stocker, T.F., Monnin, E., Lüthi, D., Schwander, J., Stauffer, B., Raynaud, D., Barnola, J.-M., Fischer, H., Masson-Delmotte, V., 2005. Stable carbon cycle–climate relationship during the late Pleistocene. *Science* 310, 1313-1317.
- Sigman, D.M., Boyle, E.A., 2000. Glacial/interglacial variations in atmospheric carbon dioxide. *Nature* 407, 859.
- Smith, H., Wahlen, M., Mastroianni, D., Taylor, K., 1997. The CO₂ concentration of air trapped in GISP2 ice from the Last Glacial Maximum-Holocene transition. *Geophysical Research Letters* 24, 1-4.
- Sowers, T., Bender, M., Raynaud, D., Korotkevich, Y.S., 1992. $\delta^{15}\text{N}$ of N₂ in air trapped in polar ice: A tracer of gas transport in the firm and a possible constraint on ice age-gas age differences. *Journal of Geophysical Research: Atmospheres* 97, 15683-15697.
- Sowers, T., Brook, E., Etheridge, D., Blunier, T., Fuchs, A., Leuenberger, M., Chappellaz, J., Barnola, J.M., Wahlen, M., Deck, B., 1997. An interlaboratory comparison of techniques for extracting and analyzing trapped gases in ice cores. *Journal of Geophysical Research: Oceans* 102, 26527-26538.
- Sowers, T., Jubenville, J., 2000. A modified extraction technique for liberating occluded gases from ice cores. *Journal of geophysical research* 105, 29.
- Spahni, R., Schwander, J., Flückiger, J., Stauffer, B., Chappellaz, J., Raynaud, D., 2003. The attenuation of fast atmospheric CH₄ variations recorded in polar ice cores. *Geophysical Research Letters* 30.
- Stephens, B.B., Keeling, R.F., 2000. The influence of Antarctic sea ice on glacial–interglacial CO₂ variations. *Nature* 404, 171.
- Stocker, T.F., Johnsen, S.J., 2003. A minimum thermodynamic model for the bipolar seesaw. *Paleoceanography* 18.
- Tans, P., Keeling, R., 2017. Trends in atmospheric carbon dioxide. url : <https://www.esrl.noaa.gov/gmd/ccgg/trends/> (visited on Oct. 24, 2018).
- Toggweiler, J., Gnanadesikan, A., Carson, S., Murnane, R., Sarmiento, J., 2003a. Representation of the carbon cycle in box models and GCMs: 1. Solubility pump. *Global Biogeochemical Cycles* 17.
- Toggweiler, J., Murnane, R., Carson, S., Gnanadesikan, A., Sarmiento, J., 2003b. Representation of the carbon cycle in box models and GCMs, 2, Organic pump. *Global biogeochemical cycles* 17.
- Toggweiler, J.R., Russell, J.L., Carson, S.R., 2006. Midlatitude westerlies, atmospheric CO₂, and climate change during the ice ages. *Paleoceanography* 21.

- Tschumi, J., Stauffer, B., 2000. Reconstructing past atmospheric CO₂ concentration based on ice-core analyses: open questions due to in situ production of CO₂ in the ice. *Journal of Glaciology* 46, 45-53.
- Uchida, T., Yasuda, K., Oto, Y., Shen, R., Ohmura, R., 2014. Natural supersaturation conditions needed for nucleation of air-clathrate hydrates in deep ice sheets. *Journal of glaciology* 60, 1111-1116.
- Volk, T., Hoffert, M.I., 1985. Ocean carbon pumps: Analysis of relative strengths and efficiencies in ocean-driven atmospheric CO₂ changes. *The carbon cycle and atmospheric CO₂: natural variations Archean to present* 32, 99-110.
- Wahlen, M., Allen, D., Deck, B., Herchenroder, A., 1991. Initial measurements of CO₂ concentrations (1530 to 1940 AD) in air occluded in the GISP2 ice core from central Greenland. *Geophysical Research Letters* 18, 1457-1460.
- Wilson, A., Donahue, D.J., 1989. The recovery and dating of carbon dioxide in polar ice cores. *Radiocarbon* 31, 579-584.
- Zumbrunn, R., Neftel, A., Oeschger, H., 1982. CO₂ measurements on 1-cm³ ice samples with an IR laserspectrometer (IRLS) combined with a new dry extraction device. *Earth and Planetary Science Letters* 60, 318-324.

Acknowledgements

The first thanks goes to Jérôme Chappellaz, Roberto Grilli, Frédéric Parrenin for giving me this chance to gain additional insights related to the carbon cycle using Antarctic ice core. I thank your help in expanding my knowledge in laboratory technique, ice cores and statistics and scientific guidance. Thank Grégory Teste so much for the support, the discussions and the constant help in the laboratory. He was one of the most important people in the laboratory. Many thanks especially to D. Raynaud for the very profitable discussions and reviewing this thesis and sharing his invaluable knowledge in gases in ice cores. I would like to thank Clara Dupraz for the assistance in the CO₂ measurements during the first part of my PhD. Thanks to Jai Chowdhry Beeman for proofreading my thesis and sharing idea in statistics and climate. Thank to Julia Gottschalk for discussions about CO₂ variability and climate change during the last two glacial periods. Thanks to Thomas Stocker, Hubertus Fischer, Amaelle Landais, Jochen Schmitt, Bernhard Bereiter, Christoph Nehrbass-Ahles and Loïc Schmidely for sharing the knowledge and views on atmospheric CO₂ and general inspiration. Thanks to X. Fain and K. Fourteau for help on the CH₄ analytical system.

